Comprehensive Investigation of Mechanical Properties of Fused Deposition Modelling

A dissertation presented in partial fulfilment of the requirements for the degree of

Doctor of Philosophy in Engineering

At Massey University, Albany, New Zealand

Arno Ferreira

May 2017

PREFACE:

The author declares that this is his own work except where due acknowledgment has been given. It is being submitted for the PhD in Engineering, majoring in Mechatronics to the Massey University, New Zealand.

This thesis describes the research carried out by the author at the School of Engineering and Advance Technology, Massey University, Albany, New Zealand from June 2014 to May 2017, supervised by A/Prof J. Potgieter and Dr. K. Arif.

ACKNOWLEDGEMENTS

There are a number of people without whom this thesis might never have been written, and to whom I am greatly indebted.

My deepest gratitude goes to Associate Professor Johan Potgieter, who expertly guided me throughout my post graduate education. I am thankful for the enthusiasm that he showed throughout the entire project, for helping me not only develop my understanding of the project but also developing my skills as a researcher, for his assistance with research funding and providing all the resources required to achieve this goal and for going above and beyond.

My appreciation also extends to Dr. Khalid Arif for his expert guidance and assistance during the project. Dr. Khalid Arif's mentoring has been especially valuable along with his unwavering encouragement, enthusiasm, and wisdom.

I would like to thank my partner and family for supporting me during the stressful times and throughout this process. Emily, who has been unfailingly supportive as I pursued this goal, always willing to do whatever she could to make my life easier. To my parents I am also forever grateful. Thank you to my mother, Althea, who has been a source of encouragement to me throughout my life. Her unwavering belief in my abilities and constant support mean the world to me. My father, Solomon, who always knows what to say and for the myriad of ways, throughout my life, that he has actively supported me to find and realise my potential.

It would be a remiss not to mention and sincerely thank Dr. Steven Matthews for his advice and support and the administrative staff at Massey, specifically Dianne Cook, who always helped in whatever way she could.

Abstract

Fused depositing modelling (FDM) is a layer wise manufacturing method whereby parts are printed from the bottom up through the extrusion and deposition of a filament onto a print base. Various test methods exist for the determination of part mechanical properties. These include tensile, flexural, and impact testing and are conducted using a variety of standards including those of ASTM and ISO. Many researchers have investigated the effects of factors such as road width, raster orientation, layer height, and air gap on the mechanical properties of FDM parts. However, there are many unexplored factors that also impact on the properties of printed parts. For example, the printers used in characterisation studies are mostly commercially available or consumer market printers which allow only limited control over the print parameters and print with a limited set of materials. Similarly, the life of the printer can also affect the print quality but this has not been studied before.

Control over machines could be achieved by purchasing additional print profiles from the manufacturers or by open-sourcing legacy hardware through retrofitment with new electronics and software. The latter option is more economically viable as there are a large number of decommissioned legacy machines that have superior hardware cheaply/freely available. A retrofitted commercial 3D printer would allow control over print parameters and printing with materials outside the ones sold by the manufacturers. This can open new avenues to study the properties of the printed parts. In this work, a Stratasys Vantage X 3D printer has been retrofitted and made open-source through a combination of hardware, software, and firmware modifications. These modifications result in complete control by the user over all print variables along with the ability to use any feedstock including custom made feed stocks and ones that are locked by the manufacturer. The printing accuracy of the machine is evaluated by optical imaging of the printed samples and destructive testing in accordance with the ASTM D638 standard. .

To study the effect of the machine's life on the properties, a longitudinal study is designed in which two groups of parts (with 0° and 90° orientations) are printed at two different times during the course of this research. The temporal spacing between the parts is eighteen months. The parts are designed according to ASTM D638 standard and printed on identical printers using the same parameters on both occasions. The parts are subjected to tensile

testing for the mechanical characterization while scanning electron microscopy (SEM) is used for the examination of the sample's fracture and topographical surfaces.

A difference is discovered between the Young's moduli of old and new groups. The orthotropic nature of FDM parts becomes prevalent in the strain responses of samples with 0° samples experiencing the largest strain. Distinct differences exist between the diffusion levels of the chronological sample groups, with the original batch exhibiting greater diffusion resulting in almost indistinguishable layers and higher tensile strengths. Individual layers are easily observed in the newer sample groups. Topographical analysis of samples shows up to 0.1mm difference between the road widths with the older samples roads being the narrowest. Results from this research show that the age of the printer affects the mechanical properties of the parts with the older parts exhibiting greater strength compared to their new counterparts even though both were printer under identical conditions. Therefore, a significant difference exists between temporally spaced FDM parts.

To conclude, this research has successfully retrofitted an old FDM system which is capable of printing various materials through a choice of user parameters. The longitudinal study conducted to study the effect of the machine age on the printed parts purports that as the printing machines get older their print quality deteriorates and this factor should be considered by designers when designing parts for functional purposes.

List of Terms and Definitions

Print orientation: This refers to the inclination of the part with respect to the X, Y, and, Z axes with the X and Y -axis parallel to the build platform and the Z axis perpendicular to the platform in the direction of the build.

Raster angle: For the purposes of testing, it is the angle between the raster relative to the applied direction of the load. During the printing process, it is traditionally referenced to the angle of the raster relative to the X-axis on the build table.

Layer thickness: This is the thickness of the layer deposited by the nozzle.

Nozzle height: This is the height between the extrusion nozzle and the previously deposited layer or at the start of a print, the height between the nozzle and the print bed.

Road: This refers to a single strand of deposited material. The conglomeration of the roads makes up the raster pattern.

Raster width: This is the width of a single deposited road.

Raster gap (air gap): This refers to the gap between two adjacent roads on the same print layer.

Voids: These are spaces between two adjacent roads or layers where material would ideally exist but was not successfully filled.

Infill: This is a value usually represented as a percentage. It represents how much of a solid model should be filled in.

Number of shells (boundary layers): This is the number of outlines printed in each layer. The higher the number of shells, the greater the strength of the printed object.

Extruder temperature: This is the temperature at which the extruder operates during printing. This temperature setting is dependent on the material used.

Printing speed: This is the speed at which the printhead moves while it is extruding filament.

Extrusion rate: This is the speed at which filament is extruded.

Movement speed: This is the speed at which the printhead moves while it is not extruding the filament.

Fill pattern: This is the pattern used for the interior fill of a part. This is made up of linear roads at varying raster angles but can also be hexagonal, diamond and other patterns.

Printer age: The time between the printer being commissioned and the current date.

Table of Contents

Table of Figures

Table of Tables

1. Introduction

1.1. Research Objective

Additive manufacturing (AM) was first developed in the 1980's in the form of stereolithography (SL). The research and development of this process was aimed at simplifying the prototyping process by reducing time and cost associated with traditional methods. Fused deposition modelling (FDM) was later developed and commercialised Stratasys in the early 1990's and has since seen a major open-source and industrial development [1]. FDM has become the most popular and widely used AM technique with half of the machines on the market being of this kind. The size of this industry in 2013 was $3.07 which showed an increase of over $2 billion from 2011 where it was $1 billion [2-4]. As the development of FDM continued, the quality of parts produced improved with the technology evolving into a final manufacturing method. The layer wise printing process allows for the manufacture of functional and intricate parts at a relatively low cost. However, parts produced by this method suffer from anisotropic properties limiting their use for certain applications. It also requires a user who is well versed in the technology and the printing methods in order to optimise the print parameters based on the intended application.

Advancements in the technology has seen companies such as Air New Zealand incorporate it, by their research teams, for the development of cabin parts for their aircrafts. However, one of the problems faced by companies such as these is the inconsistent nature of FDM parts along with the limitations parts have in specific orientations due to delamination between consecutive layers. This is one of the reasons why FDM has not been implemented for the development and use of parts that must be reliable and exhibit constant predictable behaviour for design and safety purposes. The anisotropic nature of FDM pars have sparked the interest of several research groups. Research into the effect of print parameters on part tensile, compressive, impact and, flexural strengths started soon after the conception of the technology and continues today. Most of the research conducted intends on understanding the FDM process more thoroughly and allowing for the continuous improvement of the technology. These improvements focus on several areas including the surface finish and final aesthetic look of the parts, however majority of the research is aimed at part mechanical

properties. With the principal operation of FDM being identical for all systems manufacturing parts using this technology, slight variations exist between different machines that greatly affect the part's mechanical properties. These variations are normally due to the quality of the printer's hardware and software along with the manufacturer determined parameters.

1.2. Problem Statement

Research into the mechanical properties of FDM parts are conducted using a wide variety of printers to manufacture test specimens. One of the largest restrictions the research community experiences is the limitations on controllable print parameters. In order to overcome this limitation, research teams have turned to open source 3D printers such as MakerBot, granting them greater access to the print parameters. Unfortunately, these printers are normally manufactured using lower quality hardware and off-the-shelf components. Open source printers normally produce inferior parts compared to those manufactured on commercial printers and have higher levels of inaccuracies and distortions. Alternatively, commercial machines ensure high quality parts with exceptional strength and reliability. However, these printers have fewer user controlled print parameters restricting the ability of the researcher to fully examine all aspects that play a role in the properties of the manufactured part. Commercial printers are also restricted to the material stock they can use. Printers are sold capable of only using one or two material types and cost tens of thousands of dollars to unlock its capability to print using alternate print stock. Most open source printers are restricted and only capable of using either ABS or PLA feed stock for printing. No system exists that has the quality hardware of a commercial machine with the open source access to all control parameters allowing for more in depth research to be completed on the mechanical properties of FDM parts.

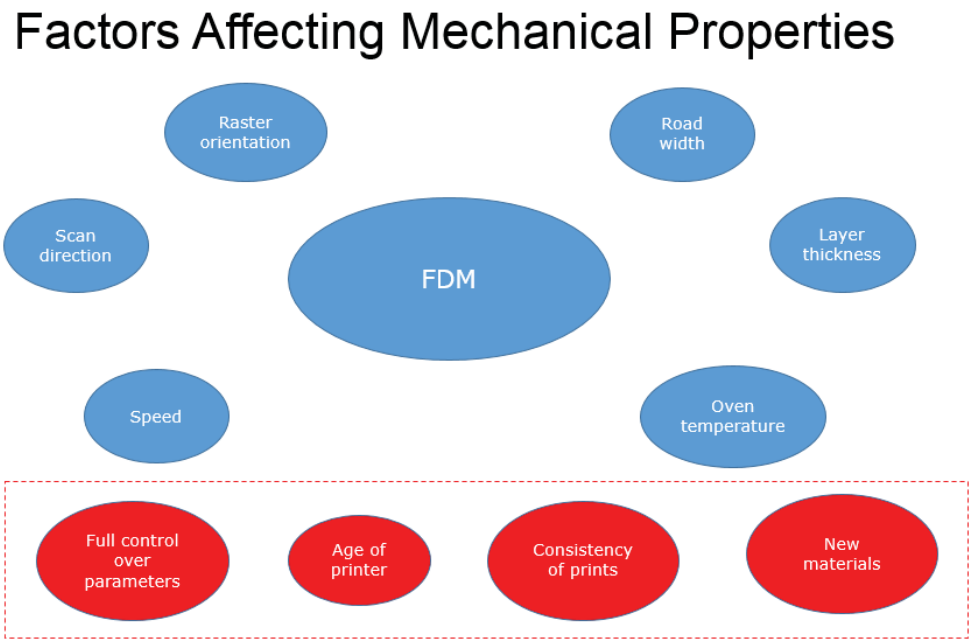

Figure 1.1 Blue: Factors that are known to affect the mechanical properties of FDM parts. Red: Factors whose effects on FDM mechanical properties have yet to be investigated.

Even though print parameters will affect parts from any FDM printer in the same manner, researchers have continued to use printers that vary in quality, age, and cost. The knowledge gained from research on these machines help to improve the quality of parts manufactured on any machine by use of the optimal print parameters. However, the mechanism of FDM mechanical properties is not fully understood. This brings into question the reliability of parts printed on different machines. Even though certain parameters such as raster angle are known to affect the mechanical properties in all FDM machines in a similar manner, research into machine-to-machine variation or machine age as a factor has never been conducted. In the field of FDM research, there is a lack of longitudinal studies investigating the printers and the properties of the parts manufactured on identical high quality commercial machines. No investigation has been conducted on the impact of age on parts either. There has always been an assumption that identical printers will produce identical parts with similar properties, however, studies on the effect of age on identical printers have not been completed. Therefore, there is no concrete evidence on how the part properties of samples produced chronologically on identical machines vary. This directly affects a designer's ability to design parts in accordance with the variations between identical printers used to manufacture the same parts at different times.

The manner through which FDM parts have been examined has traditionally been through mechanical testing supplemented with some scanning electron microscopy (SEM) imaging.

Thorough investigation of the topographical and fracture surfaces of FDM parts has not been conducted, even though this can be a vital tool in understanding and identifying the differences that exist between parts. It also enables researchers to examine the methods and patterns by which parts are manufactured and the variation in the deposition methods.

1.3. Research Solution

Through a comprehensive literature review, this research aims to identify and study the factors influencing the mechanical properties of FDM parts that have never been investigated. Through this literature review, a broader understanding of the standards used during part testing will be achieved. It will also help to determine the standards to be used for this research along with defining the tests and methods to employ. The lack of control variables open to researchers and how this could affect the achievable results are identified in the literature review as per figure 1.1. With current printers either being open source, hobbyist type printers that aren't consistent or reliable enough for research purposes or commercial machines with limited control, the decision was made to retrofit a commercial FDM machine allowing full control of all print parameters to the user. With the large amount of vintage commercial FDM printers available on the market due to the high frequency in which they are replaced with newer models, the retrofitment of a vintage FDM machine will allow researchers to manufacture test samples using a wider variety of control variables at low cost. This is a piece of research equipment the likes of which has not been available to researchers before. In this research, as part of the retrofitment of the Stratasys Vantage X printer, the need for Stratasys drum cartridges will be removed allowing the use of any extrusion based feed stock. This in conjunction with granting complete access to the control variables will result in an ideal research machine. This retrofitment will prove that commercial FDM printers can successfully be modified and optimised for research use.

With an increase in the number of bureaus manufacturing parts for customers in industry, it is hard to guarantee the quality of parts produced on identical machines under identical circumstances would perform in the same way. Taking into account that designers design parts around the known variables that affect the mechanical properties of part, it is important to identify variables that could affect the part properties, but have yet to be investigated. The lack of research into the effect of machine age, print consistency and chronological manufacture effects was identified during the literature review and therefore considered as

part of the comprehensive investigation of the factors affecting FDM part properties. The research undertaken aimed at answering the questions of how stress, strain, and elasticity of chronologically printed parts vary. It also aims to add understanding of how printer age would affect part properties and what designers need to consider when having parts manufactured by different bureaus. The mechanical testing method used for this research is identical to what has traditionally been used in other studies. This not only adds valuable understanding of the temporal effects on FDM parts but also contributes to existing knowledge of the mechanical properties of these parts. This will allow design engineers to more effectively design parts taking into account all the known variable that affect part mechanical properties including the effect of printer age. In order to further investigate how the age of a printer affects its mechanical properties, bulk material samples using the same ASA material was used to injection mould test specimens. These samples act as a benchmark with their mechanical properties compared to those of the 3D printed parts. Thorough SEM analysis investigating specific areas of bonding such as abnormalities in road widths, and varying levels of diffusion, the understating of the printing process and the influence of printer age on the mechanical properties of parts can be furthered.

1.4. Thesis Layout

This thesis is laid out in 6 chapters as following.

Chapter 2 consists of a thorough literature review on the standards and test methods used for FDM testing aiding in the discovery of the potential research areas. A brief discussion on retrofitment of machines is also appended in this chapter.

Chapter 3 describes the retrofitment of the Stratasys Vantage X FDM printer along with the initial testing and results of part properties based on the ASTM D638 standards. This chapter is based on a published paper and included in the thesis with kind permission of Springer.

Research conducted into the temporal effect on FDM parts manufactured under identical conditions along with the SEM analysis of their fracture surfaces and topographical nature is presented in chapters 4 and 5.

Chapter 6 presents the conclusion and recommended future work.

2. Literature Review

2.1. Introduction

Additive manufacturing (AM) or three-dimensional printing (3DP) is a rapidly expanding technology whereby complex parts can be fabricated in a relatively short timeframe compared to the weeks or months of traditional prototyping. Generally, the parts are built by adding layer upon layer of material through different processes such as sintering, melting, extrusion, or photo polymerization, etc. The parts manufactured with AM require little to no post-processing and result in almost no wasted material [5]. Different AM processes have their own strengths and weaknesses; these are dictated by the choice of material and the additive processing method. Sintering and melting result in strong mechanical properties but require high power laser systems to operate [6]. On the other hand, resin-based methods produce superb surface finish but lack useful mechanical functionality. Extrusion-based methods rely on forcing the material through a heated nozzle to build parts. This process is termed as FDM and is the most versatile and commonly used in low end to high end printers. This process can work with almost any material as long as it can be liquefied and extruded through a nozzle. If the extrusion material is manufactured into filaments, the whole process can be clean, dust-free and safe [7].

In FDM parts are manufactured in a layer-wise manner by extrusion of semi-molten tracks placed on a build platform. The parts are built from the bottom to the top (Fig. 2.1a). The filament, traditionally Acrylonitrile Butadiene Styrene (ABS) or other thermoplastic is extruded through a heated die and deposited onto the previous layer based on the path determined by the slicing software [8]. However, ABS is only one of many materials used: ULTEM 9085 is becoming popular in the aerospace industry for the production or parts such as air gates, panel covers and other interior parts [9, 10]. Many biodegradable materials like polylactic acid (PLA) [2, 11], polymethylmethacrylate (PMMA) [12] or biopolymer composites with natural fibre are also being widely investigated [13, 14]. FDM technology has drastically improved over the past decade and approximately half of the machines introduced into the market are part of this category. It is estimated that by 2018, the low-end 3D printing space will be worth approximately $5.1 billion in revenue globally. It took the

additive manufacturing industry 20 years to reach a total worth of $1 billion by 2011 but grew to $3.07 billion USD in the following two years [2-4, 15]. Just the material sales are projected to increase to $8 billion by 2025 [16].

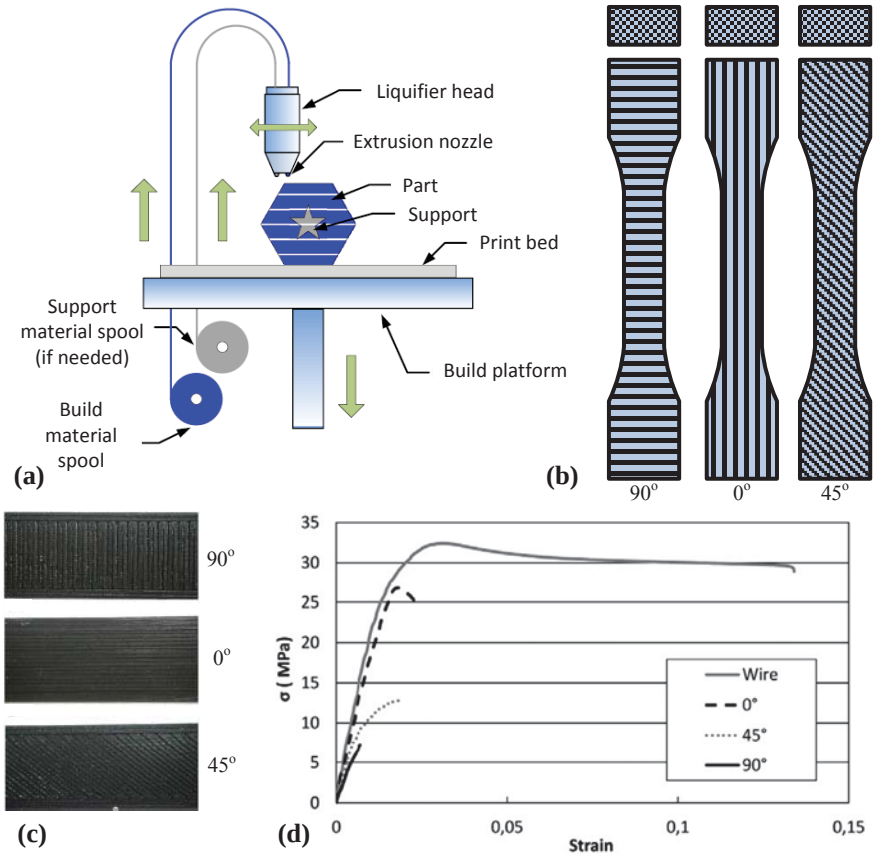

Figure 2.1 (a) Schematic of FDM process; (b) three types of raster orientations, 90° orientation specimen; 0° orientation specimen, 45° orientation specimen; (c) Images of printed single layer specimens; (d) representative tensile testing data for ABS at each raster orientation, modified from [17].

In recent years FDM technology has grown tremendously, during which the desire to use printed parts as final products rather than prototypes has also significantly increased [18]. For any functional use of printed parts, the importance of mechanical properties cannot be over-stressed. Inherently, the FDM process is anisotropic (Fig. 2.1 b, c); the parts exhibit strength behaviour that varies as a function of raster orientation [17, 19] (see Fig. 2.1d). The roads and layers are building blocks of the fabricated parts. The material is stronger in the direction of the roads compared to the transverse direction where the strength comes from inter-road adhesion. According to [17] the strength and ductility properties of FDM parts vary greatly depending on their filament orientation and that parts with their orientation perpendicular to the loading direction can be 50% weaker than their parallel printed counterparts. This limits its application for structural and end use parts. Other qualities, such as surface roughness [20], are also significantly affected by factors such as the layer thickness and part orientation.

Overall, the main variables that affect mechanical properties of FDM parts are the print orientation, raster orientation, air gap, raster width, and layer thickness [21-27].

Due to the aforementioned anisotropic nature of FDM technology the evaluation, prediction and optimisation of parts printed through the FDM process is highly desirable. A variety of different techniques have been developed to determine the significance of process variables. As there is no common standard yet available for the testing of printed parts, many researchers make modifications to existing standards and present results in a similar way to as bulk processed materials. Mechanical testing (tensile, compressive, impact, flexural and three-point bending tests) have been used as part of this evaluation process with tensile testing being the most common [22, 28-32]. Optical and electron microscope analysis have also been used for characterization of the manufactured parts [32-34]. Furthermore, finite element analysis (FEA) [35-37] has been widely used to study the properties of FDM in the recent years.

In this research, the currently used testing methods for prediction of mechanical properties of FDM printed parts are reviewed. The purpose is to familiarize the reader with the available testing standards and techniques and highlight the pros and cons of each method. The focus of this literature review is mainly on mechanical testing, but it also introduces other novel methods of characterization.

2.2. Mechanical Testing

2.2.1. Tensile Testing

Mechanical testing of 3D printed materials is the most widely used method of characterization. Parts are subjected to various loading conditions such as tensile, compression and three-point bending. Of these, tensile testing is the most popular. To accurately test the tensile strength of materials a standard is required for the size and shape of the specimens. However, with 3D printing being a relatively new technology no such standard yet exists. This has resulted in a variety of standards being used by researchers. Weng et al. [38] recently studied tensile strength and flexural strength of nanocomposites according to ASTM D790-03 and ASTM D638-03, respectively. Thermal expansion and dynamic mechanical tests was also used to evaluate their samples. Szykiedans et al. [39] and Gorski et al. [40] used the EN ISO 527-3 type 5 specification and slightly modified the

samples for printing instead of cutting or moulding whilst Dawoud et al. [41] used the DIN EN ISO 527-2 standard. Bertoldi et al. [42] and Bellini et al. [19] based their research samples on the ASTM D 5937 – 96 standard for moulded plastics. GB/T 16421 – 1996 was used by Wu et al. [43] whereas Sood et al. [22] and Rayegani et al. [44] used the ISO R527:1966 standard for the determination for tensile properties of plastics. The most commonly used standard however is the ASTM D638 – 10, used by Croccolo et al. [25] and Ning et al. [45] amongst others, which is the standard test method for determining the tensile properties of plastics. Since these standards are developed for bulk processed materials, Ahn et al. [30] deviated from the ASTM D638 standard and used a rectangular shape instead which was adapted from the ASTM D3039, which is used as standard test method for tensile properties of polymer matrix composite materials. Ziemian et al. [46] also used the ASTM D3039 standard for their experimental work. The authors of these papers did this to avoid stress concentration in the necking region of the samples from the FDM printing process. This stress concentration could result in premature failure of the test specimens and the adoption of the ASTM D3039 prevented such failures and provided true reflection of mechanical strength of the printed specimens.

All of the before mentioned standards use dog-bone shaped test specimens of various sizes. Depending on the control variables under examination, parts are manufactured in accordance with the respective standard. The approaches to printing these test samples are largely dependent on the chosen control variable setup. Raster orientation and air gap has been found to have the most significant influence on the tensile properties of 3D printed parts [21, 30, 47]. The number of layers used to successfully print the dog-bone shape depends on the chosen layer thickness and sample height where: Number of layers = Sample height / Layer thickness. It is important to note that the stress-strain relationship of FDM specimens differs from that of the bulk material they are printed from due to differences in material density and bonding (Fig. 2.2 a, b).

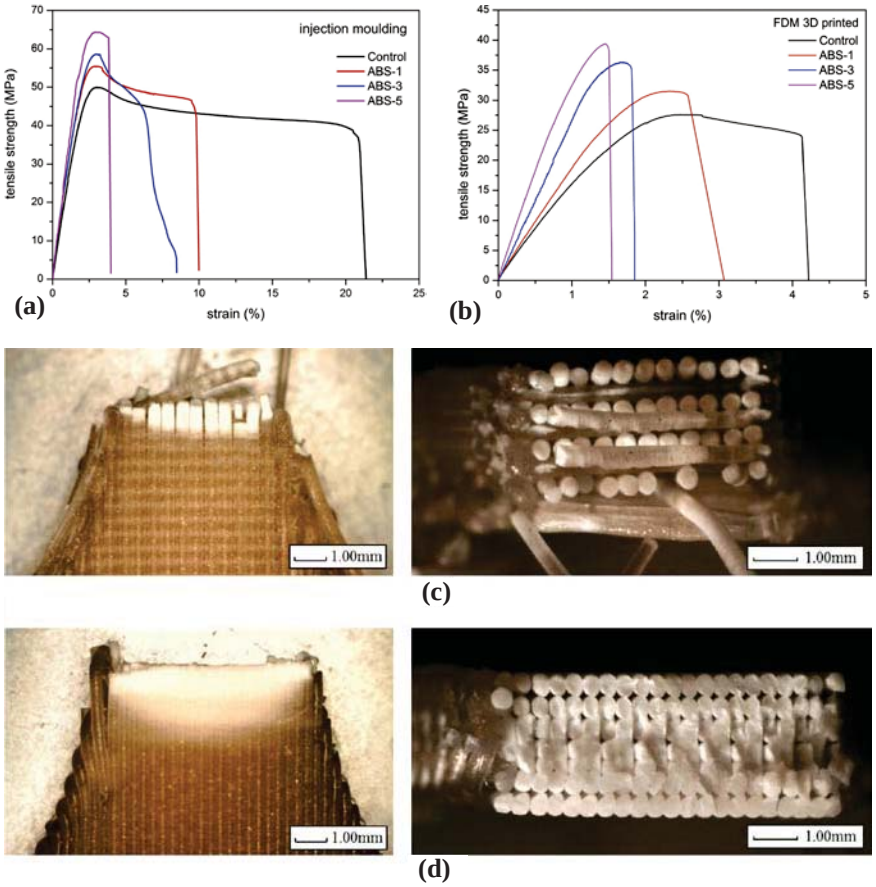

Figure 2.2 Tensile strength of ABS/OMMT nanocomposites samples, (a) made by injection moulding and (b) made by FDM 3D printer [38]. Tensile failure mechanisms for (c) orientation which displays non-uniform deformation at the rupture site as opposed to (d) orientation which shows a nearly uniform fracture surface [48].

Test parts are traditionally printed with a 0°, 0°/90°, ±45° and 90° raster orientation (Fig. 2.1 b, c) although this does vary where some researchers have used ±30° orientations etc. [15, 17, 21, 49]. The test methodologies vary widely, however, it is common for parts to be compared by manipulating a single variable at a time. Samples are printed in groups with sample sizes of three, five, or sometimes more to get better average results. When investigating the effect of raster orientation, typically five parts will be produced at each step of offset angle, after which each group will be tested using traditional tensile testing methods. This process results in a group mean and standard deviation which can be compared. Other approaches include, but are not limited to, Analysis of Variances (ANOVA) and Design of Experiment (DOE) [22, 30, 48, 50]. These approaches allow the manipulation of multiple variables at the same time while reducing the number of runs required to determine the significance of their influence of the tensile strength of parts.

During the tensile testing process, samples are loaded into a tensile testing machine, most commonly an Instron Testing System [51], Zwick Z010 testing machine [52], or Shimadzu

AGX-100PLUS [38], and kept in place using two wedge-action grippers. The samples are positioned in the wedges at a set crosshead displacement based on the standard being used. For ASTM 638 – 10 type 1 the set distance is 115 mm. An extensometer is normally attached in the longitudinal axis to capture the local strain in the necked region. The strain rate is an important factor for ensuring the accuracy of the stress-strain curve. A slower rate ensures that the molecules have time to mobilize and relieve stress locally by uncoiling. Should the rate of extension (crosshead speed) of the part be too high, the resultant stress value at failure could be lower due to the primary bonds failing prematurely [53, 54]. The crosshead speed used is normally specified by the standard being used. Whilst some published experiments have used ranges between 1mm/min and 2mm/min [22], the most commonly used ASTM D638 – 10 standard recommends 5 mm/min [17].

2.2.2. Compression Tests

Compression testing of printed parts captures how they will react under compressive loads. Similar to tensile testing, there is currently no standard methodology for applying compressive loads to FDM parts (e.g. normal, perpendicular, oblique to print plane). Thus, this has led to a variety of standards being used. Ahn et al. [30], one of the earlier research teams investigating the compressive properties of FDM parts, used the ASTM D695 (standard test method for compressive properties of rigid plastics) standard [55]. This same standard was also used by Ziemian et al. [46]. The ISO 604-1973 (plastics-determination of compressive properties) was referenced for their sample standards by Panda et al. [56], Percoco et al. [57] and Sood et al. [58]. The latter, however also used the ISO R291:1977 standard (plastics – standard atmospheres for conditioning and testing) during their research to ensure the test conditions were appropriate [30, 43, 56-58]. An alternative standard, GB/T1041-2008, was used by Wu et al. [43] for such compression testing.

The standards use either cylindrical or rectangular shaped test specimens of various sizing according to which parts are manufactured. As in the case of tensile testing, parts are all printed using the FDM print method but the control variables are changed in accordance with the chosen experimental setup by the respective researchers. Ahn et al. [30] investigated the effect that print orientation had on the compressive properties of parts. The print orientation is altered between three levels. Parts were either printed axially (horizontally) or transversely (vertically). Their raster angle and air gap settings were both kept at the standard printing levels of ±45° and zero respectively. Results indicated that for the control variable, print

orientation, samples printed axially (horizontally) exhibited 15% more compressive strength when compared to their transversely (vertically) printed counterparts. Lee et al. [29] conducted a similar experiment and also concluded that the axially printed parts exhibited the highest compressive strength (Fig. 2.3 b, c). Panda et al. [56] did a study in which three control variables, layer thickness, raster angle and print orientation, all had three levels 0.127mm, 0.178mm, 0.254mm; 0°, 30°, 60° and 0°, 15°, 30° respectively. Percoco et al. [57] evaluated raster width (the width of the extruded material deposited), raster angle and immersion time (time parts are immersed in 90% dimethyl ketone and 10% loads, the raster orientation had a very small influence on the compressive loads that parts were able to withstand.

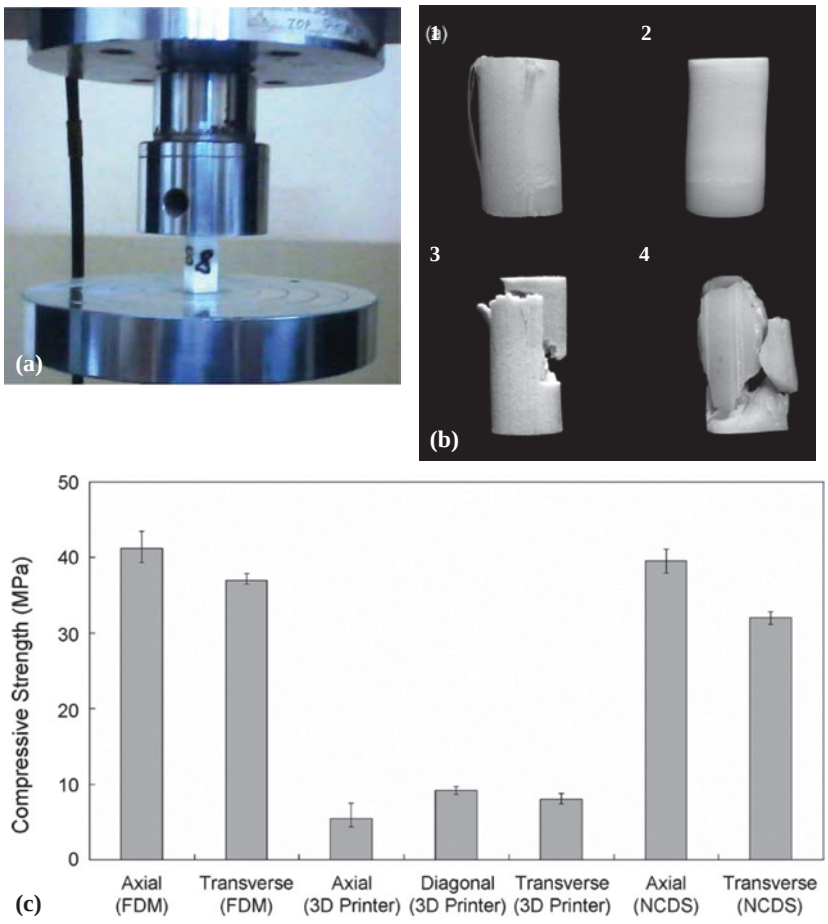

Figure 2.3 (a) A specimen during the compression test [56]. (b) Four failure modes of the specimens: (1) FDM-axial (2) FDM-transverse (3) 3D printer-axial and (4) NCDS-axial. (c) Compressive strength of each specimen [29]. NCDS stands for nanocomposite deposition system.

The approaches to testing vary; some researchers only vary a single variable whilst others evaluate multiple variables against compressive strength properties simultaneously. In order to help reduce experimental error, it is common practice to have sample groups each

consisting of five identical samples [43]. Percoco et al. [57] used a central composite design (CCD) approach in order to assess their test samples. Compared to their tensile testing approach, Ahn et al. [30] did not use ANOVA analysis to evaluate their control variable influence as they only had a single control variable. In order to reduce the required number of runs, Sood et al. [58] used a face centred central composite design (FCCCD). This was chosen over the spherical CCD approach which requires a higher number of runs.

Similar to tensile testing, compression specimens are loaded into a universal mechanical testing machine (Fig. 2.3a) and crushed with a cross head speed ranging from 1mm/min to 5mm/min [43, 57, 59]. As the test is completed, the software attached to the testing machine graphs a Stress (MPa) vs Strain (mm/mm) diagram of the part. Initially, the stress strain curve will behave linearly as the specimen undergoes an increase in the compressive load. However, as cracks generate, this curve starts to become non-linear and inelastic in its response. Once the peak stress is reached the stress value suddenly drops as the strain continues to increase. Non-linear region can experience stair stepping which is due to the force per unit area reaching a value at which the material continues to deform [58]. In the absence of cracks, one would expect the graph of stress vs strain to rise steeply, which is common for materials expanding under compressive loads.

There is currently no single standard for compressive testing; researchers from different groups adapt different standards, resulting in incomparable findings. One of the biggest concerns is that the standards are developed for bulk processed materials, which exhibit different failure modes when compared to printed specimens. The FDM process is known to produce specimens with non-homogeneous, anisotropic, characteristics which make them sensitive to the loading conditions. Therefore, their properties cannot necessarily be assessed accurately by current methods.

2.2.3. Impact Testing

Impact testing of FDM specimens suffers from similar challenges to tensile and compressive material testing; the properties are both non-homogeneous, and anisotropic. It is not as commonly used as tensile testing for the characterization of FDM parts.

Impact testing relies on a notched specimen that is held vertically as a cantilevered beam with the notch facing the direction of the pendulum hammer. During the test, the specimen is subjected to a quick, intense impact blow delivered by a pendulum hammer. The test

measures the impact energy with the results displayed in J/cm which is the absorbed energy per unit of thickness. This absorbed energy is calculated based on the potential energy difference of the hammer before (the initial height from which the hammer was released) and after impact (the height achieved by the hammer after the specimen has been impacted. The hammer height and its relation to the energy can be expresses as below [15, 22, 46].

$$E \propto (ho - hf) \tag{2.1}$$

where E= impact energy in J (N.m); h_0 = initial height, m; h_f = final height, m

The impact energy can then be used in order to determine the impact strength using equation

$$Impact\ strength = \frac{A_k}{L_1 \times L_2} \tag{2.2}$$

where A_k = impact energy in Joules and L_1 and L_2 is the sample thickness and the height of the sample minus the depth of the notch respectively. The values measured for each sample is normally graphed with sample groups used to find a more accurate mean value with standard deviation for each group.

There has predominantly two standards been used in the determination of the impact strength of FDM parts. The most commonly used ones are variations of ASTM D256. Roberson et al. [28] and Ziemian et al. [46] used the ASTM D256-10 standard, while other researchers such as Es-Said et al. [15] followed ASTM D256 – 88. The competing standard, ISO 179, and its variations is used by groups such as [41] and [22] who follow DIN EN ISO 179 and ISO 179:1982 (plastics – determination of Charpy impact strength of rigid plastics) respectively. Tsouknidas et al. [60] studied force dissipating capacity of printed specimens by calculating impact in relation to the impact velocity, based on static compressive tests, according to ISO 17340. Both bulk material and FDM printed specimens were used and they concluded that the impact absorption capacity of bulk material was higher than printed specimens (Fig. 2.4a).

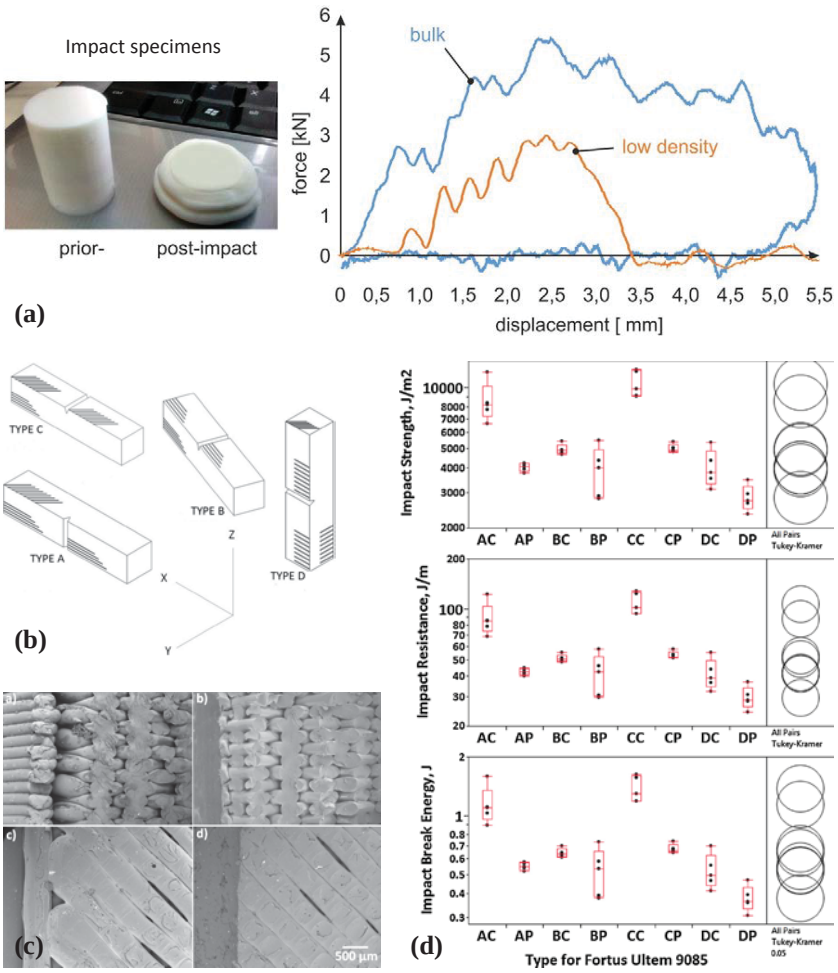

Figure 2.4 (a) Characteristic force displacement curves for bulk and porous specimens [60]. (b) The different build orientations and notch placements used in this study for samples printed on Fortus 400mc. The staggered lines represent raster orientation. (c) SEM micrographs of impact test fracture surfaces printed from Ultem 9085. (d) Graphical representation with Tukey–Kramer honestly significant difference analysis of impact test results for the different types and notched specimens printed on Fortus 400mc from Ultem 9085 [28].

Both above-mentioned standards use a V-notched rectangular block. The ASTM specimen is 63.5 mm long, 25.4 mm wide, and 25.4 mm thick, whilst the ISO specimens are 80 mm long, 10 mm wide, and 4 mm thick. Parts are printed using the standard FDM printing process. Most characterisation experiments of FDM part impact strength had the notch modelled into the CAD file. This meant that the test sample was printed with the notch. The material was not machined away after printing of the part; for example, [41, 46]. However, in the methodology of Roberson et al. [28], test samples were printed with the notch as well as having it machined out to the desired specification. Their research not only investigated the effect that build orientation had on the impact test results, but also investigated how the notching methods affected the test results. Sood et al. [22] investigated the effect of layer thickness, print orientation, raster angle, raster width and air gap and concluded that good strength depend on reduction of distortion in the build parts. Furthermore, the factors they

studied could not be selected independent of each other as their interaction played significant role in dictating the strength. Es-Said et al. [15] investigated the effect of altering the raster angle only but found superior impact strength and resistance for layers deposited along the length of the samples.

As there is no set standard for FDM testing, the experimental approaches vary. Dawoud et al. [41] investigated two control variables, raster angle and air gap, in their experiments. Through the use of ANOVA testing, they found that the raster angle had a significant effect on the impact strength for both positive and negative air gaps. Es-said et al. [15] and Ziemian et al. [46] also used ANOVA analysis in order to determine the statistical significance of their chosen control variables (air gap, road width, fill style, etc.). Roberson et al. [28] used various statistical methods in order to analyse the data gathered from their tests. The Tukey-Kramer honestly significant difference (HSD) test was used in order to graphically display and determine the statistical significance between sample sets. The greater the overlap of one sample sets circles with another, the less statistically significant the difference between the sample pools (see Fig. 2.4 b, d).

As the standards are used to determine the impact strength of homogeneous materials, parts manufactured through the FDM processes will vary in their response based on how the notch in the test samples are manufactured. Roberson et al. [28] concluded that parts notched mechanically after printing of a rectangular specimen exhibited a higher impact resistance when compared to their counterparts where the notch is printed in during the FDM process. Only the sample group with the raster layers oriented horizontally failed completely as this most likely allowed the crack propagation to occur along the bonding plane between the two layers.

2.2.4. Flexural Testing

Flexural testing is another mechanical characterisation method that evaluates the modulus of elasticity in bending E_f, the flectural strain as well as flexural stress and the flexural stress-strain response of the material being tested. This test helps to understand how FDM parts will respond under bending load, amongst other forces they might be subjected to depending on their application. It should be noted that according to Sood et al. [22] the optimal control of print input settings for both tensile and flexural strength are identical, but different for impact strength.

Many different methods have been applied for flexural characterisation of FDM specimens. Es-Said et al. [15] followed the ASTM D790 – 03 standard during their three point bending tests, whilst Ning et al. [45] used the ASTM D790 – 10 variation. Alternatively, Sun et al. [31] followed the ASTM D 1184 – 98 (standard test method for flexural strength of adhesive bonded laminated assemblies). Dawoud et al. [41], Sood et al. [22], Górski et al. [49], Panda et al. [61] and Rayegani et al. [44] used variations of the ISO 178 standard (DIN EN ISO 178, ISO R178:1975 and PN-EN ISO 178 (plastics – determination of flexural properties of rigid plastics)) respectively. Fatimatuzahraa et al. [21] also used a variation of the ISO 178 standard while Wu et al. [43] relied on the GB/T 9341-2008 standard for their research.

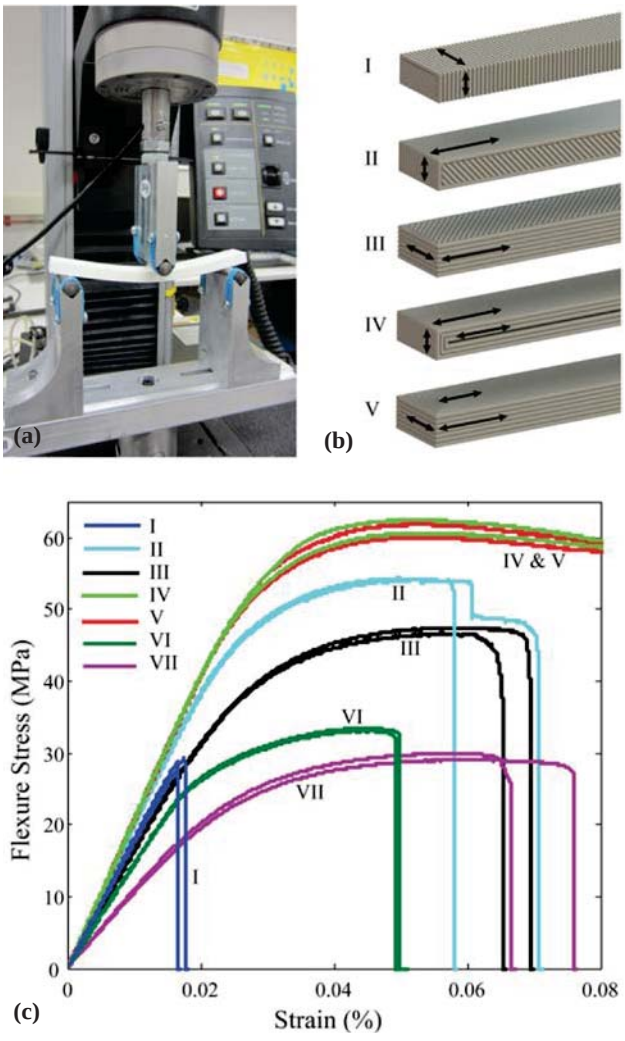

Figure 2.5 (a) A typical 3–point bending test setup. (b) Print orientations marked with black arrows in I-VI and (c) corresponding stress-strain curves [62].

There isn't a large variation between the bending samples used by the GB/T 9341-2008 and ISO 178 standards with samples being 80 mm long, 8 mm wide, 3.6 mm thick and 80 mm x 10 mm x 4 mm respectively. Samples created using the ASTM D 1184 – 98 standard by Sun et al. [31] were 31 mm long, 19.1 mm wide and 3.1 mm thick. Singamneni et al. [63] made use of 3 point bending tests in order to test their curved layered test specimens. The test samples were manufactured using a variety of FDM machines all utilising traditional Fused Deposition Modelling techniques. The control variable (print parameter) levels were determined by individual researchers based on their experimental research goals. Sun et al. [31] investigated the effect that changing the liquefier and envelope temperatures have on the flexural strength of FDM parts amongst other variables (e.g. chamber temperature and cooling conditions). Galantucci et al. [64] investigated the effect that chemically treating specimens with 90% dimethylketone and 10% water had on their flexural strength. For these tests, identical test samples were printed and half were subjected to chemical treating whilst the rest were left untreated. As per their findings, not only the surface roughness of the specimens improved but also the flexural strength showed general improvement. Wu et al. [43] investigated the influence that varying the layer thickness has on the flexural properties whereas Dawoud et al. [41] investigated the effect of layer thickness as well as raster angle and compared their flexural strength with that of injection moulded ABS. It was found that raster orientation and particularly air gap had a significant influence on the flexural strength of FDM parts. Fig. 2.5 b, c shows flexural stress-strain curves for six different orientations fabricated with ABS-P430 on a Fortus-250mc printer and tested following ASTM D790 [62]. A large variation in flexure strength based on print orientation is clearly visible. A strengthening technique based on void filling with resin resulted in improvement of the overall part strength and stiffness by up to 45% and 25%, respectively.

As the data analysis and testing approaches vary between research groups, various techniques are used during the experimental setup process. Dawoud et al. [41] used ANOVA analysis at a 95% confidence interval to assess the influence of raster angle and layer thickness on the flexural strength. Two 3-level CCDs were used by Galantucci et al. [64] during their investigation on how raster angle, raster width and chemically treated (with 90% dimethylketone and 10% water) or not specimens influenced the flexural strength of parts. Singamneni et al. [63] varied only a single process variable (build orientation) during their study of flat layered vs. curve layered FMD samples in order to prove that parts printed with

a curved layer was almost 40% stronger in bending when compared to their flat layered counterparts.

The 3-point bending test of samples require a machine that applies an increasing force in the middle of the upper sample surface with the beam lying on a support span, either side of the sample supported from below (see Fig. 2.5a for a typical setup). Various machines have been used to perform 3-point bending tests, with the most common being variations of the universal material testing INSTRON series. Universal testing machines such as the Lloyd LRX Plus Universal Testing Machine, the Mitutoyo TQ SRT Deflections of Beams & Cantilevers machine, INSTRON 4458 or 1195 series, and Zwick Roell Z020 machine are used in order to apply the increasing force [21, 41, 49, 61, 64]. The specification of cross-head speed does not vary much between standards; they have an average speed of 2mm/min [43, 61, 64]. The test parameters include support span, the loading speed/cross head speed and the maximum deflection of the part. These parameters rely on the thickness of the specimen. For the ASTM and ISO standards, there is a difference in when the test is stopped. The ASTM D790 standard require that the test is completed when the sample either reaches 5% deflection or fails before the 5% is reached [65]. ISO 178 states that the test will be completed once the specimen breaks. Should the specimen not fail, the test will continue as far as possible and the stress is reported at 3.5% [66].

As with the previously discussed mechanical testing methods, there is currently no standard flexural test designed specifically for FDM specimens. This has led to a range of standards and test methods being used in order to determine these mechanical properties. Non-traditional 3-point bending tests have also been performed for flexural studies on FDM parts e.g. Lee et al. [59] and Espin et al. [67]. Regardless of the large variety of standards and test methods used, the influence that print parameters such as raster orientation and air gap have on the flexural strength of parts is evident and consistent across the board.

2.2.5. Fatigue Testing

Fatigue testing is one of the least investigated mechanical testing methods currently used for the determination of FDM part properties. With the move of three-dimensional printing from a prototyping method to a manufacturing method, along with the influx of plastic parts being used in the biomedical and automotive industries, fatigue testing is vital to allow designers and engineers to forecast the expected life-span of a specific part. Thermoplastics such as

ABS are known to be sensitive to parameters such as: stress/strain amplitude of loading cycles; temperature; environment; and frequency.

Limited studies have been completed and published on the fatigue life cycles of FDM parts. Afrose et al. [68] investigated the effect that build orientation has on the fatigue behaviour of FDM specimens produced using polylactic acid (PLA) material. The specimens were manufactured in accordance with the ASTM D638 standard. Alternate standards that could potentially be used in the future include standards such as the ISO 13003:2003 standard (fibre-reinforced plastics – determination of fatigue properties under cyclic loading conditions) [69]. Fatigue testing can be conducted at a variety of frequencies; experimentation by Afrose et al. [68] utilised a frequency of 1 Hz via a Zwick Z010 tensile testing machine. The test parameters were kept constant for each test specimen at various applied loading conditions over cycles. To ensure that a data overflow problem did not occur during testing, three specimens for each of the print orientation were subjected to 5000 cycles with the applied load varying between 50, 60, 70, and 80 % of the UTS from specimen to specimen during testing. Printing parts in the X-, Y- and 45° orientations mimicked printing parts with the raster orientations equal to 0°, 90° and 45° respectively. This was based on the findings of Zoroufi M [70] who identified that during higher frequencies of testing, the specimen's temperature increases, which decreases its fatigue life. It enabled material flow in the sample and increased the ductility. The weakest section of the part's gauge length also experienced localised deformation. A lower frequency however, increased fatigue life with samples experiencing a more brittle fracture with limited gauge length deformation. During testing, wedge-like grippers identical to that of tensile testing are used.

To determine the effect of orientation on the fatigue properties of ABS and ABSplus Lee and Huang [71] followed the UNI EN ISO 527-1 (1997) standard. Dog-bone shaped specimen were printed in nine different orientations (3 horizontal on thickness side, 3 horizontal on width side and 3 vertical) from both materials and subjected to tensile and cyclic tensile loadings. It was observed that the fatigue strength highly depended on the print direction which influences strain energy of the specimen. Based on this observation the ABSplus material showed higher tensile strength but lower fatigue strength for some build orientations.

Fatigue testing of FDM parts is a valuable tool in the determination of their mechanical properties. With the goal of FDM being more towards creating end products now rather than prototypes, having a method of predicting the life cycle of a part is extremely useful.

2.2.6. Alternate Mechanical Testing

A number of alternate testing approaches have also been adopted by researchers to characterize mechanical properties of FDM parts. Lee et al. [59] investigated how process parameters (air gap, raster angle, raster width and layer thickness) affect the elasticity and flexibility of custom designed FDM parts. The parts were designed with the intention of flinging a ball as far as possible at different deflection angles to determine the elasticity of the parts. They used the Taguchi approach to help optimize the design approach. Nine prototypes were manufactured and displacement angles 10°, 15° and 20° were tested. The results were evaluated along with the control variables were analysed through ANOVA analysis to determine which control variable influence the flexibility of the prototypes the most.

Espin et al. [67] designed a simple L-shaped horizontally aligned hook in order to present a complex stress state (Fig. 2.6). The aim of the design was to produce stress in various directions that was below the yield stress exhibiting acceptable deformation. Parts were manufactured using three different build orientations and a total of 18 samples were printed. Three parts were printed for each possible orientation. However, since the elastic moduli in the x and y axes are different, the decision was made to build two different orientations for each of the build orientations. The first having the cantilever aligned with the x-axis and the second with the cantilever aligned with the y-axis. All parts were tested with the base plate of the cantilever clamped in place with the cantilever horizontally aligned. The test conditions had each part subjected to a 35mm displacement applied at 1mm/min 15mm from the end of the cantilever. Further details of this study are also given in the section on finite element analysis.

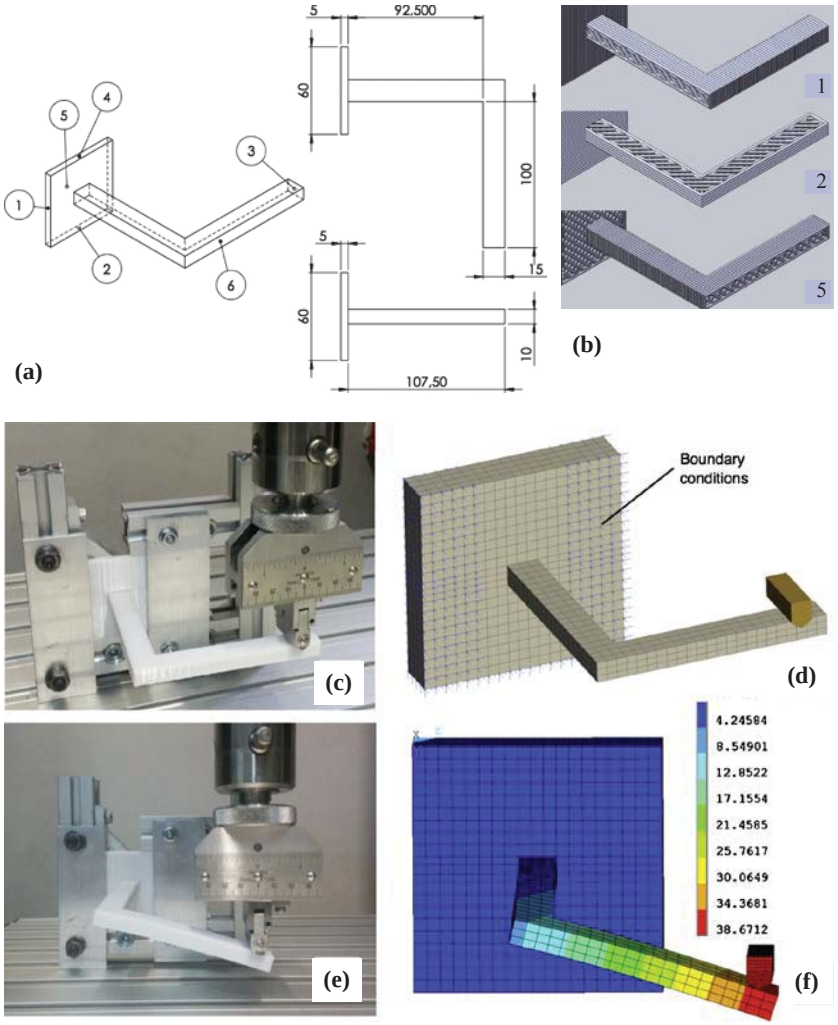

Figure 2.6 (a) Dimensions of the sample for physical and FEA simulation test with possible building bases numbered. (b) Diagram of the different slices disposition in the cantilever for each building orientation 1, 2 and 5. Setup for the experimental test, (c) and model for the simulation (d), small displacement (c & d), and photos taken at 35 mm of deformation (e & f) [67].

Table 2.1 Summary of mechanical testing techniques

Mechanical Testing Techniques	Machine Used	Standard Used	Test Method	Sample Shape	Result type	References
Tensile Testing	Instron 4468 Zwick Z010	ASTM D638 – 10 DIN EN ISO 527 – 2 EN ISO 527 – 3 ASTM D5937 – 96 GB/T 16421 – 1996 ASTM D3039	Samples are pulled apart at cross-head speeds between 1mm/min - 5mm/min	Dog bone shape with dimensions based on standard used	Ultimate strength Yield strength Young's Modulus Sample Fracture Point	[19, 23, 31, 41, 42, 47, 53, 56, 67, 72, 73]
Compression Testing	Instron 4485 Instron 1195 series IX Instron 5582	GB/T1041-2008 ASTM D695 ISO 604-1973 ISO R291:1977 ISO 604 -1973	Samples are positioned between two spherical seated platens with a cross-head speed between 1mm/min - 5mm/min	Cylindrical or rectangular shape based on standard used or modified by research group	Compressive strength (MPa)	[28, 51, 52, 54-56, 73]
Impact Testing	Charpy and Izod based Test equipment	ASTM D256 - 10 ASTM D256 - 88 ISO 179	Notched specimen held vertically as a cantilevered beam with the notch facing the direction of the pendulum hammer.	Rectangular shape with notch either printed or machined in	Impact Strength (J/cm)	[15, 19, 26, 47, 56]
Flexural testing	Instron 4458 Instron 1195 Zwick Roell Z020 Lloyd LRX Plus Testing – Machine Mitutoyo TQ SRT	ASTM D790 – 03 ASTM D790 – 10 ASTM D1184 – 98 PN-EN ISO 178 DIN EN ISO 178 GB/T 9341 – 2008	An increasing force is applied in the middle of the upper sample surface with the beam lying on a support span. An average cross head speed of 2mm/min is used.	Rectangular shape with approximate dimensions of	Yield Strength (MPa) Ultimate Strength (MPa) Effective Modulus (MPa)	[15, 17, 19, 29, 40, 42, 47, 57, 59, 67, 73]
Fatigue Testing	Zwick Z010	ASTM D638 ISO 13003:2003 standard	A mean load and alternating load is applied to a specimen with the number of cycles required for failure to occur being recorded. Loads can be applied axially, in flexure or, in torsion.		Fatigue Life Cycles	[64-66, 68]

2.3. Scanning Electron Microscopy

Scanning Electron Microscopy (SEM) analysis is considered non-destructive as it can be repeatedly done to a sample with the sample experiencing no volume loss [72, 74]. The use of SEM in the evaluation of the mechanical properties of FDM parts has become prevalent in recent years. The signals derived from the electron interactions with the samples reveal information about the sample, such as its external morphology, crystalline structure, and chemical composition. In the case of FDM the material orientation and fracture surface are readily visible (Fig. 2.7a). There are many SEM machines used for this purpose. For example, the Philips XL 40 ESEM used by Michigan Tech [75] , the JSM 500-type JEOL Scanning Electron Microscope used by Ziemian et al. [46], the CamScan Series 4 scanning electron microscope used by Dawoud et al. [41] and the Hitachi TM-1000 used by Torrado et al. [76], to name a few.

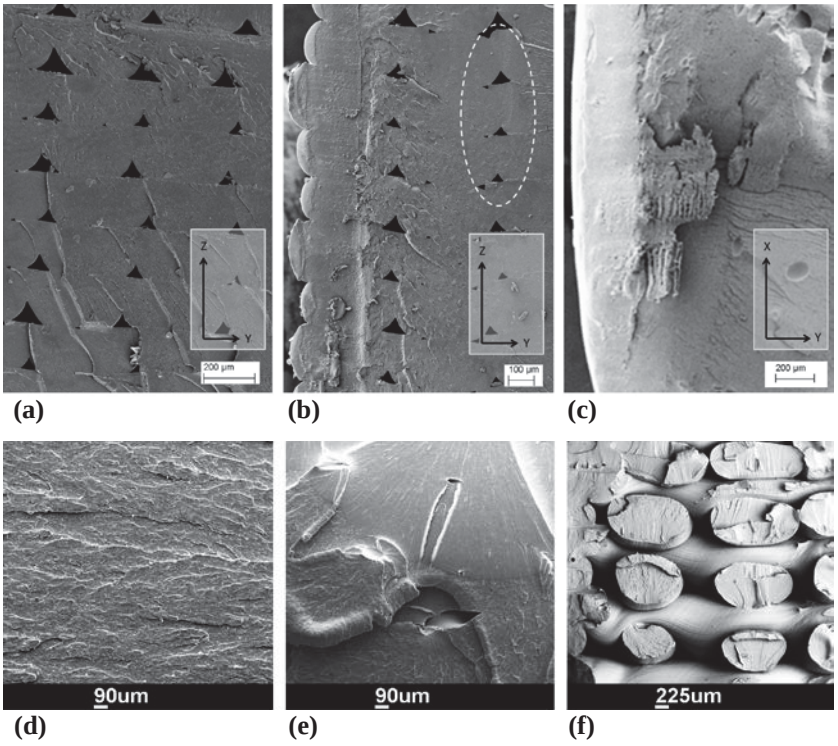

Figure 2.7 SEM micrographs of 3D-printed dumbbell specimens printed from ABS in, horizontal orientation (a), vertical orientation (b) and perpendicular orientation (c) [77]. SEM of the fracture surface of tensile samples of (d) injection moulded, (e) negative air gap and (f) positive air gap samples FDM [41].

As it is known that material strength is dependent on its microstructure, researchers use SEM in order to capture this for various test samples. SEM was used by Fatimatuzahraa et al. [21] to complement their analysis of samples destined for impact testing. Using this analysis

technique, they found that the microstructure of specimens printed with a ±45° raster orientation was more compact than those printed with a 0°/90°. SEM allowed Dawoud et al. [41] to confirm their results, along with tensile testing, that a positive air gap results in stronger parts, as stronger interfacial bonding is achieved. Their microscopy photos (Fig. 2.7 d, f) show that a positive air gap led to in-plane cylindrical raster's that barely touch, resulting in weak axial bonds. They conclude that the integrity of parts is achieved primarily by the subsequent layers bonding correctly rather than bonding in the same layer. SEM imaging can also help identify defects in the parts, such as in (Fig. 2.7b), which may or may not compromise mechanical properties [77]. A fracture surface of a homogeneous material could be an indicator of complete merger of filament together for shorter time of deposition (Fig. 2.7c). Torrado et al. [76] made use of SEM imaging to examine the fracture surfaces of their ABS tensile test samples that had various additives (styrene ethylene butadiene styrene and ultra-high molecular weight polyethylene) added to the build material. Ning et al. [45] examined the effects that adding various amounts of carbon fibre content and lengths had on the mechanical properties, and porosity, of ABS FDM. They noted that samples with 10 wt% carbon resulted in the lowest tensile strength. Using SEM micrographs, it was found that the 10 wt% carbon fibre specimen had the weakest interfacial adhesion between the carbon fibres and the thermoplastic material. It was also noted that as the carbon fibre content increased the porosity in the samples increased.

Scanning Electron Microscopy has become a vital tool in explaining the root cause of FDM mechanical properties. It has allowed researchers to more thoroughly understand how, and why, parts fail under specific loads, the failure mechanisms, and determine how different additives and other modifications to traditional ABS and other materials affect the part properties.

2.4. Fiber Bragg Grating

As the need to understand the properties of FDM parts and how they react to various external forces increase, new methods are devised in order to evaluate these responses. One such a method is the implementation of a Fiber Bragg grating (FBG) sensor in test specimens. FBG uses a single-mode fibre core that is laterally exposed to a pattern of intense ultraviolet light. As the fibre is exposed to the UV light, a permanent increase in the fibre core's refractive index occurs resulting in its grating. Grating being the fixed index modulation according to

the exposure pattern [78]. FGB sensors are optical sensors that can be used in order to measure strain, temperature and stress in specific locations of 3D structures. [73] The possible applications of FBGs in AM are not limited to FDM. These sensors have been employed in order to study fabrication processes as well as the materials used. It has also been used for the experimental testing of specimens. FBG sensors have been used in the study of solidification strains experienced by photo curable resins in micro-stereolithography. [79] They have also been used in Shape Deposition Modelling (SDM)[80] and Selective Laser Sintering (SLS) research for validation of their mechanical behaviour and design purposes [81, 82]. Tensile test specimen and a pictorial description of the steps taken to print the specimens in SLS system are shown in Fig. 2.8 a, b. Distorted and un-distorted spectrum profiles due to thermal expansion of the FBG are given in Fig. 2.8c. Optical sensors such as these have several advantages over more common measuring techniques such as low cost and weight, having a small size and not being very susceptible to electromagnetic interference [83].

Kantaros et al. [83] incorporated the use of FBGs in their research. They varied two process variables separately, the layer thickness and raster orientation, and used the sensor in order to monitor process-induced residual strain, temperature during the curing as well as evaluating the structural integrity of parts during intended use. Parts were manufactured 10 mm x 10 mm x 40 mm (width x height x length) with each of the specimens containing a 0.125 mm diameter optical fibre that was embedded centrally in the mid-plane of the specimens aligned axially. The optic fibre was equipped a 10 mm FGB that operated at a 1550 nm Bragg wavelength (the wavelength which is strongly back reflected). Based on research conducted by Colpo et al. [84], this experimental configuration would ensure that hoop and radial strains would be negligible when compared to the axial ones with the fibre and surrounding material having the same strains. Results obtained by Kantaros et al. [83] showed that the residual strain in manufactured specimens, with a layer thickness of 0.25mm, were lowest when the raster angle was 0° and was highest for the ±45° raster angle. With an increase in layer thickness from 0.25mm to 0.5mm, the measured strain for both the 0° and 90° raster angles were comparable.

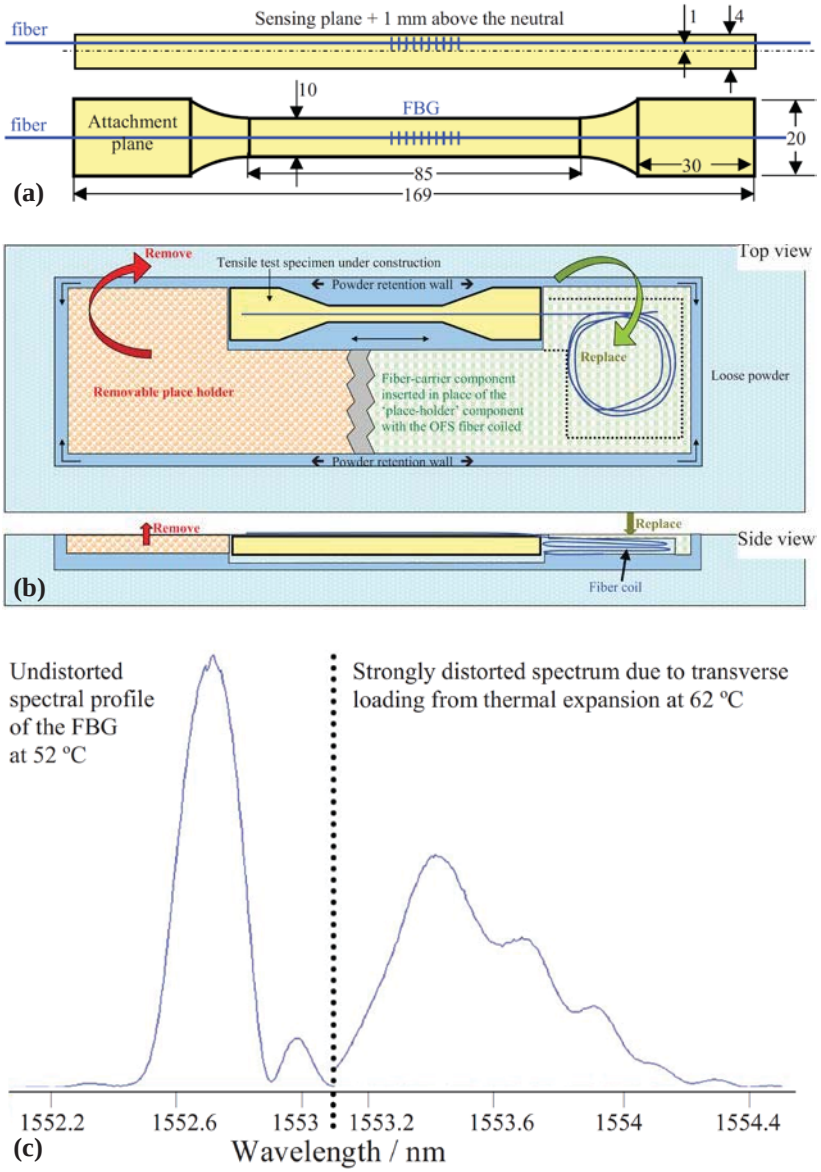

Figure 2.8 (a) Diagram of an ISO 3167 tensile test specimen with the location of the installed fiber (dimensions in mm). (b) Top and side views of the build area with the component under construction shown inside the powder-bed, surrounded by powder retaining walls. On the left, the removable place holder is shown. (c) Typical example of the strong changes in spectral profile and grating strength observed during thermal cycling of FBGs embedded in glass-filled nylon, indicating that this material combination is unsuited to the direct embedding of FBGs into the material during an AM process [82].

Economidou et al. [85] investigated the influence of varying the raster angles of their prismatic specimens and how subjecting them to thermal cycling would influence the thermal strain in the samples. The FBG sensor measuring length was 3 mm with a Bragg reference wavelength of 1550nm. The fibre diameter was 0.125mm and was acrylate coated. Specimens were fabricated with raster angles of 0°, 30°, 45°, 60° and 90° relative to the axial (long) direction. The wavelengths measured by the FBG sensors during the thermal cycling stages were used in order to calculate the thermal strains in the host materials. Parts were subjected to thermal cycles heating them up to 130°C. This temperature means the bulk

materials transitioned through their Glass Transition Temperature (T_g) of 94°C (104°C according to the Stratasys data sheet [86]) for P400-ABS. Due to the nature of the FDM process the presence of voids are unavoidable and as a result affect the fibre response to the applied thermal loading. The raster angle, however, also affects the void geometry in respect to the fibre axis. This means that the contact surface between the fibre and the bulk material are significantly affected by the raster angle. A raster angle having the fibre aligned parallel to the bulk material would allow for significantly more surface contact area as opposed to a raster angle that is 90° with respect to the fibre. Once the bulk material transitions through its T_g, the polymer chains mobility increase with the increase in thermal energy. During this phase, the meso-structure is altered and the void geometries change thus affecting the sensor-host material interface. This first thermal cycle acts as an enhancer for the interfacial bonding between the material and the sensor fibre ensuring a more uniform strain transfer from the polymer to the fibre [85]. Kousiatza et al. [87] also investigate the integration of FBG sensors in order to continuously monitor the strain fields build up and temperature profiles during the FDM fabrication process.

The uses of FBG sensors are becoming more popular as a method to investigate the strain and temperature profiles of FDM parts. It allows users to evaluate how different raster angles and thermal cycles affect the induced strain of FDM parts and adds another valuable insight into the FDM process and the mechanical properties of produced specimens.

2.5. Finite Element Analysis

Finite Element Analysis (FEA) has been widely used in engineering for the modelling and evaluation of engineering structures. It therefore makes sense to employ FEA analysis on FDM parts in order to help determine their mechanical properties as well as predict how they would deform or react to specific applied forces. A finite element model was developed by Zhang et al. [88, 89] to simulate the filament deposition process taking into account both the mechanical and thermal phenomena, analysing how stresses accumulate in the part and how it affects the distortion of the final parts. Taylor et al. [90] created a finite element model in order to evaluate the thermo-mechanical behaviour of ULTEM 9085 FDM tools that were subjected to elevated temperatures and pressure when used for vacuum assisted resin transfer moulding. Parts were manufactured and compared to the predicted responses from the FEA analysis. Ogden et al. [37] developed a database of ABS printed parts' strength characteristics

in order to allow FEA analysis to be done. The model was utilized to predict the anisotropic material characteristics of ABS FDM parts for various loading conditions. Physical samples of the FEA modelled parts were printed and their results compared to the predicted models. Rezaei et al. [36] has recently developed a solid FE model to obtain stress-strain response of PLA cellular lattice structure printed with FDM. The lattice structures were printed with suitable processing parameters and tested in tension and compression. These tests revealed asymmetric behaviour in the test specimens, which was similar to the predicted results from the FE model.

The use of FEA analysis in the prediction and optimization of FDM parts is becoming more common, however the FDM parts are known to exhibit anisotropic properties making it harder to predict their behaviour. Due to the orthotropic nature of FDM parts, researchers have investigated the use of compliance matrices in order to help define the mechanical behaviour of orthotropic parts. It is assumed that the FDM parts exhibit linear elastic behaviour with the relationship between stress and strain based on Hooke's law stating that for small strain, stress is linearly proportional to the strain. A material can be considered elastic when the equivalent stress is less than the yield stress in tension according to Von Mises criterion. Based on the assumption that FDM parts behave in a fully linear manner, for the complete determination of material mechanical properties, all 36 compliance matrix S (Eq. 3) components need to be determined [19, 67, 91, 92].

$$\begin{pmatrix} \varepsilon_1 \\ \varepsilon_2 \\ \varepsilon_3 \\ \gamma_{23} \\ \gamma_{13} \\ \gamma_{12} \end{pmatrix} = \begin{pmatrix} S_{11} & S_{12} & S_{13} & S_{14} & S_{15} & S_{16} \\ S_{21} & \cdots & \cdots & \cdots & & \vdots \\ S_{31} & \cdots & \cdots & & & \vdots \\ S_{41} & & & & & \vdots \\ S_{51} & & & \cdot & & \vdots \\ S_{61} & & & & \cdot & S_{66} \end{pmatrix} \times \begin{pmatrix} \sigma_1 \\ \sigma_2 \\ \sigma_3 \\ \tau_{23} \\ \tau_{13} \\ \tau_{12} \end{pmatrix} \quad (3)$$

However, in the case of orthotropic materials which are materials having three mutually perpendicular symmetry planes, the compliance matrix requires only nine unknown components. This means that nine independent constants are required where three of these are the Young's modulus (E_i), three the shear modulus (G_{ij}) and three Poisson's ratios (ν_{ij}) [42, 67, 91]. Experimentally, the nine independent values of the stiffness matrix were determined by Espin et al. [67] by building 5 samples for each of the six different orientations shown in Fig. 2.6. The stress strain diagram was determined as set out by the ASTM 638.

Ogden et al. [37] chose a "plasticity von Mises" model for their FEA modelling. Each print orientation that was tested had a stress-strain curve chosen based on its closeness to the average values of its yield strength, toughness, and modulus of elasticity. The values predicted based on the FEA model using SolidWorks plasticity von Mises model were accurate to within 6% of the experimental values. Espin et al. [67] evaluated their test sample using both an orthotropic and isotropic model approach and found that both models were reasonably accurate when compared to the actual testing completed with mean deviations of 7.3 % and 7.12 % respectively. It should be noted that even though the use of isotropic models is easier, since there is no need to orientate the material properties, the orthotropic model is more realistic when a part reaches its yield tension. Results obtained by Bellini et al. [19], through the use ANSYS to obtain stiffness matrix, showed that part failure can be underestimated when the part is designed based on isotropic material properties. Despite the fact that their test samples had similar Von Mises values, it should be noted that these values are an "average" of the stress components in every direction resulting in the resistance to failure possibly being over-evaluated when using an isotropic model. Other researchers such as Li et al [90] have used an FEA analysis tool in order to help predict how sparse and solid FDM tool samples would respond to use in real world scenarios.

2.6. Glass Transition Temperature:

The glass transition temperature (T_g) is a phenomenon observed found only in polymers. It is the observed behaviour of polymers when a plastic container is left in cold environments and cracks more easily as opposed to summer when it is kicked. The T_g can be described as the temperature (different for every polymer) below which a polymer exhibits more brittle material behaviour. Depending on the intended application, parts are used either below or above this T_g. Polymers such as polystyrene is used above its glass transition temperature as a hard plastic. Rubber elastomers (polyisoprene and ABS) are used above this temperature particularly for applications such as FDM where they are rubbery and flexible.

It is important to distinguish between the glass transition temperature and melting point of a polymer. Glass transition only occurs in polymers in the amorphous state where as melting is found in crystalline polymers. It is common for these materials to have both amorphous and crystalline domains. This means they have both a melting point and T_g. The polymer chains that are responsible for the two mechanisms differ. During the melting of a polymer, it will

continue to increase its temperature until the melting point is reached. Upon reaching the melting point, the polymers temperature will stay constant until it has completely melted. When complete melting has occurred, its temperature will again start to increase. The observed stagnation occurs because of all the energy going into the polymer for melting. This is known as the "latent heat of melting."

When an amorphous polymer such as ABS reaches its T_g, the heating rate depends on the heat capacity (the required amount of heat to raise the temperature of 1 gram of polymer by 1 degree Celsius) of the polymer. When comparing the temperature responses of a polymer reaching its T_g and melting point, it will be noted that the temperature of the polymer continues to rise when the T_g is reached. This is because there is no latent heat of glass transition. Above the T_g, there is a difference in the rate at which the polymers temperature rises. As a polymer transitions through this temperature, its heat capacity increases. [86, 93]

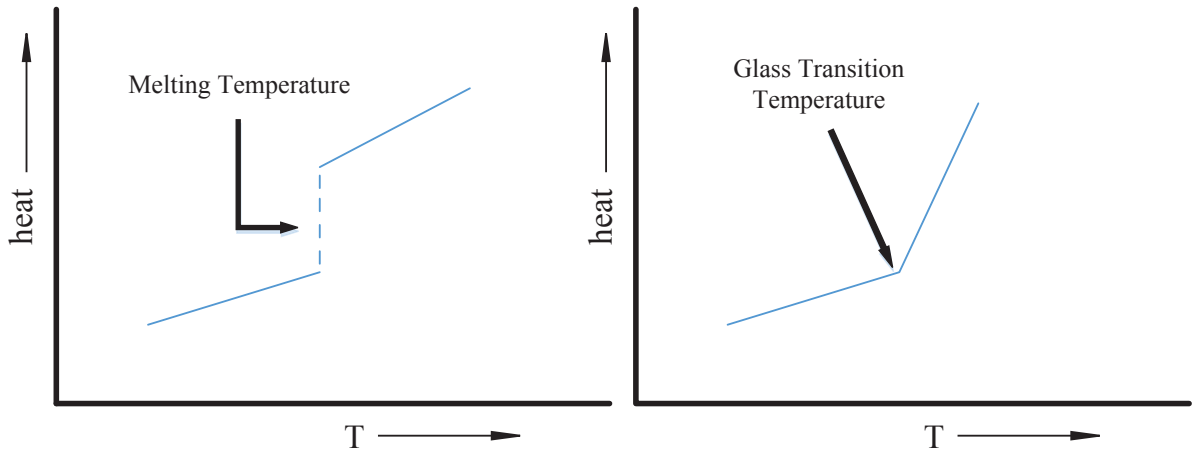

Figure 2.9 A heat vs. temperature plot of left; for a crystalline polymer reaching its melting temperature; right: An amorphous polymer reaching its T_g. [93]

Fig 2.9 depicts the stage of crystalline polymers where its temperature does not increase as more heat is applied as opposed to the continual increase in temperature of the amorphous polymer. The increase in heat capacity results in higher heat requirements for the temperature to continue to increase. Polymers used in FDM systems normally have a low T_g. With the particular property requirements for successful fusion at relatively low T_g temperatures, FDM machines currently have few polymers that are compatible with this platform [94].

2.7. Retrofitment of Machines as 3D Printing Systems:

The retrofitment of machines for a different purpose or for use with different software is not a new concept as exemplified by Karunakaran et al [95, 96]. The research team retrofit a CNC machine with a welding torch with the goal of creating a hybrid machine operating on the same additive manufacturing principles as FDM in combination with the machining capabilities of a CNC machine. Their FDM metal welding system, named "ArcHLM", manufactured parts through a hybrid AM, subtractive manufacturing, process. This allowed end use parts to be manufactured with far less material as the part did not start out as a solid block of metal that had to be milled to shape. Shaikh et al. [97] used a retrofit CNC machine to prove the effectiveness of their Hilbert Curve based toolpath for machining and production purposes. Similarly, Suryakumar et al [98, 99] used a retrofitted CNC machine for the investigation of the mechanical properties of parts manufactured through a hybrid weld deposition and milled process. They used this machine in order to develop build strategies for the rapid manufacture of components of varying complexities. Another retrofitted CNC machine created by Song et al. [100] was used in their hybrid manufacturing machine. A gas metal arc welder deposited metal beads and a finishing milling operation completed the part. Xiong et al. [101] added plasma deposition capabilities to a CNC machine for the creation of their hybrid manufacturing system. Vaidyanathan et al. [102] retrofitted a Stratasys FDM Modeller with a high-pressure extruder head. The head, capable of extruding ceramic feedstock, was used for their extrusion freeform fabrication process.

The retrofitment of machines, particularly CNC machines, for use in FDM type processes are common. However, the retrofitment and rejuvenation of commercial FDM machines has yet to be successfully completed.

2.8. Summary

Testing and characterization of fused deposition modelling has been widely undertaken using various techniques. However, no unified standard yet exists for mechanical testing of 3D printed parts; researchers normally rely on bulk material standards or modify them to capture behaviour of FDM part failure. As FDM specimens exhibit particularly anisotropic material properties, and are sensitive to loading conditions, their preparation and orientation for

mechanical testing are pertinent. The most critical factors affecting the parts strengths are raster orientation, air gap and raster width.

Tensile properties directly depend on the raster orientation and result in the strongest parts when the tensile load acts in the direction of longer raster paths. However, the same is not always true for compressive loads where the raster orientation have a very small influence on the compressive loads.

SEM imaging allows users to support theories on why, and how, FDM specimens will (or did) fail as it reveals information on the external morphology, crystalline structure, and chemical composition (using energy dispersive x-ray spectroscopy) of parts. SEM has been used to study inter-layer bonding and effect of road overlapping on the properties, but no study has been conducted with in-situ tensile testing to actually relate the mechanical strength to bonding or diffusion of polymer from one layer to the other immediately above or below. In-situ tensile testing can better expose weaknesses of the bonding process in the context of mechanical strength.

Novel methods like fibre Bragg grating are useful, but limited to only a few types of characterization. Properties such as strain, temperature and stress can be measured inside 3D objects. However, these properties alone are not enough to design parts for strength in real world applications. Ideally a part printed fully with an embedded fiber inside the extruded roads can reveal many interesting aspects of FDM. This type of part printing would be challenging from many aspects e.g. forcing the fiber without damage through the nozzle.

With the knowledge gained from mechanical testing and optical analysis, research has been done on the prediction of FDM part quality based on the selected levels of the input variables. Finite element analysis integrated in the design or printing process seems very promising to optimize the strength of FDM part for functional use. However, the work so far is in its early phases and need be further optimized for different materials and FDM machines particularly those in the low-end market.

From this review, we can conclude that the need for a test standard is clear and even though it has become more common for researchers to investigate several aspects of parts through doing a combination of tests such as tensile and compression or tensile and bending tests, it would be beneficial for a more complete test approach to be taken for the characterization of FDM parts as the applications of different parts will vary. Due to the nature and freedom that

users have in creating interesting shapes with various dimensions that cannot be manufactured in any other way other than through additive manufacturing, creating printing rule sets not based on just a single or two mechanical tests would be advantageous in the advancement of this technology to a standalone manufacturing method. We envisage that the predictions models (e.g. FEA) will play a major role in the future of FDM. These will allow for a rule base to be built where parts could be analysed and the print orientation and input parameter setting chosen based on part application and prioritised output parameters.

It has been found that no open source commercial 3D printer currently exists having the capabilities to open new avenues of research. Furthermore, there are no retrofitted units that can print with the same mechanical resolution and capability as standard machines. This led to the identification of the need for a machine capable of using any extrudable feed stock with open control of all variables that affect the print quality and mechanical properties. The review also showed that mechanical testing of FDM parts is well documented, however, longitudinal studies on the temporal effect on these parts as well as machine age has yet to be studies. All testing has been one of manufacture and testing of samples. The use of SEM is also well documented but the technology has not been applied for an in-depth investigation of the fracture and topographical surfaces of FDM parts.

3. Retrofitment and Characterization of Vantage Fused Deposition Modelling System

3.1. Introduction

With the current rate of expansion of FDM machine variations along with the increase in their accuracy, it has become difficult and expensive to have a machine that is up to date with current software and printing materials. Companies such as RepRap have created printing systems that are open-source, customisable and user updateable. Even though the core design of 3D printing systems remains unchanged, larger companies such as Stratasys require customers to regularly upgrade after several years as the machines become outdated and unsupported due to age. These companies also rely on closed-form machines, often requiring the customers to pay large amounts to unlock additional material option. As a result, retrofitment of industrial type 3D printing machines would be a valuable option for researchers. The retrofitment and modification of FDM printers are easier as they do not rely on extensive laser systems and special materials. Once retrofitted, these would allow various forms of research to be conducted including the testing of different materials, their mechanical properties and having almost complete control over the process variables used for printing of parts.

From the preceding literature review, it is clear that the repurposing of machines for AM is not a completely new concept; however, these modifications are normally applied to CNC machines. This research presents the retrofitment of an “out of date” Stratasys Vantage X machine in order to allow users control over the process variables of printed parts. The system has been retrofitted with a newly designed power supply system made up of a power supply and power supply control board. The extruder controllers are replaced and the firmware based on the Makerbot “Thing-O-Matic” firmware is modified for this machine. A new control board using an Arduino Mega is designed for the printing control system and the stock feed system is modified to accept printing material on rolls. Open access to the

filaments used in the machine widens the research capabilities available to the user. It can also serve as a model for other similar machines to be made open source. As per our knowledge, this work is first ever on the full retrofitment of an old FDM machine. The retrofitted machine is named as “OpenVantage” for easy reference.

This chapter is divided into four sections. Section 2 gives details of the hardware design and modifications including power supply, extruder head, motherboard, and front panel controller. Section 3 is dedicated to firmware development while section 4 describes details of the software to control the machine. System calibration and testing are given in the section 5 and 6, respectively. Experiments and results are discussed in the section 6.1 which precedes the summary. This chapter is based on the published work with permission of Springer.

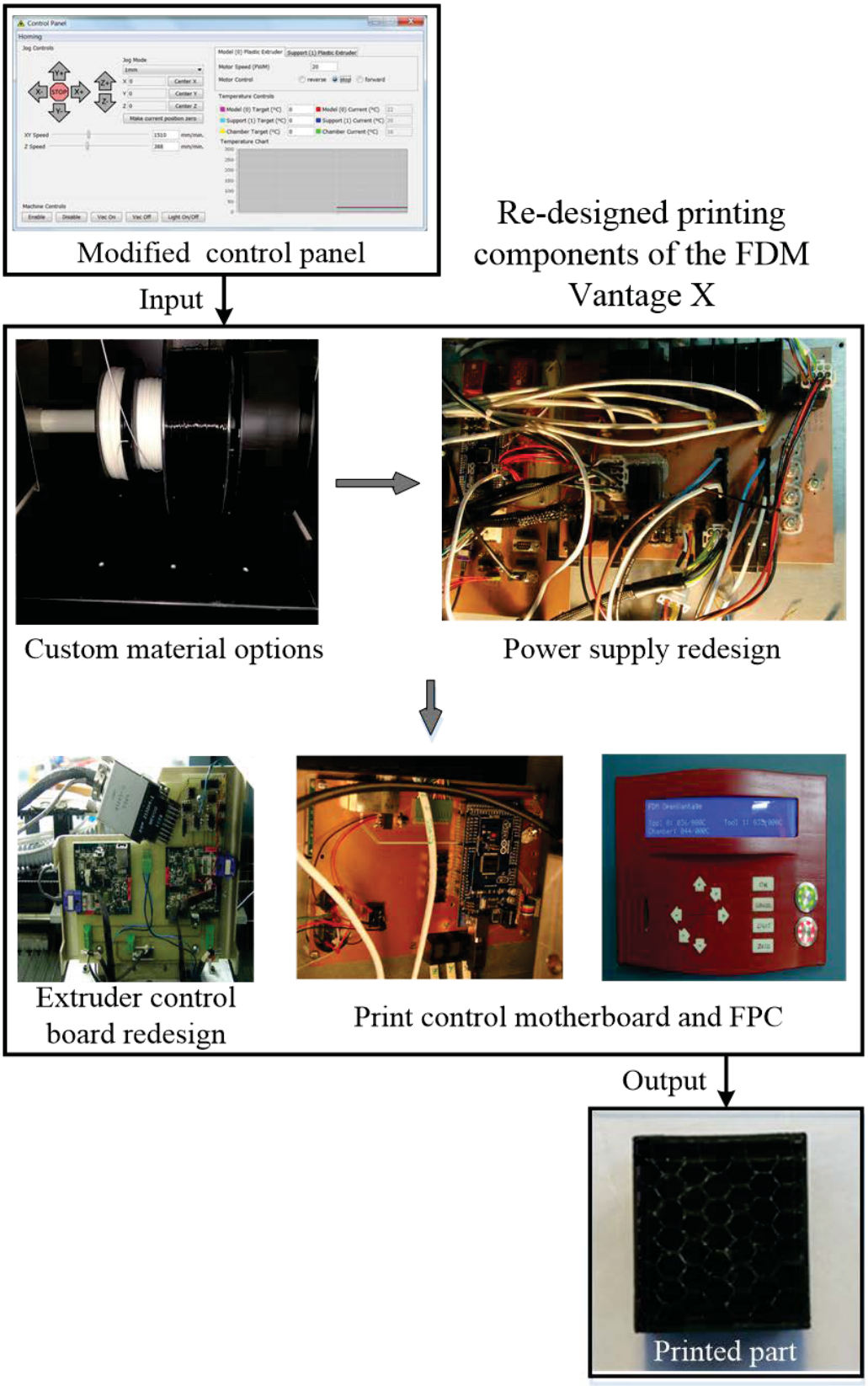

Figure 3.1 Print process layout with retrofit components

3.2. Hardware Modifications

Machine retrofitment can be extremely complex or reasonably simple depending on the amount of modification required in order to achieve the desired performance. In the case of the Stratasys FDM Vantage X, that has been retrofitted for this research, a considerable amount of hardware and software modifications are required in order to allow the user full control over the materials that the machine can utilize, extruder speeds, deposition rates (speed that the print head moves) as well as various other parameters. A block diagram with actual system photographs show the print process layout with the retrofit components in Fig. 3.1. A photograph of the retrofitted system is shown in Fig. 3.2. The details of the major modifications are given below.

3.2.1. Electrical Design

The original Vantage design had a 230V phase-phase working voltage with a delta configuration. In New Zealand, however, the standard three phase is 230V phase-neutral or 415V phase-phase. This means in order for the printer to operate, a heavy-duty transformer on a separate trolley is required for the supply voltage to be converted to a suitable level.

Figure 3.2 Retrofitted Stratasys FDM Vantage X system

3.2.1.1. Power supply

Due to the inconvenience of the required power supply and size of the transformer, the power supply is redesigned and the machine is converted to a ‘star’ configuration. This would allow the printer to be plugged into any 3-phase power supply in New Zealand. The conversion to a ‘star’ configuration requires a connector change from 4-core (3P&E) to 5-core (3P, N&E) as well as an additional terminal block connecting the neutral to the filter. A redesign of the PCB is also required in order to switch phase-neutral rather than phase-phase. The power supply PCB is redesigned and split into two separate PCB’s: A Power Supply Control Board (PSCB) and Power Supply Board (PSB).

The design philosophy follows that of the original equipment manufacturer (OEM). Fig. 3.3 shows a photograph of the redesigned power supply. The incoming supply through the filter is connected to the contactor and L3 connected to the back panel main switch controlling the supply to the PSCB. A Crydom MCX240D5 solid-state relay (SSR) is used to power the UPS from the PSCB as well as a small Point of Load (PoL) 24VDC power supply for the contactor. The PSCB provides the signal to the contactor and the gate voltage to a FET for switching the contactor. The stepping motors are powered from the fused side of the contactor return side. Heater supply loads are distributed across the three phases and switched using a Crydom D2425 SSRs.

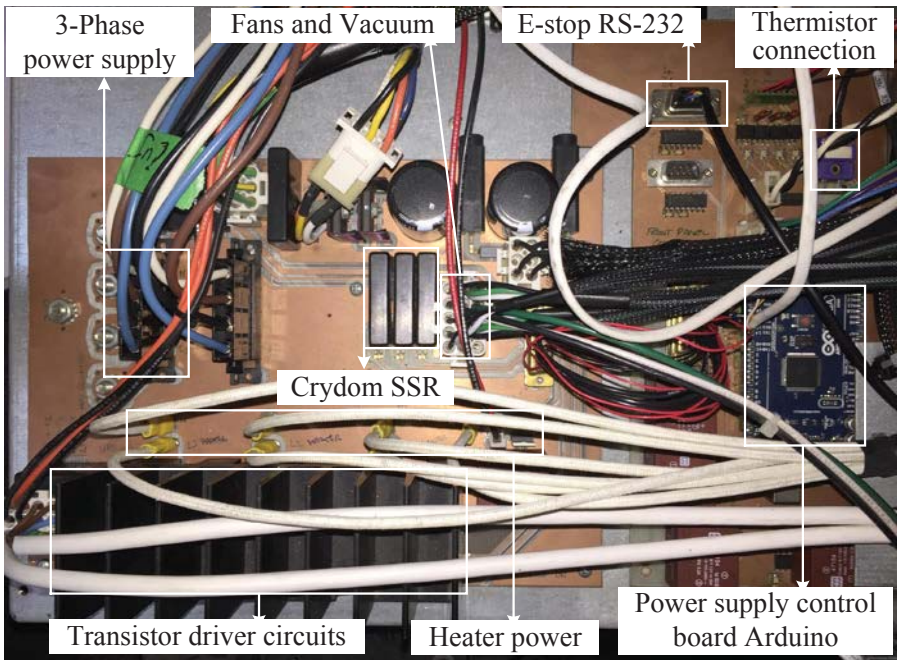

Figure 3.3 Power supply redesign showing main components, connections, and control board.

The secondary coils of a power transformer found in the bottom of the printer is used in the development of the High Voltage Direct Current (HVDC) supplies for the extruder head using GBU806-HB bridge rectifiers and smoothing capacitors for rectification of the power supply. The resulting PSB and PSCB are designed using DesignSpark PCB software. These PCBs are manufactured using a LPKF PCB mill. The digital control board design is based around an Arduino Mega board which is powered by a redundant 12V supply. The primary supply is connected to L3 from the PSB and the secondary to the UPS return from the PSB with the two supplies tied together through a pair of 1N4001 rectifier diodes and connected to the input of a 4N35 opto-insulator. The output of the opto-insulator is connected to the Arduino Mega along with an LED indicating the presence of power on each. L1 and L2 are connected to two Myrra 47154 PoL power bricks allowing the Arduino Mega to monitor the connection health of the 3 phases. The Arduino is also responsible for monitoring four DC supplies, the 24V supply to the motherboard and extruders as well as the three 60V supplies to the Stepping Motor Drives.

The Power Supply Board and the Power Supply Control Board have been designed so that the oven temperature could be monitored by the PSCB and the control signal provided to the Power Supply Board as it is used for controlling the oven heater SSR's.

3.2.1.2. Extruder head

The OEM used a single PCB in order to control both extruders with a PIC micro-controller and a Xilinx FPGA. The two 100-ohm heating elements with embedded thermocouples were connected in parallel and switched using IRF644 MOSFET's. The same MOSFET setup is used in order to drive the support material extruder up and down when required with the extruders being driven by Faulhaber 2342L036, 36V DC micro-motors attached to a Faulhaber 23/1 planetary reduction gearbox. Each motor has a Faulhaber IE2-512 encoder providing 512 pulses per revolution. For the retrofitment of this printer the extruder control board is broken into two separate sister boards mounted to a motherboard on a back plate along with the HVDC components (Fig. 3.4). The new extruder boards utilize an ATMega328P microcontroller operating at 16MHz. The original extruder motors and DC motor controllers are used as they are perfectly fit for the extrusion process and only require the working voltage of the capacitors on the motor control side as well as the transient voltage suppressor attached across the motor outputs. Serial communication between the

extruder and motherboard uses a RS-485 multi-drop bus allowing a single host (the motherboard) to communicate with multiple slaves (extruders and power supply).

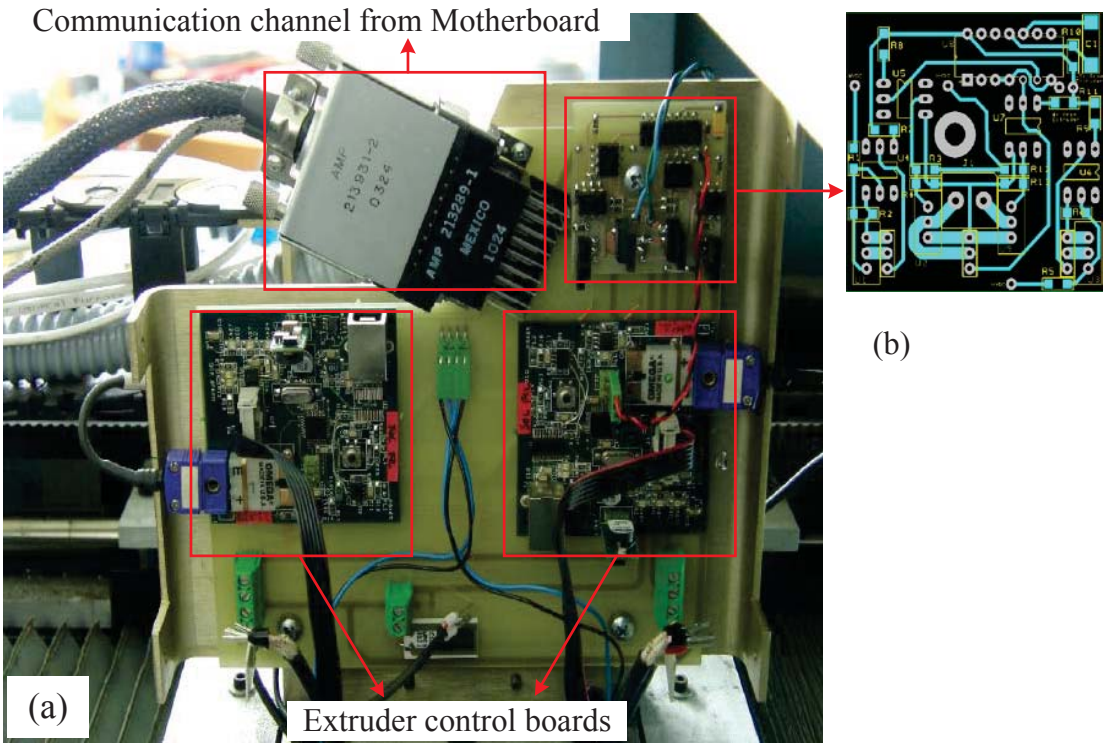

Figure 3.4 (a) Controller board with extruder boards mounted. (b) PCB schematic of the solenoid voltage switching/opto-isolator board.

3.2.1.3. Motherboard

The motherboard design is based on the Makerbot v2.4 motherboard for the Makerbot Thing-O-Matic. Even though the original OEM positioned the I/O PCB in the bottom of the machine, this retrofitment positions the motherboard behind the front display panel as this would allow easy access to the SD card slot and minimise the amount of wiring needed between the motherboard and the FPC. Three PCB's have been used for the FPC/Motherboard combination. A keypad interface PCB, the motherboard itself (Arduino Mega 2560) and a third board for the SD card slot that could be mounted just behind the front panel for SD card insertion. The original panel had two LED's which are removed allowing for the implementation of an extra button to control the chamber lights inside. The original display also makes use of a 4x40 LCD display around which the front panel is designed where the MakerBot design uses a 4x16 LCD display. In order to use the larger Stratasys

FPC display, an equivalent LCD display is used based on the same Hitatchi HD44870 chipset used by the MakerBot system. The larger display requires an extra I/O pin in order to drive a second 'Enable' line.

A photograph of the motherboard is given in the Fig. 3.5a while Fig. 3.5b shows a schematic of the connections between Arduino Mega controller board and the units it controls for the printing process.

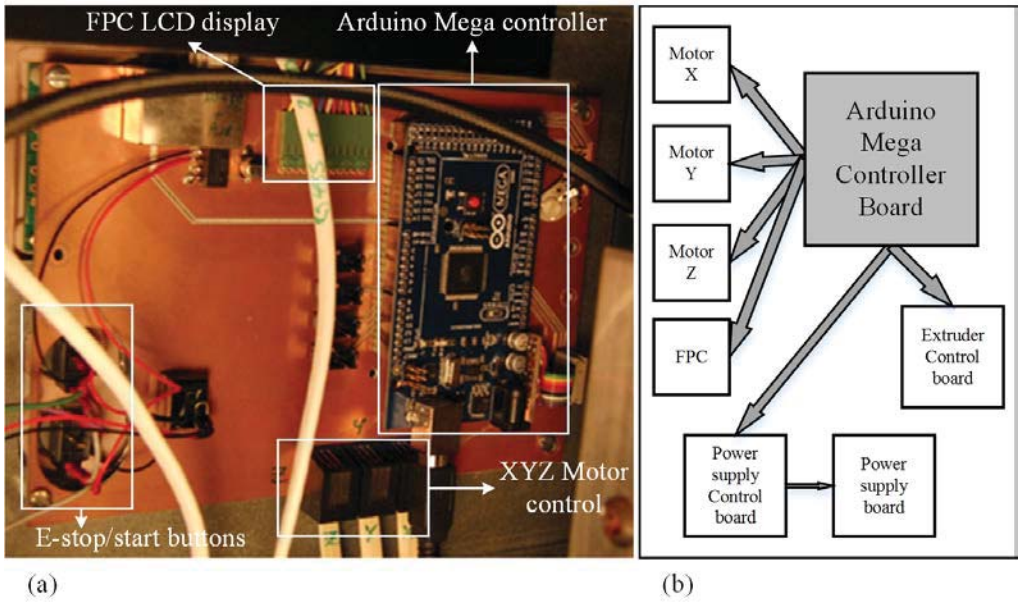

Figure 3.5 Motherboard layout with Arduino Mega controller (a) and connection diagram (b).

3.2.2. Front Panel Controller

The FPC on the FDM Vantage X machine uses a 4X40 LCD display with navigation buttons as well as a green start and red stop button. For this retrofitment, the original panel's physical form is kept, however the basic button structure and interface is based on the MakerBot design. The FPC is re-designed in SolidWorks utilizing the current 4X40 display size and a button layout that is more suitable for the MakerBot design. The SD card interface is moved to the FPC allowing easier access. The panel and buttons are 3D printed on a TPM3000 Selective Laser Sintering system with nylon and spray painted to get the colour shade as shown in Fig. 3.6.

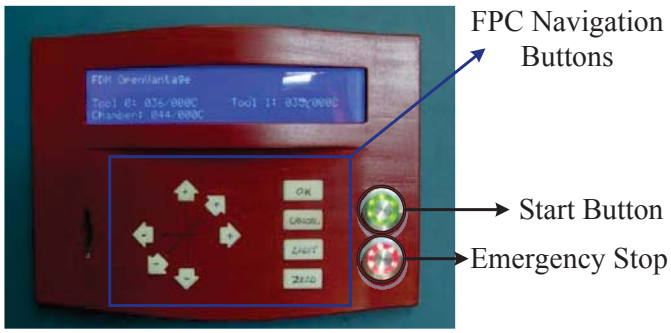

Figure 3.6 Front Panel Display Layout

3.2.3. Other Physical Modifications

The cartridge controller is removed from the machine. This would allow the use of any feedstock that could be wound onto drums. The small compressor and associated receiver with pressure regulation devices are also removed as they are no longer required with the removal of the cartridge controller. Fig. 3.7 shows commonly used FDM materials that can be used with the retrofitted machine. The original industrial PC of the machine is no longer required and is therefore removed along with the UPS as this is unserviceable. The UPS is replaced by a smaller model, a Blazer 800, in order to provide backup power to the microcontrollers. The space left after removal is utilised to house the power supplies for the axes stepping motor drives.

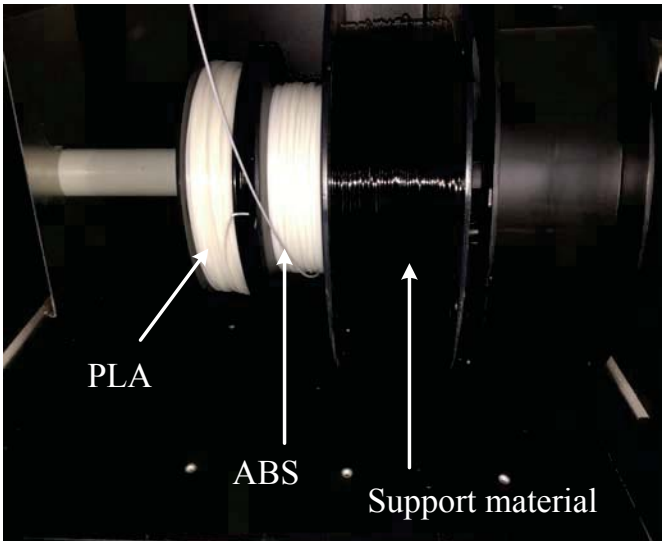

Figure 3.7 Custom loaded print material.

3.3. Firmware Development

The firmware for this printer is based on the v3.1 of the MakerBot Firmware. This version of the firmware is used as it is the last version that allows control of extruder with DC motors in contrast to Sailfish and Jetty that use stepping motors for extruder control. The main modification to the motherboard firmware is the interface. The original interface is based around the MakerBot interface. The addition of the button to turn the oven lights on/off as well as the display being changed from 20x4 to 40x4 required slight modification of the original firmware. The required changes in the base firmware for extruder, power supply and heater controller are discussed below.

3.3.1. Extruder Controller

The extruder code remains relatively unchanged with certain areas of code being removed because of the change of architecture. As an example, due to the reallocation of the oven temperature control to the power supply, the build platform code is no longer required. The follow code segments are removed as they are considered obsolete.

- Software servos (not used)
- Cooling fan (controlled by power supply)
- Thermistor tables (thermocouples are exclusively used)
- Platform heater and thermistor (controlled by power supply)
- Automated build platform (not available)

3.3.2. Power Supply Controller

Due to limitations on the available pins on the motherboard Arduino Mega, the power supply firmware has been implemented as an additional “tool” on the existing RS-485 bus used by the motherboard for communication with the Extruder Controllers. This means making the power supply controller Tool 2 in the firmware to be addressed as T2. The RS-485 is a half-duplex differential protocol requiring only two wires. In this retrofitment the RS-485 board is manufactured and mounted underneath the Arduino controller on the motherboard allowing control of the extruders, oven, and the power supply controller. The RS-485 bus acts as the main control channel between the three Arduino’s used. The firmware for the power supply is based on a modified version of the Extruder Controller firmware.

3.3.3. Heater Controller

Since the Power Supply Controller firmware is based on the Extruder Controller firmware, the code required for the heater control is already there; the difference however is in the control algorithms. The extruder heaters are DC and can be turned on and off whenever required. The oven heaters are AC and are turned on or off using a SSR on each phase meaning they can be turned on at any time but only turned off at a zero-crossing point in order to minimise power dissipation in the semi-conductor device. With each cycle having two crossing points, with 8-bit control, the window time for the PWM of the oven is set to 2.55s. Testing showed that the default oven PID control was incorrect as the temperature level didn't stabilize but oscillated between +7°C above and 3°C below the set point as shown in Fig. 3.8a. The PID was modified resulting in the oven temperature stabilising with a ± 1°C variation around the set point as shown in Fig. 3.8b.

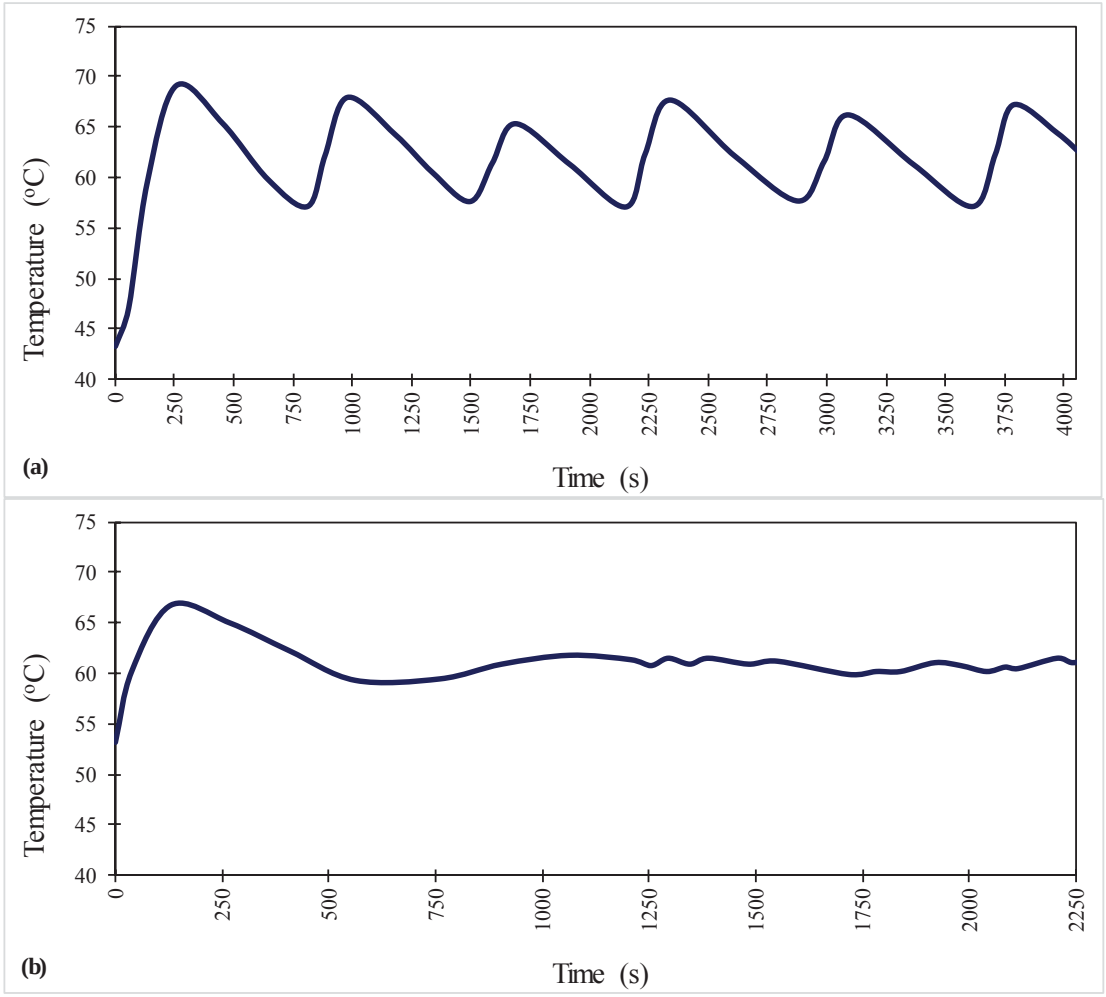

Figure 3.8 Oven temperature fluctuation with original PID settings (a) and with modified PID settings (b).

3.4. Software Design

The de-facto software for controlling open source 3D printers is ReplicatorG [103] which can drive MakerBot, RepRap, CupCake CNC and many other open source printing and machining systems [104, 105]. As our retrofitment is based on the MakerBot hardware and firmware, the obvious choice of for the control software is ReplicatorG. ReplicatorG 0040 (the latest version) and 0037 were initially tested to using the ReplicatorG control panel to control of the motor speeds and directions as well as the heater set point. These tests resulted in success however testing with G-code revealed some problems. Upon execution of code "M108 T0 256" the extruder on tool 1 did not activate as expected as ReplicatorG converted the S3G code "M108 T0 256" to "0x86 0x00" (tool change to index 0) and "0x89 0x1F" (disables all drives). The machines.xml definition disabled all drives at the end of every build and so the M108 command was being translated to select tool 0 rather than setting the motor speed. However, testing with an earlier version (version 0037) of the ReplicatorG worked fine and it was selected to use with the machine. It is noteworthy that 0037 works with DC motors which are used in Vantage X extrusion system while 0040 expects stepper motors in the extruder. During the power supply firmware development, the slave ID of the Power Supply Controller was set to 127. Fig. 3.9 shows the layout of modified 0037 control panel.

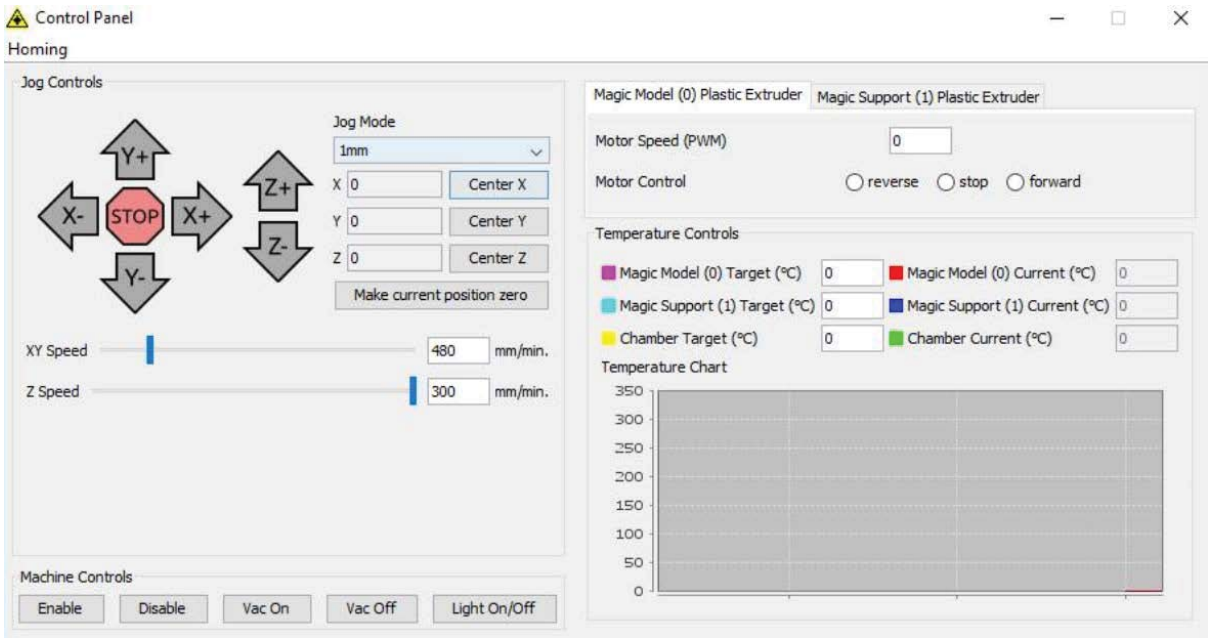

Figure 3.9 Modified ReplicatorG 0037 control panel layout

For the G-code generation Slic3r [106] has been found more efficient and reliable than the built-in generators in the ReplicatorG. Once the G-code is generated it is run through a script written to slightly modify specific G-code lines in order to effectively control the machine. The platform set-point and monitoring are changed to monitor and control the oven temperature and display in the temperature monitoring window. Since the Stratasys machine doesn't include an automated build platform (ABP) like the Thing-O-Matic does, the control panel window file is modified to toggle the oven lights on/off instead of controlling the ABP. The control panel also had two buttons added in order to turn the vacuum pump, responsible for holding the work piece on the table, on and off. The machine options menu is modified and an oven/chamber tool tab is added with the PID control settings.

Upon completion of the software, firmware and hardware modification of the printer, additional calibration had to be completed in order to ensure correct operation.

3.5. Machine Calibration

With the Stratasys retrofitment being based on the Thing-o-Matic from MakerBot, many necessary calibrations are required. The Thing-o-Matic is based on steppers (all driven at $1/8^{th}$ steps or 1600 pulses/revolution) directly driving a belt using a small timing gear (10.82mm) on both the X and Y axes and a direct lead screw on the Z axis. The Z axis requires 200steps/mm and the X and Y axes only require 47 steps/mm. The belt design on the Stratasys machine however resulted in the Y axis moving only half that of the X axis. The system was measured and determined that the X axis required 70 steps/mm and the Y required 35 steps/mm. Due to the gearing system used for the Z axis, it was determined that only 1260 steps/mm were required. This means that the theoretical resolution of the X, Y and Z axes is 0.014 mm, 0.028 mm and 0.0008 mm, respectively. The original quoted resolution of the Stratasys FDM Vantage is 0.127mm in all three axes. As a result, the above setting produced a machine with a higher resolution than the original. However, in the Y axis the machine would still be inferior to the MakerBot Thing-o-Matic. Considering the installed stepper drives being capable of microstepping up to 51200 microsteps/revolution, the individual axes are re-calibrated using alternative settings in order to improve overall performance. The re-calibration is aimed at creating a system that is accurate in the region of 5-micron resolution.

Based on the new calibration settings, the machine has a theoretical resolution of 0.0045mm in the X and Y axes and 0.0032 in the Z axis. This far exceeds both the Stratasys FDM Vantage X and the MakerBot Thing-o-Matic which this machine is based on. With the completion of calibration, the maximum build envelope is determined based on the midpoint between the two extruder heads as the reference. The build envelope is set to 440mm x 370mm x 415mm in the X, Y and Z axes, respectively.

After the completion of the calibration, it is necessary to determine the home position of the printer based on the X, Y and Z limit switches. The home position is determined using the minimum of each of the three axes (the front left corner of the printer). The centre position (0, 0, 0) is determined using the point between the two print heads. As the Z axis only had a limit switch at its maximum, the minimum limit is identified as the extruder height. The position 0, 0, 0 is set by moving the print head to the middle of the print bed and driving the table up until the extruder nozzle just touches the print base. This position is set using the "make current position zero" button on the control panel. The home position is saved to the motherboard EEPROM using G-code (m131 X Y Z). This allows the machine to be reset by sending each of the axes to the home position and then recalling the offsets stored as above allowing the machine to move to the 0, 0, 0 position to start printing.

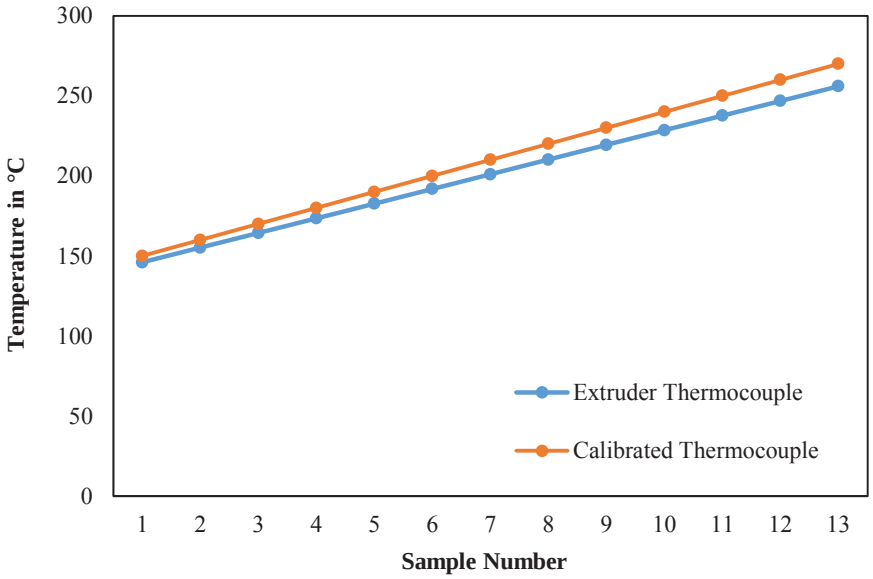

Figure 3.10 Temperature error measurement of the extruder.

Through further testing it was determined that the extruder heater temperature being reported by the embedded thermocouple did not match that of an external, calibrated thermocouple, connected to a Fluke 52, dual input digital thermocouple meter. Testing showed that at 150°C

the extruder thermocouple only reported 146°C and at 270°C the extruder thermocouple reported 256°C. A linear relationship was found between the reported and actual temperatures (Fig. 3.10).

Suing the high and low temperature a correction factor is calculated. The measured raw values from the thermocouple are converted to correct values using Eq. 1.

$$T_{corrrected} = (T_{raw} + 9.27)/1.09 \quad (1)$$

Due to the difference between reported and actual temperatures the default PID setting also need be changed to with the original Arduino PID development done by Brett Beauregard [107]. With this modification, the heaters returned to normal operation. Table 1 shows the parameters used for the FDM Vantage PID control.

Table 3.1 PID parameters used in the retrofitted Vantage X

Parameter	**Default MakerBot**	**FDM Vantage X**
K_P	7	5
K_I	0.325	5
K_D	36	1.5

The hard-coded shutdown limit for the extruders in Vantage X is 280 °C. As one of the main purposes for retrofitment of the machine is to enable various material to be printed having different melting temperatures, the hard limit of the machine is increased to 350 °C.

3.6. Printing Experiments

With the completion of the retrofitment, testing has to be done to ensure the correct operation of the printer. The four main process variables that could potentially be altered are: Temperature, Layer Thickness, Flow Rate (extruder motor speed) and, Feed Rate (X/Y axis motor speed).

As this machine is retro fitted for the purpose of printing various material meaning that the optimal settings for the above parameters would vary, the initial testing of the machine was

done using the Stratasys polycarbonate / acrylonitrile butadiene styrene (PC-ABS) supplied with the printer. A layer thickness of 0.1mm was chosen as it would demonstrate the higher resolution capability than that of the original machine (0.127mm).

3.6.1. Effect of Process Parameters

Before any other testing can be completed, the correct extrusion temperature has to be determined for the material being used. The initial starting temperature was 260°C and the temperature was incrementally increased by 2°C up to 270°C. At each increment the extruder was turned on and the extruded filament sample collected and photographed under an optical microscope (BS-6020RF/TRF) with a CCD camera (MC50, Mshot). A mosaic of photographs is shown in Fig. 3.11 with corresponding extruder temperatures.

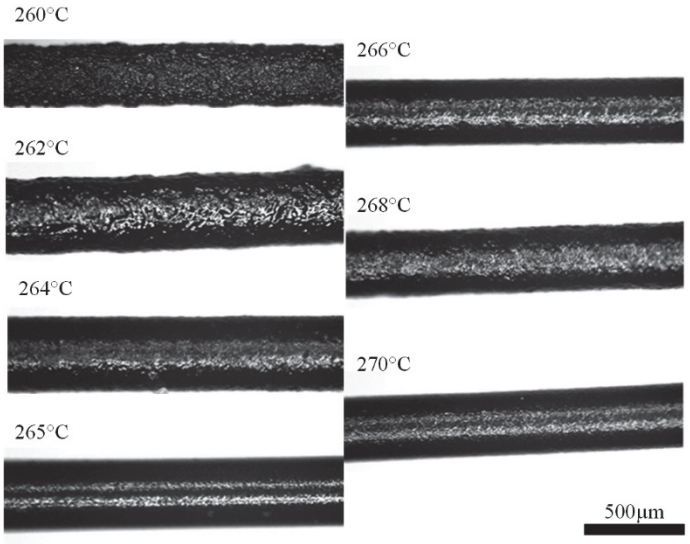

Figure 3.11 Microscopic views of extruded filament at different temperature settings.

During testing and analysis of the microscopy images, it was evident that at 260°C the extruder wasn't hot enough and as a result incomplete melting occurred. At 262°C the same problem occurred. When tested at 264°C there was still evidence of incomplete melting with occasional lumps and rough areas. At 266°C, consistent melting was observed and as a result an extra sample was taken at 265°C. For temperatures above the 266°C mark, even though the filament extruded well, it retained its heat for too long after exiting the nozzle resulting in deformation and string bridges when the nozzle was moved away. Since the extruder has the ability to maintain its temperature within ±1°C, a temperature of 266°C was selected for printing as this would give a range of 265-267°C at the nozzle.

The base layer that is laid down before the part is printed was determined to be optimal with a Z height of 0.4mm using a flow rate of 35 on the PWM setting for the extruder and having a feed rate of 100mm/minute. This gave an extrusion height of 0.55mm and 2mm width. The interface layer was then added using a Z height of 0.6mm maintaining a flow rate of 35 (PWM setting) and a feed rate of 1200mm/minute. This supplied sufficient material to bridge the gap between base layer filaments. As a result of the thinning of the extrusions over the base layer filaments and thickening over gaps, the extrusion height was found to be inconsistent. A second interface layer at a 0.7mm Z height was added and a consistent extrusion height was achieved.

The first layer of the part to be printed was laid down slower than subsequent layers in order to ensure sufficient contact was made between the first layer and interface layer preventing the part lifting during the printing process. The initial layer was deposited at a layer height (Z height) of 0.8mm, a flow rate of 35 (PWM setting) and the inner fill deposited at 1200mm/minute and outer perimeter at 1920mm/minute.

The first printed part was the default 20mm calibration box included in the ReplicatorG examples directory. It was successfully printed using a 0.1mm resolution using the parameters described above. The part was examined under an optical microscope and found that the layers were consistently 0.1mm as shown in Fig. 3.12.

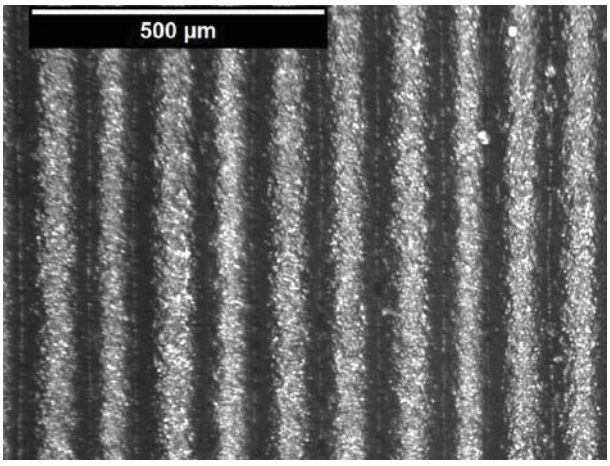

Figure 3.12 Microscopic image of initial test Box

Since the initial testing was completed by manually modifying the G-code to the above specifications, a test was done to investigate the results of the automatically coded test box. It was found that the two boxes were indistinguishable from one another. Fig. 3.13 shows a cut away of the hexagonal fill pattern used in the test box.

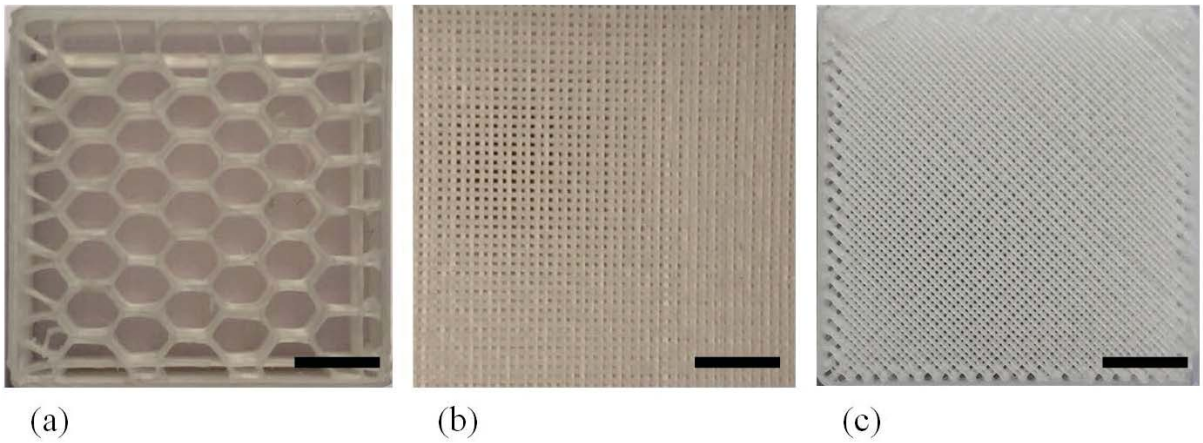

Figure 3.13 Cut-away of test box hexagonal (a), 0°/90° (b) and criss-cross fill pattern (c). *Scale bar* = 2mm

The box was re-printed using a ±45° raster fill angle and 0°/90° fill angle as shown in Fig. 3.13. Due to the nature of the different fill methods, the ±45° and 0°/90° create a denser fill when compared to the hexagonal fill. The 90% fill used for the printing of these samples however resulted in larger than expected inter-road gaps. Small samples were also created as shown in Fig. 3.14. These samples were used to test the accuracy and quality of parts manufactured after the retrofitment.

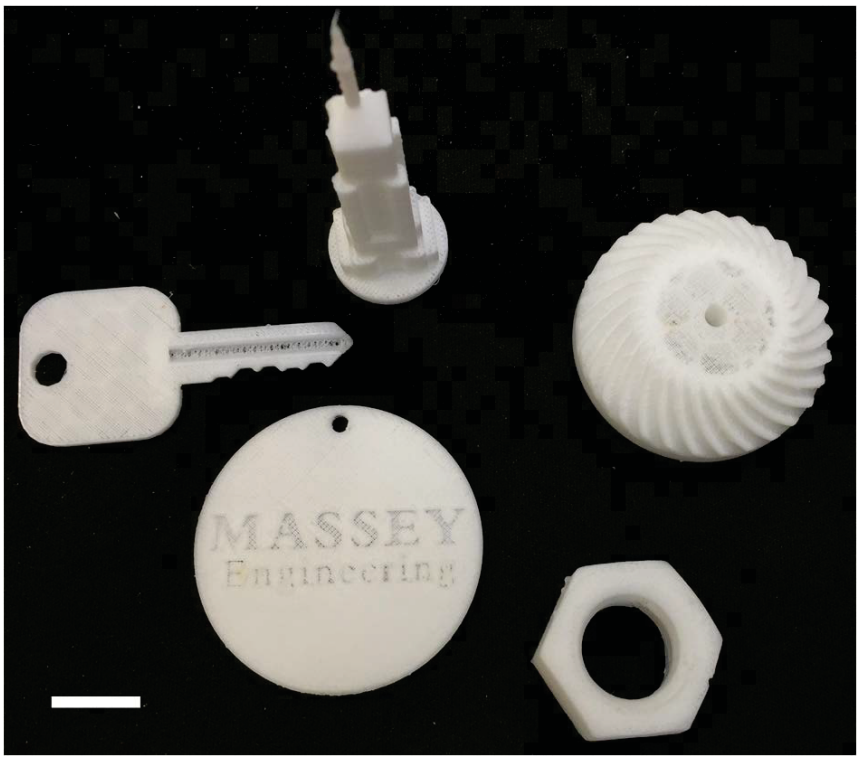

Figure 3.14 Miscellaneous small test parts printed on OpenVantage. *Scale bar* = 10mm

3.3. Mechanical strength testing

For the tensile testing of parts manufactured on the retrofit FDM Vantage X machine, UP Fila ABS+ material was used. ABS+ material provides heat stability, impact resistance and toughness along with allowing the printer to be tested using material not specifically designed for it. The dog-bone specimen design is done using SolidWorks 2015 based on the ASTM D638 type I standard. The design files are sliced using Slic3r to generate the toolpaths for the OpenVantage. Samples are printed with a 90% fill density and a ±45° raster orientation.

Tensile testing is performed using an Instron 5967 dual column testing system. An extension rate of 5mm/min was used for tensile testing with a 50-mm clip on strain gauge extensometer.

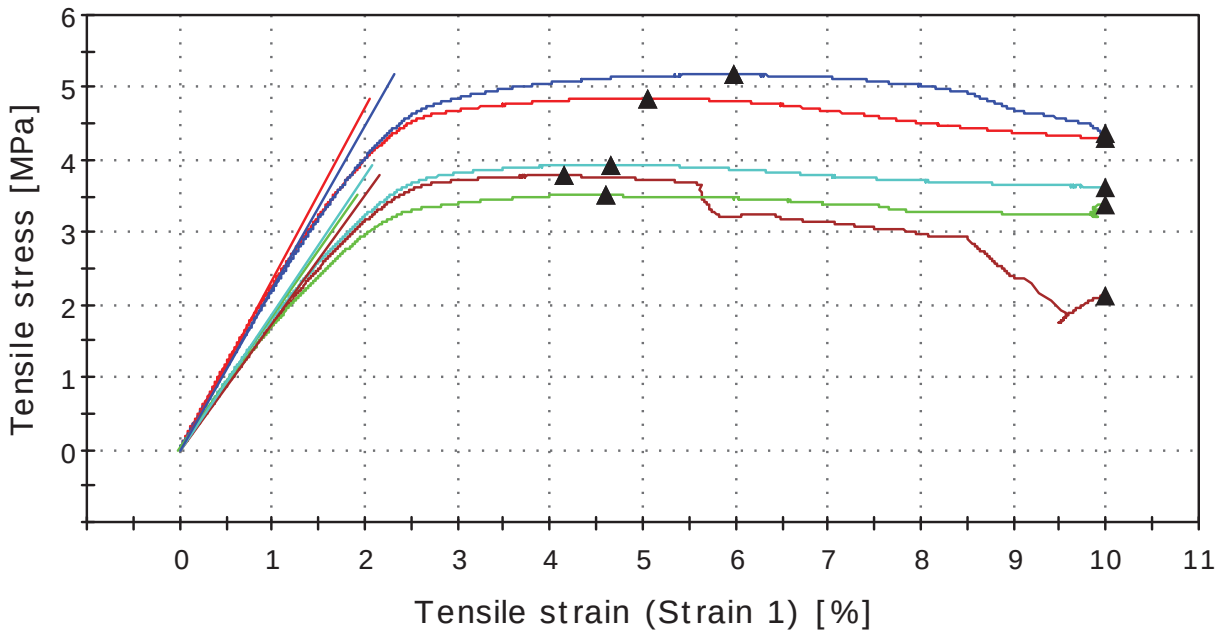

Figure 3.15 Stress strain diagram for samples printed on the OpenVantage

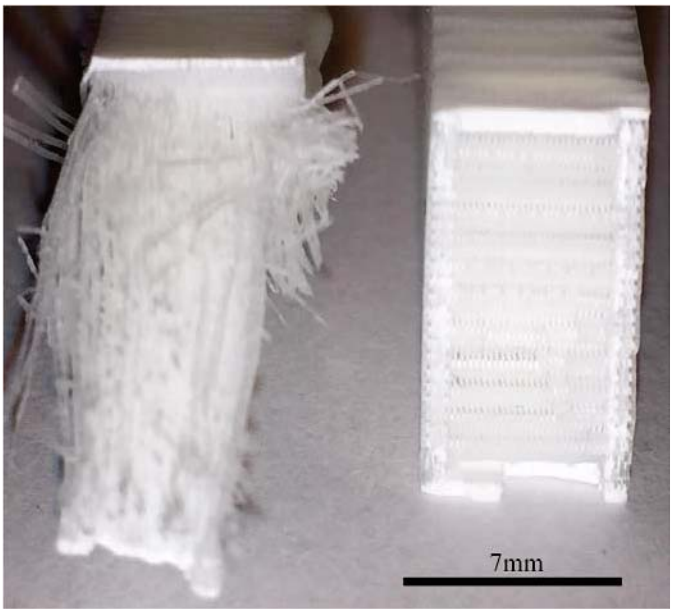

Figure 3.16 Magnified view of OpenVantage (*left*) and Up Box (*right*) printed samples

Five samples were printed on the OpenVantage printer and the average tensile strength values for these samples were calculated (Fig. 3.15). From the results, it is observed that the average strength of the parts is 4.25 MPa with a standard deviation of 0.721 MPa. These parts exhibit a low tensile strength and Young's Modulus when compared to printers such as the UP Box (tensile strength: 14.5 MPa and Young's modulus: 796 MPa) with samples printed using the same material and print settings. As Young's Modulus is a measure of material's stiffness, it can be used to indicate the flexibility of the parts printed on the OpenVantage. The elongation at yield experienced by dog-bones printed on the OpenVantage was more than expected showing that during failure, the individual roads continue to exhibit some elastic behaviour as the individual fibres systematically break. Parts printed on the Vantage X also don't exhibit brittle stepwise failure as in the case of the Up BOX. In Up box samples, the fracture surface shows a ±45° stepwise failure as the different fibre groups fracture together. In the case of the OpenVantage, fibres fail individually, resulting in a lower tensile strength and larger elongation before complete failure. Fig. 3.16 shows a magnified view of the fracture surface of one of the samples. From the image, it can be observed that the sample has a ±45° alternating layer orientation meaning that as the tensile load is applied, the fibres share the load making the bonding between layers weaker as the applied force increases. This is because the fibre orientation isn't parallel to the direction of the applied load resulting in weaker tensile strength. As the sample fails, the individual fibres shear and start to fray. Further investigation showed that the inter-layer and inter-road bonding wasn't sufficient in the tensile test sample as a smaller layer thickness and road width was created during the

printing process even though the printer was set to use a 90% fill density. As a result, the tensile test parts were weaker than expected as the individual fibres making up the internal fill weren't completely bonded.

3.7. Summary

The retrofitment of the Stratasys FDM Vantage X allows for the exploration of new research avenues. This work saw a Stratasys Vantage X successfully converted to the new OpenVantage 3D printer based on the MakerBot "Thing-O-Matic". The successful completion of this retrofitment relied on the modification of four main areas: Hardware, Electrical, Firmware and Software. As part of the first step in making the printer capable of accepting any feed stock, the drum feed system was replaced. In order to ensure complete operability of the new printer, the Front Panel Controller had to be replaced. The electrical redesign was done in order to align the printer's electrical system with New Zealand standards, which made the standalone transformer redundant, consequently reducing the footprint of the printer. A redesign of the main control board (motherboard) and extruder heads was also completed, which allowed for an increase in the resolution of the printer from the Stratasys standard 0.127mm in all three axes to a X-Y axis accuracy of 0.0045mm and a Z axis accuracy of 0.0032mm. With the OpenVantage based on the MakerBot "Thing-o-Matic" the base firmware used for this retrofitment is identical to that of the MakerBot system with some pieces of firmware used for alternate control purposes and some obsolete pieces of the firmware removed. Software control of the machine is done using ReplicatorG software in combination with Slic3r software for the G-code generation. Completion of the retrofitment was followed by a thorough calibration of the printer to ensure accurate operability.

After system calibration, various print and other tests were completed to validate results. For initial test prints, PC-ABS was used. Single fibres were extruded at 2°C increments between 260°C and 270°C. An extrusion temperature of 266°C was deemed optimal. A test box native to the ReplicatorG software was printed and evaluated under a microscope to ensure consistency between the fibre roads widths and inter-road bonding. Three additional test boxes were printed using different fill settings available in the Slic3r software. Externally boxes were found to be identical. Tensile test samples were printed and tested in accordance with the ASTM 638 Type I standard. An average tensile strength of 4.25 MPa with a S.D. of

0.721 was achieved. It was found that the relatively low tensile strength was because of insufficient bonding between adjacent roads and layers which reduced the ability of the part to effectively support a higher load. The part being made up of individual fibres rather than a diffused fibre network resulted from the layer thickness being set to 0.1mm. Taking into account the age of the core system with the Stratasys Vantage X being released in early 2006, it was expected that the tensile strength of parts produce on it would not be comparable to modern printers.

Improvement and research on the printer will continue. The successful retrofitment of this machine achieved a higher print resolution. However, the use of a higher resolution does reduce the parts strength, and conversely increase the part strength as the resolution is increased. This retrofitment also opened the ability to use almost any feed stock and gave full control of the print variable normally not available to the user. Based on these results, the retrofitment of this printer was successful.

4. Mechanical Properties of Temporally Spaced FDM Printed Samples

4.1. Introduction

There are currently various methods, standards and analysis tools used to study the mechanical properties of FDM parts. Investigations into the effect of processing conditions on material flow, inter-filament bonding, bond formation and inter-layer cooling has been completed. Determination of the optimal process parameters such as raster angle, air gap and layer height has also been done [19, 21, 31, 41, 108, 109]. However, research investigating the effect of temporal spacing on properties of printed parts, i.e. parts printed with the same parameters on the same machine at different times, has not yet been conducted as per best of our knowledge.

In order to allow better characterisation of the mechanical properties of printed parts under identical conditions at different times, investigation into the tensile strength along with a thorough examination of the build properties is required. Determination of the differences in the strain experienced by each sample group along with the supported tensile load is important. Evaluating the Young's moduli values of each group will also give a better understanding of the FDM process and its effects on printed parts. Supplementing this with scanning electron microscopy (SEM) analysis of the fracture, topographical and bonded contact surfaces allow a more holistic understanding of the potential inconsistency of parts printed using identical machines and material.

This chapter is dedicated to mechanical properties of temporally spaced samples printed under same condition on the same model of an FDM printer. Topological and fracture analysis with scanning electron microscope (SEM) are described in the chapter 5.

4.2. Hypothesis

With the identification of a gap in current research, further investigation into the chronological printing effect on tensile test samples was required. Traditionally, four raster angles are used during the FDM printing process. These are axial (0°), transverse (90°), crisscross (45°), and cross (0°/90°). For the purposes of this study, only axial and transverse raster orientations were considered. The use of these two raster orientations will allow the examination of the inter-layer and inter-road bonding of samples. These two bonding mechanisms are part of the fundamental factors that affect the strength of FDM parts. 0° and 90° raster orientations test samples rely on their fibres alone (axial) or the bonding between roads and layers (transverse) respectively for their tensile strength. From research conducted by [22, 24, 43] and others, it was expected that the axial print orientation will be superior to its transverse counterpart. In the case of the axially printed parts, the fibres support the tensile load. For parts printed using the same print conditions e.g. 90° old and 90° new, a difference was expected between the tensile test results. Newer parts were predicted to exhibit superior strength to the old due to possible degradation of the older samples. However, the differences in machine age and relative wear and tear from use had to be considered. With the original batch of sample produced a few months after the release of the Stratasys Fortus 450mc and the new batch produced almost two years after its release, the potential for machine age and degradation affecting samples must be considered. **Therefore, the hypothesis for the conducted research was that the age of both the machine and the part would play a combined role in its mechanical properties. Even though the older parts would potentially suffer some degradation over time, it was predicted that these samples would have superior quality as the printer would be relatively new at the time of print. As the printer ages, its ability to reproduce samples of identical quality under the same printing conditions and print settings would diminish. The axial samples were foreseen to exhibit little difference as they rely predominantly on their fibres for strength. A substantial difference was expected between the transversely printed samples due to degradation of the printer, with the quality of the inter-layer and inter-road bonding being negatively affected.**

Table 4.1 Printer control variable setting for both the old and new sample groups.

Sample Group	Old Samples	New Samples
Raster orientations	0° and 90°	0° and 90°
Air Gap	-0.01mm	-0.01mm
Material	ASA	ASA
Colour	Black	Black
Chamber Temp	90°C	90°C
Extrusion Temperature	380°C	380°C
Fill %	100%	100%

4.3. Methodology

4.3.1. Sample Preparation

For this study, parts were manufactured using the Stratasys Fortus 450mc 3D printer. These machines represent some of the newest technology currently available on the market by one of the leaders in the 3D printing field. Commercial FDM parts are commonly printed using materials such as ABSplus or ABS-M30^{TM}. The parts printed for the purposes of this research were manufactured using Acrylonitrile Styrene Acrylate (ASA). The tensile strength of ASA is 33 MPa which is very close to 32 MPa of ABS-M30 However, ASA boasts superior UV-resistance along with the best aesthetics of any FDM material [110, 111]. Due to the nature of the experiment, ASA would provide superior UV protection to ABS materials meaning a reduction in potential UV damage and sample degradation. Three injection moulded samples were created using ASA along with the FDM samples. These would act as reference for bulk material part performance manufactured from ASA and compared to the results obtained from parts manufactured through the FDM process. The initial “old” batch was manufactured in January 2015, with the “new” batch manufactured in July 2016 using the same material and printer type under identical print settings as per Table 1. With the variety of available tensile standards, the ASTM 638 type 1 standard was chosen due to its frequent use in FDM research [25, 45]. Thirty-six printed samples made up four sample groups with nine samples in each. Letters represent each sample group for ease of reference. Designation of the old samples with letters A and C represent samples with raster orientations 90° and 0° respectively. Similarly, new samples groups B and D represent samples with the respective 90° and 0° raster’s. Group E represents the injection moulded sample group. The use of a

slightly negative air gap, -0.01mm, ensured stronger bonds between sample roads and layers without sacrificing surface finish or accuracy. A layer thickness of 0.254mm along with a 100% fill would reduce the number of voids induced by the printing process. Reducing the number of voids would be vital as the study of the micro level properties of each lamina are related to the bond quality between filaments, the filament properties and the void density [108]. The use of the two-raster orientations, 90° and 0°, allows the evaluation of samples for their tensile strength based purely on either the inter-layer bond strength or fibre strength. Figure 4.1 shows the sample placement with represented raster orientation as positioned and printed on the printbed.

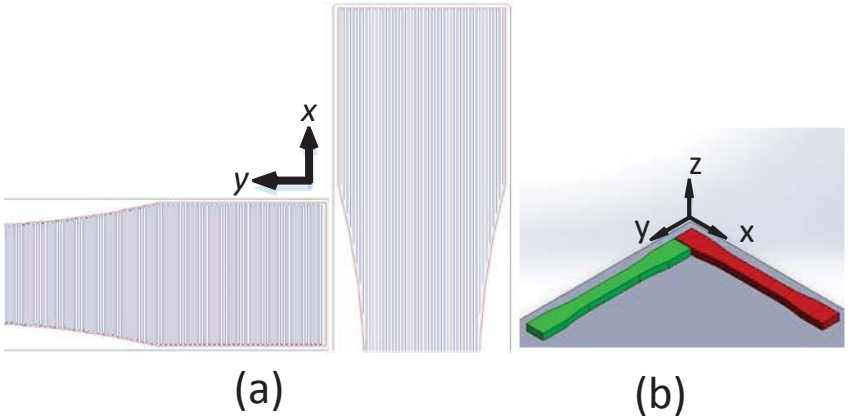

Figure 4.1 FDM samples; (a) 90° and 0° raster orientations and (b) sample position relative to printbed.

Computer aided design (CAD) software, SolidWorks, allowed for the accurate design and file creation of tensile parts in accordance with the ASTM D638 standard. Completed models are saved in the .STL file format. This allows Stratasys' "Insight" software to generate the tool path based on the desired settings. Upon completion of the printing process, samples are removed from the heated chamber and allowed to cool. Placing the completed part in a liquid bath removes the soluble support structure used during the printing process. The support takes up to eight hours to dissolve, after which parts are removed and allowed to dry. A major benefit of the soluble support is its ability to help retain the structural integrity of printed samples. As there is no need for support to be broken away from the part, it is not subjected to unnecessary external forces that have the potential to alter its mechanical properties.

4.3.2. Sample Tensile Testing Procedure

An Instron 5967 tensile testing machine fitted with a 30KN loadsel, having a force accuracy of 0.001N, allows for the completion of the tensile testing. A 50mm extensometer attached

longitudinally allows strain to be calculated while the part is tested as depicted in Fig 4.2b. The crosshead speed is set to 5mm/min in accordance with the research standard used. During the sample setup, precautions taken ensure consistent and accurate results from the samples. Samples are marked using masking tape to accurately position them in the grippers with a distance of 115mm between each gripper in accordance with the ASTM 638 standard used. Samples are positioned to the back plate in each gripper as per Fig 4.2b. This ensures each sample is kept vertically reducing the chance of one side bearing most of the load due to an incorrect loading angle. The extensometer is then positioned in the middle of the sample's gauge length and the test started. The test is completed once complete fracture occurs in a sample. Fig. 4.2a depicts the test setup.

Figure 4.2 (a) Instron 5967 used for tensile testing; (b) experimental setup for tensile testing with extensometer position; (c) 50mm Instron GL50mm extensometer used

Table 4.2 Sample group with the corresponding labelling method used to for ease of reference

Sample Groups	Old 90°	New 90°	Old 0°	New 0°	Injection Moulded
Corresponding labels	A	B	C	D	E

4.3.3. Sample Storage

Old test samples (groups A and C) were stored in a sealed container. Early on moisture was noticed inside the container and Silica gel crystals (LabServ BSPSL519.5) were added to maintain a dry environment. Regular evaluation of the crystals ensured their replacement as required. The removal of this unwanted moisture helped to ensure part degradation would not occur from a high humidity environment. The storage of samples in an air-conditioned room kept at 21°C would eliminate any unwanted thermal cycles. No matter how small the thermal cycle's samples are subjected to, they could potentially influence the mechanical properties of the parts. Parts were not exposed to any direct sunlight and UV exposure from Fluorescent light was kept to a minimum.

4.3.4. Scanning Electron Microscope (SEM) Imaging Procedure

After examination of the fracture surfaces under a microscope, further investigation into the failure mechanisms experienced by the parts were required. The use of Scanning Electron Microscopy (SEM) allowed for this examination on the micron and sub-micron level. Upon visual examination of the various fracture surfaces in each sample group, representative samples from both sample groups A and B were selected for scanning electron microscopy. Topographical and fracture surface imaging was completed on the sample groups. Based on the tensile test results, sample groups C and D were not investigated, as their tensile properties were almost identical. The large discrepancy between groups A and B warranted further investigation as to the cause. The selected samples were cut 7mm from the fracture surface. As it is vital to not hinder or damage the fracture surface or contaminate it with dust and debris from the preparation process, the samples were handled with gloves and a set of tweezers. A fine-toothed hacksaw was used in order to slowly cut through the sample. Eight hundred grit wet and dry sand paper was used to slowly smooth and level the cut surface.

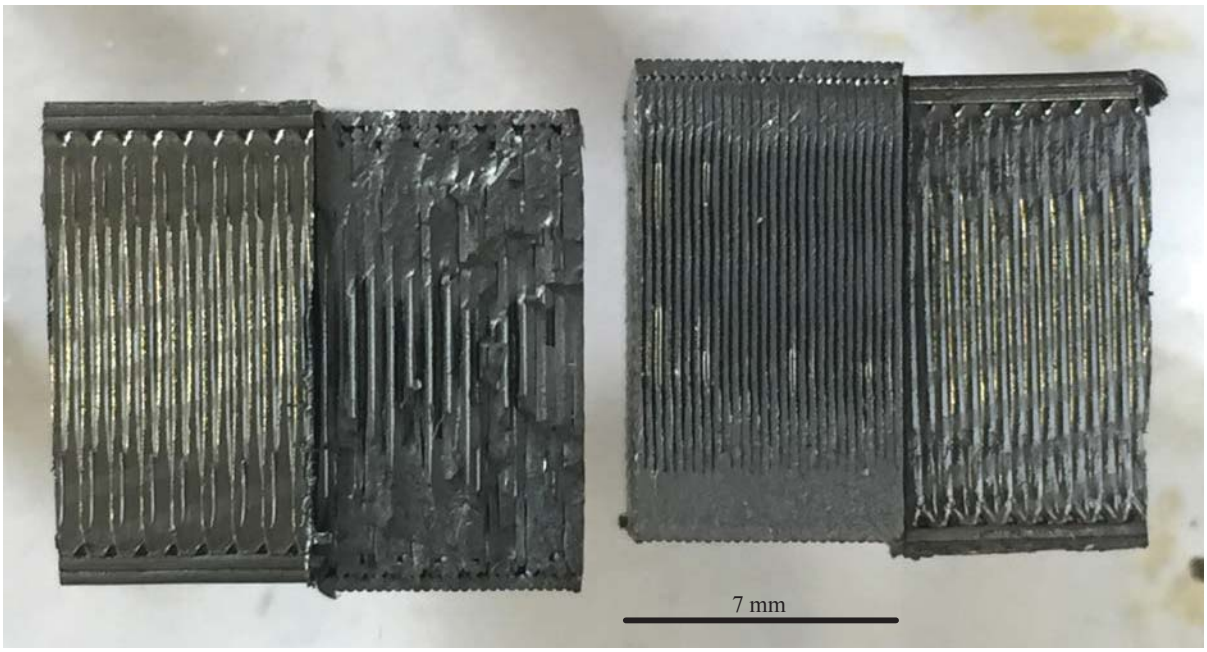

Figure 4.3 Samples prepared for SEM analysis for the old (left) and the new (right) samples as positioned on the carbon tape stubs.

The sample were placed on a SEM stub using double-sided carbon tape as per Fig.4.3. SEM machines require parts to be in a vacuum, because of this, carbon tape is required as it will not collapse or deform in a vacuum and will enhance conductivity [112]. As these samples are made from ASA material, they are non-conductive. This means for the Topographical imaging, samples had to be coated using a conductive paint that is silver-based. Specimens placed into the SEM machine, a FEI Quanta 200 FEI (SEM), have coordinates assigned to them based on their position on the test bed.

The fracture surfaces of each sample are systematically reviewed using various magnifications. The fracture surface is broken up into six zones and each zone further examined under higher magnification as per Fig 4.4.

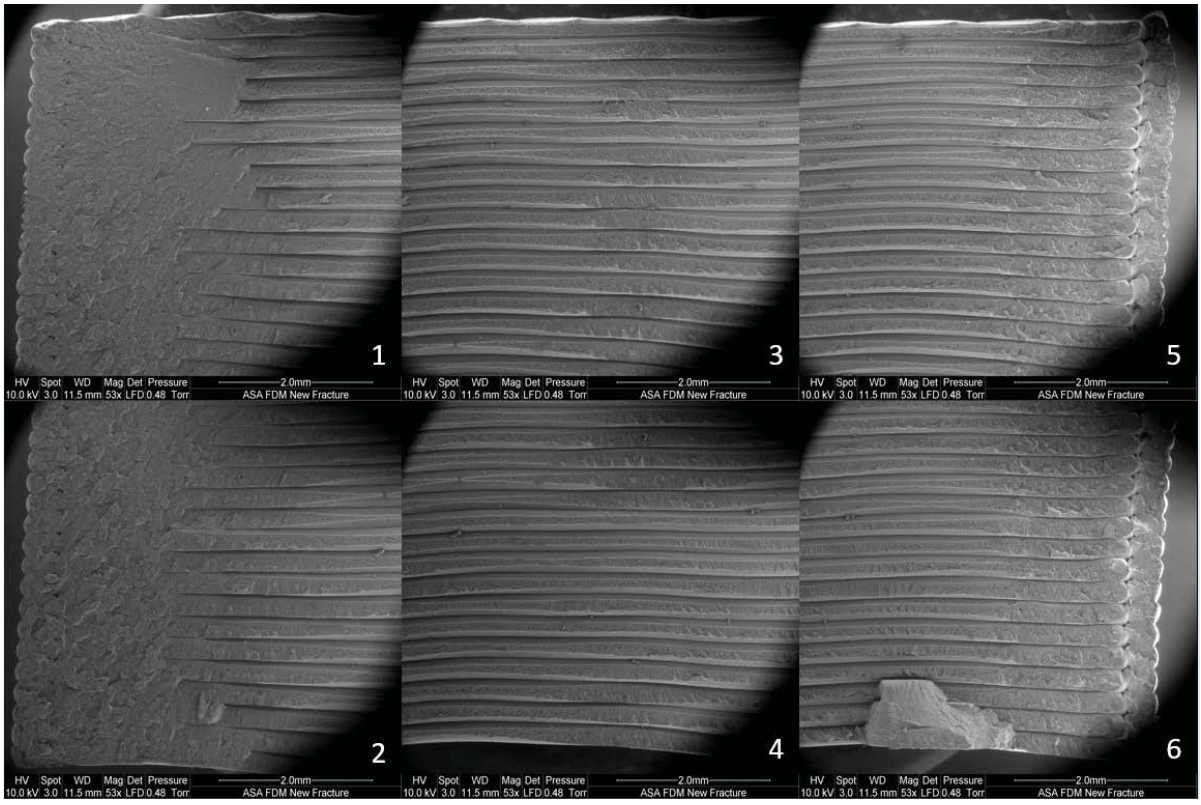

Figure 4.4 SEM imaging and sextant break up of a sample fracture surface

4.4. Tensile Test Results

In accordance with the ASTM D638 standard, completed tensile testing delivered results on the tensile strength, Young's Modulus, and tensile strain at yield along the longitudinal direction for each specimen. Table 4.3 shows the obtained results.

Table 4.3 Obtained tensile test results for the samples groups A, B, C, and D

No. of Samples Considered	Sample Group	Tensile strength (MPa)	Tensile strength (MPa) SD	Young's Modulus (MPa)	Young's Modulus (MPa) SD	Tensile Strain (mm/mm)	Tensile Strain (mm/mm) SD
9	90°, Old (A)	31	1.057	2050	136	0.028	0.005
9	90°, New (B)	22.8	1.989	2010	125	0.016	0.002
9	0°, Old (C)	38.1	0.251	2180	69	0.078	0.023
9	0°, New (D)	36.6	0.529	2080	44.7	0.047	0.016
3	Injection Moulded (E)	42.4	0.881	2150	157	0.068	0.024

The failure mode experienced by all FDM samples resulted from material separation along a plane normal to the applied tensile load. Longitudinal samples experienced fracture primarily in the transverse direction, with individual fibres breaking under tension along their axial

direction. Failure of the bulk material samples was due to fracture through the cross section of the sample.

Group A samples experience some fibre pull-out along with intermittent delamination at the edge along the longitudinal axes as per Fig 4.5a. This resulted in a highly irregular fracture surface. Group B samples had a more consistent delamination along a single plane perpendicular to the applied load. Roads separated from one another and regions where more complete diffusion occurred, failed along the same plane resulting in a relatively flat fracture surface (Fig. 4.5b). Comparing the fracture surfaces of groups C and D, delamination between the interior fill of the samples and the boundary roads occurred. This indicates insufficient boding between the external boundary layer and the subsequent internal layers. Group C samples exhibit a higher overall level of diffusion between the parallel roads when compared to group D with the individual fibres of group D more visible to the naked eye. Group E shows the homogeneous fracture surface with failure occurring perpendicular to the applied load as crack propagated through the sample.

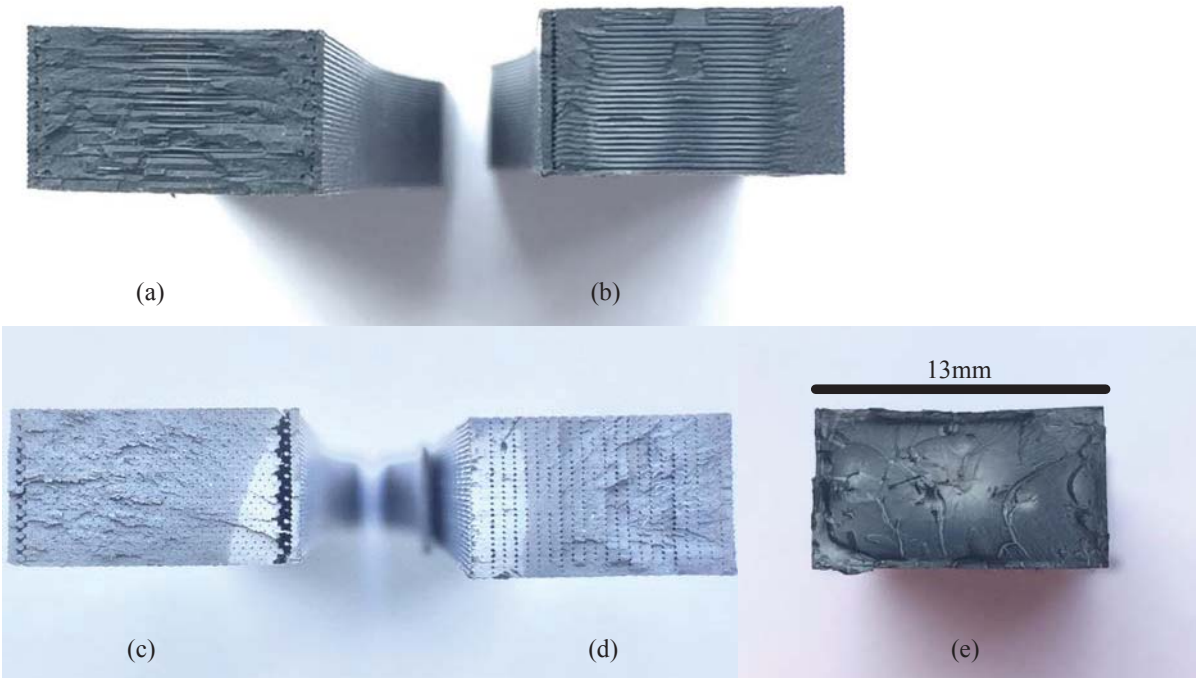

Figure 4.5 Fracture surface images of sample groups A, B, C, D, and E as presented by their respective a, b, c, d and, e group labels.

4.4.1. Elastic Modulus Results

The elastic modulus of specimens was calculated to examine part elasticity and how they compare to one another based on manufacture date (age of printer used) and raster angle. A comparison of the old and new sample Young's moduli (E) for the 0° raster orientation indicate a slight difference between the two sample group values. Fig.4.6 shows the distribution of the E values for the two sample groups along with the respective group means.

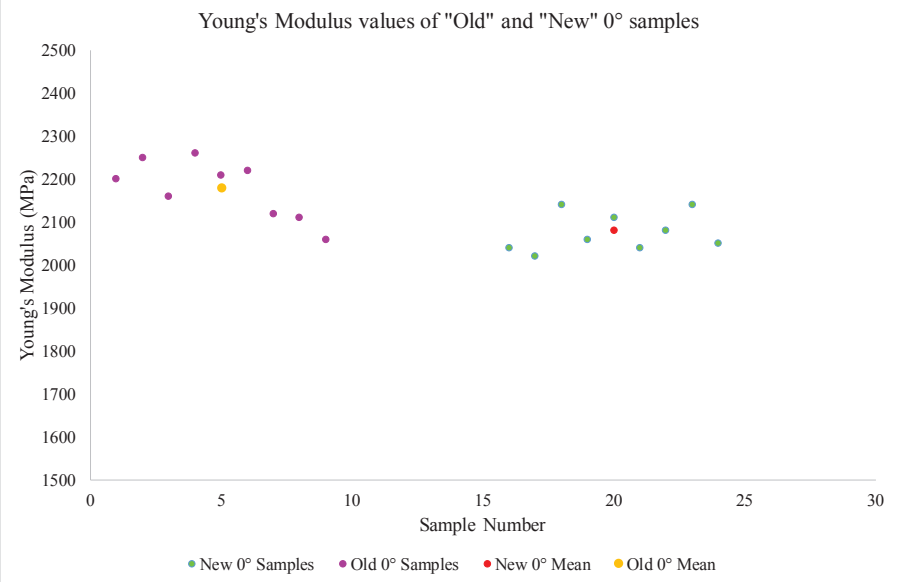

(a)

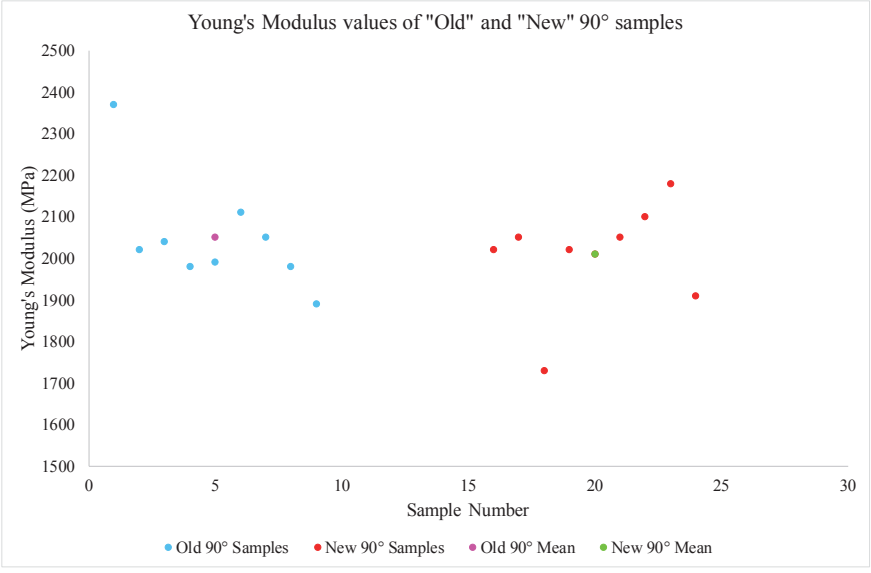

(b)

Figure 4.6 Scatter plot of the "Old" and "New" Young's Modulus values for sample groups C and D on top. Similarly, groups A and B are represented at the bottom.

Examination of the plot shows a reasonable range of E values for the samples in groups C and D. A two-tail t-test was completed to determine whether there was any significance between the two sample groups. The hypothesis for the t test assumed that no difference exists between the two sample groups. The results indicated a significant difference between the two sample groups with a P value (0.0023) less than 0.05. Research conducted by Bellini et al. [19] included testing the Young's modulus of the filament used and an extruded road of the filament. They found that the values of the Young's modulus and tensile strength is similar. The maximum strain obtained for the road test was almost a third of the obtained value for the filament. This led them to conclude that the extrusion process does not have a considerable influence on the strength and modulus of the material. The only noticeable effect is on the strain. They concluded that this can be explained by the viscoelastic behaviour of the ABS. This reduces the materials elongation characteristics. During the extrusion of a thermopolymer through a nozzle, the polymer is submitted to an orientation of the molecule chains [113].

As per [19], the extrusion process has limited or no influence on the Young's moduli of extruded parts. It is therefore believed that the observed difference in Young's Modulus values for samples groups C and D is potentially due to degradation of the material coupled with a difference in the level of diffusion within each sample group and the raster orientation. Group C also exhibits the most inconsistent E values.

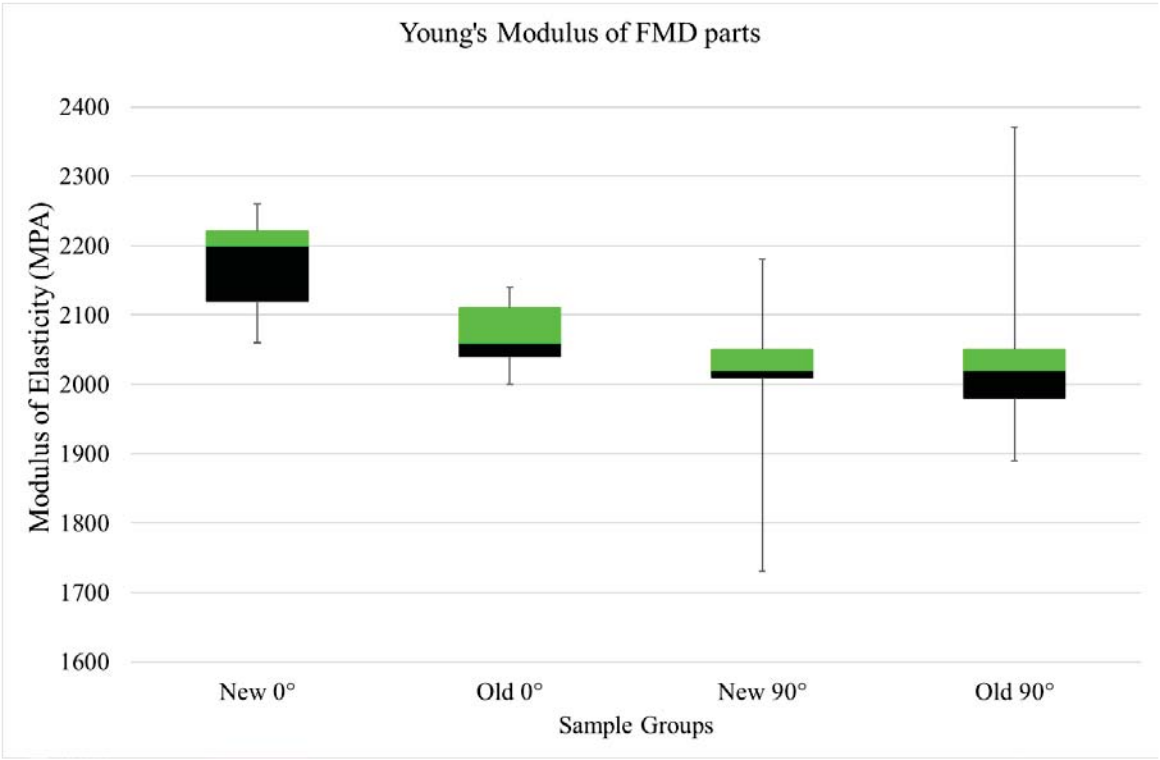

Figure 4.7 Box plot representation of the four sample groups Young's Moduli.

Sample groups A and B, the 90° raster samples, resulted in similar Young's Moduli. The small variation between the E of sample groups indicate no significant difference between samples regardless of the date they were printed. This was confirmed by the P value (0.526) of the conducted t test being higher than 0.05. Fig. 4.7 depicts a box plot of all four sample groups. This depiction of the Young's moduli results show the overlap between the new and old 90° sample groups with a noticeable difference between groups C and D. It should be noted, considering the error in the samples, the E values are not that different to indicate a large difference as they all overlap. These results indicate the unchanged material properties of the ASA material regardless of time between print and test date. It confirms that the fibres all undergo the same thermal changes during the deposition process resulting in a bonded material (the sample) that has a similar Young's modulus.

A comparison of the average Young's moduli of groups A and C, both old sample groups, indicate a statistical difference between their respective E values with a P value of 0.025. Although, the pure numerical difference between the samples is only 130MPa. This could occur as a result of different feed stocks used for printing having a slight variation between them or as a result of the orthotropic nature of the FDM part. The ASTM 638 standard is a standard designed for examination and comparison of homogeneous materials (bulk

materials) such as injection moulded ABS. The mechanical properties of FDM parts are largely influenced by the printing process and quality of the part bonds. This could potentially influence the measured Young's modulus of parts enough to explain the variations observed in the samples even though they are manufactured using identical parameters apart from their raster angles. Comparing groups B and D, no significant difference was found between their E values with a P value of 0.161. It should be noted that in both orientations, the Young's moduli were higher for the older samples compared to their respective new sample group counterparts. Visual examination of the fracture surfaces (Fig.4.5) indicate a higher level of diffusion between the fibres in the old samples compared to the new. This has the potential to influence the measured Young's modulus of the samples. The slight error in measurement is expectedly caused due to the nature of the testing mechanism. Standards such as the ASTM 638 are designed to examine bulk materials. It is theorised that the raster orientation influences the measured Young's Modulus values. Samples with a 0° raster orientation exhibit properties closer to those of bulk material. The inter-road bonding of 90° sample affect the measured Young's modulus. Similarly, comparisons of the Young's modulus values between samples groups A and B (90° sample groups) and groups C and D (0° sample groups) show higher results in favour of the old, more thoroughly diffused samples. Another indication of the influence the orthotropic nature of FDM samples have on the measured Young's modulus values is clear when considering the Standard Deviation (S.D.). The S.D. for both 90° sample groups is significantly higher than their 0° counterparts showing the influence of raster orientation on the reliable measurement of sample E values. In both cases the S.D. for the 0° samples are almost half of the 90° groups. Apart from the diffusion level in the sample groups, raster orientation also greatly influences the measurement. The lower S.D. values in the 0° samples occur as a result of the fibres parallel alignment with the applied load. With the load predominantly supported by the fibres themselves along with the fibres diffused together, the measured results would more closely resemble those of injection moulded parts. The completion of the filament vs. road tensile tests of ABS samples by Bellini et al. [19], showed that the Young's modulus of the two samples stayed relatively consistent with 34.309 MPa and 33.609 MPa for the Filament and Roads respectively. Tensile test results of orthotropic FDM samples with different raster orientation showed consistent variations in the samples elastic moduli. Bellini et al. reported a 16% difference in the Young's modulus values between their 0° and 90° samples. Espin et al. [67] reported a 6% variation in E values for the same orientations. In both cases the 0°

raster orientation had the highest Young's modulus value. For this research, sample groups A and C displayed a 6 % difference and groups B and D a 3% difference in their respective Young's moduli.

Comparisons of the Young's moduli from the FDM sample groups to that of the injection moulded parts, it was found that the modulus values for groups C and E were statistically similar. This means that due to the high level of diffusion and other factors discussed, the old 0° samples exhibit almost identical material properties during tensile loading with samples responding similarly to the bulk material in every way. The new 0° samples exhibit a lower elastic modulus than the bulk material along with both 90° sample groups as a result of the lower levels of diffusion in the samples along with variations in the raster orientation. Based on the knowledge that raster orientation influences the measured Young's modulus values, along with this research findings with the level of diffusion also influencing the measured Young's modulus, it is concluded that elastic modulus can act as an indication of diffusion level when comparing FDM parts of the same raster angle. The modulus can also be used to indicate the level of diffusion between FDM samples and bulk material samples.

Before moving on to the stress and strain analysis, it is important to understand the following.

$$E = \frac{\sigma(\varepsilon)}{\varepsilon} = \frac{{}^{F}/_{A_0}}{{}^{\Delta L}/_{L_0}} = \frac{FL_0}{A_0 \Delta L} \tag{4.1}$$

Equation 4.1 shows the relationship between a sample's stress, strain and, Young's modulus assuming the part is perfectly elastic. According to Chanda et al. [114], the viscoelastic behaviour of plastics can be described when assuming a perfect elastic material. In this material, the stress is directly proportional to the strain. Equation 4.2 can be written for the uniaxial stress and strain relationship where the constant is the Young's Modulus.

$$\sigma = E \times \varepsilon \tag{4.2}$$

A perfectly viscous liquid can be described using equation 4.3 where the shear stress (τ) is directly proportional to strain rate (γ) and the constant represents the viscosity.

$$\tau = constant \times \gamma \tag{4.3}$$

Polymer materials exhibit stress-strain behaviour that falls somewhere between these two cases and therefore they are termed viscoelastic. In these materials, stress is a function of both strain and time described by equation 4.4 representing nonlinear viscoelastic behaviour.

$$\sigma = f(\varepsilon, t) \tag{4.4}$$

For simplicity during analysis, this equation is reduced to equation 4.5 which represents linear viscoelasticity.

$$\sigma = \varepsilon f(t) \tag{4.5}$$

This means that stress will be directly proportional to strain for a fixed value of time in a tensile test on these materials. Viscoelastic materials also exhibit time-dependant deformation or strain when subjected to a constant stress. When subject to a constant strain (relaxation) they exhibit time-dependant stress. Upon removal of the applied stress, these materials recover and can be considered a reversal of creep.

4.4.2. Strain Evaluation Results

A comparison of the strain (ε) values for sample groups C and D displayed a significant difference. This was confirmed using a student t test with a resultant p value of 0.004. With strain defined as $\varepsilon = {\Delta L}/{L_0}$ (where ΔL is change in length and L_0 is original length), the mean strain values of sample groups C and D showed that the old 0° samples exhibited a larger elongation under load compared to their new counterparts. Strain experienced by group C is also the closest to that of group E meaning that samples in this group exhibit not only the closest modulus values but also the closest strain. The large difference in strain between groups A and B with respect to group E is due to the effect that raster orientation, and its subsequent delamination under load, has on tensile samples.

Comparing the strain values for the 90° samples groups also indicated a difference in the strain values per the performed t test with resultant p value of 0.00001. Consistent with the finding for the 0° samples, the old 90° sample experienced the largest change in length during loading and therefore largest strain. It should be noted that, as in the case of the Young's modulus, the strain values were highest for the older, more thoroughly diffused samples. The higher diffusion level in these samples would exhibit a more homogeneous response compare to the lower diffusion counterparts. As the load is applied to a more homogenous sample, the

fused fibres work as one to support the load. This is explained by the equation $\sigma = E \times \varepsilon$. In homogeneous samples, the E values would be constant. However, due to the orthotropic nature of tensile samples in this research, there is slight variations in the E values meaning that the stress stain relationship between different samples and sample groups would be affected.

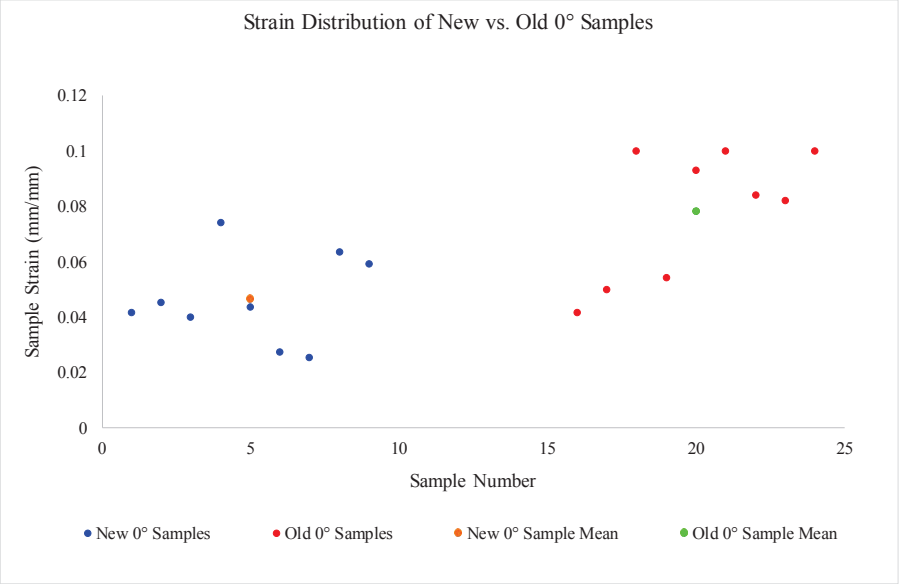

(a)

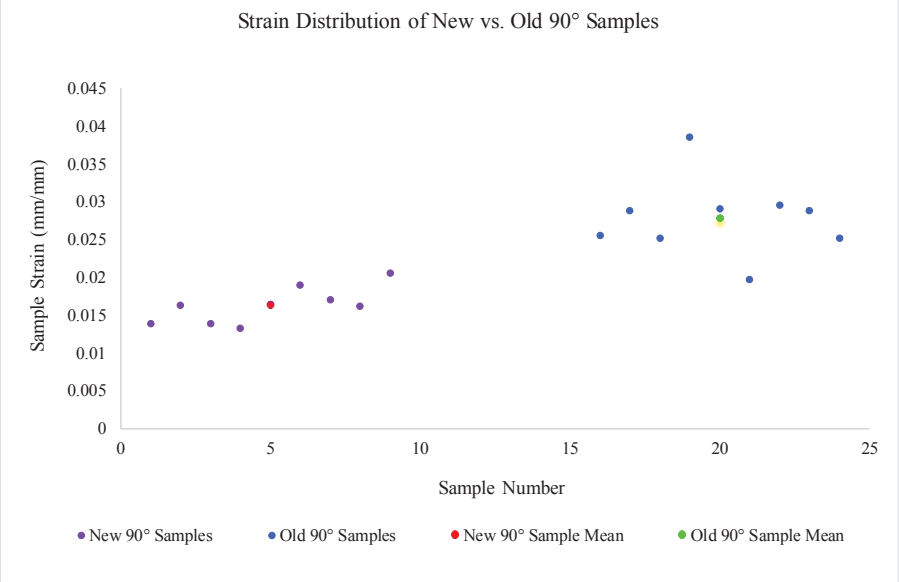

(b)

Figure 4.8 Scatterplot representation of the stress values for the Old and New 0° samples on top and Old and New 90° samples on the bottom.

The mean strain values of the 90° samples were lower than their 0° counterparts. However, this was expected. During testing, the fibre alignment for the 0° samples are parallel to the

direction of loading. This means that the load was supported predominantly by the longitudinal fibres. With the fibre orientation parallel to the load, the homogeneous fibres elongate more than their 90° counterparts. For the 90° samples, the load is applied perpendicular to the raster orientation meaning the load is supported primarily by the inter-layer and inter-road bonds. These bonds are weaker than the homogenous fibres and can therefore undergo less strain. They cannot support a load equivalent to the fibres themselves and will therefore fail before the fibres. These bonds are only partial and the fibres in their 90° orientation, have a higher resistance to strain.

In the 0° and 90° orientations, each of the individual fibres, although partially bonded together, can be examined as a single fibre for understanding the difference in the strain.

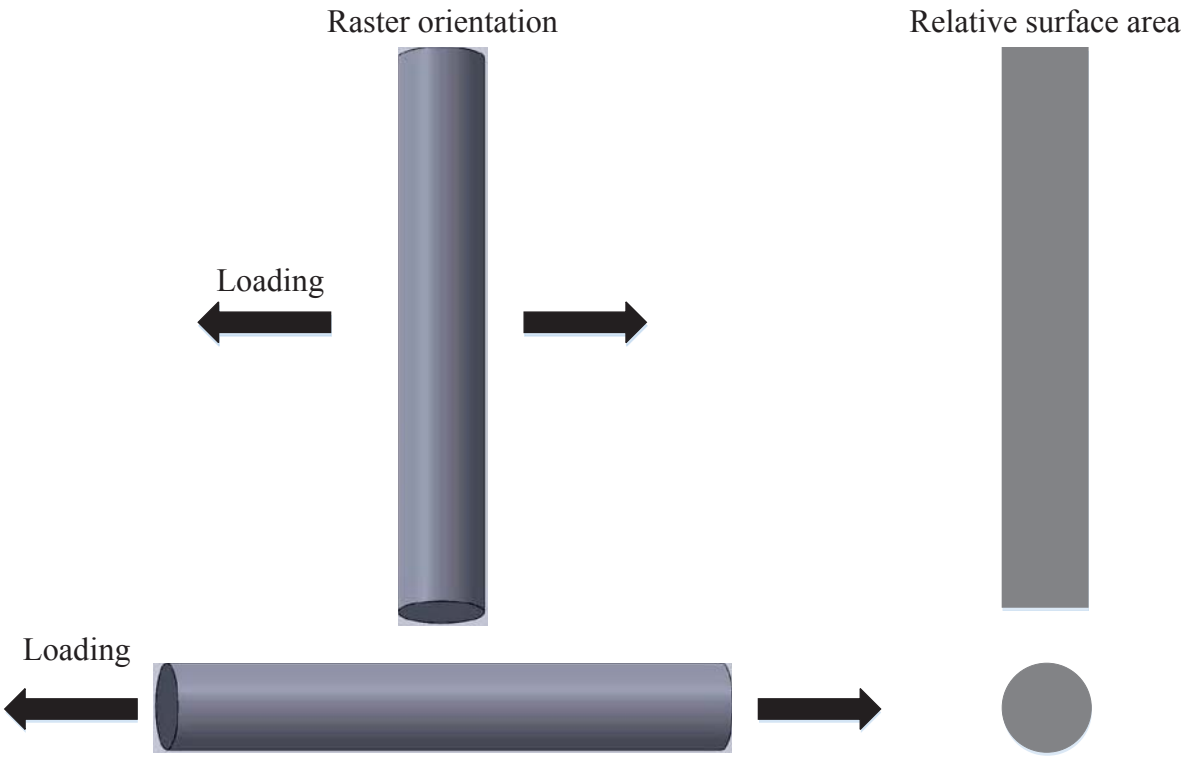

Figure 4.9 Individual fibre representation of the 0° and 90° raster orientation

Samples in the 90° orientation have the load applied perpendicular to the raster orientation. This results in a larger relative area supporting the applied load as depicted in Fig.4.9. This increase in area relative to the load results in a part with a higher resistance to strain. In order to aid understanding, an equivalent example would be a rectangular shaped piece of soft rubber. If the piece of rubber is aligned longitudinally to the applied load, its elongation

might be equal to 10mm. If that same piece of rubber is aligned 90° with the identical load applied, the elongation experienced would be significantly less (10 mm - x) depending on its dimensions. This is due to the relative area the load is pulling on. The same principle applies to the roads of a sample. This in conjunction with the weaker bonds explains why the 0° samples had a higher strain value compared to their 90° counterparts.

4.4.3. Tensile Strength Results

Examination of the average tensile strengths of the test groups supports data that raster orientation significantly affects the tensile strength of FDM parts [115]. Groups C and D representing the axially printed samples exhibited far greater tensile strength than samples printed with a 90° raster orientation (groups A and B). The new sample groups (B and D) displayed a 38% difference in their mean Ultimate Tensile Strength (UTS). Similarly, old sample groups (A and C) displayed a mean UTS difference of 17%. A surprisingly low difference as researchers such as Ahn et al. [30] reported a difference of 86% between their axially and transversely printed samples. These findings coincide with published research and further support the orthotropic nature of FDM parts. The properties at the interface of FDM parts are not the same as the material properties (perfect bonding does not occur). A UTS comparison of the "new" and "old" 0° samples showed very similar strengths with only a 1.5MPa mean UTS difference in favour of the old samples. For the 90° sample groups (B and D) a significant difference of 8.24 MPa exists between the UTS values, again in favour of the "old" samples. Samples printed 1.5 years prior, exhibit a 26% difference in strength even though they were printed using identical print parameters. Comparisons of groups A, B, C, and D with group E showed respective differences in strength of 27%, 46%, 10% and 13% with the old 0° samples having the closest tensile strength to that of the bulk material.

This notable difference in the tensile strength of the 90° raster groups require further investigation. With no post processing done on the sample sets and the identical print parameters used, a possible explanation of the collected data could be the level of diffusion in the parts. An increase in diffusion over time could potentially explain the increase in strength along with an increase in the level of diffusion during the initial print process could also explain the noted difference. A higher level of diffusion will result in parts that are more homogeneous having properties tending towards those of bulk materials. When a more thoroughly diffused part is subject to a tensile load, it comes closer to resembling the properties of a single piece of material when supporting an applied load. In the case of FDM

samples however, even though diffusion occurs between the samples, the deposited roads experience different levels of diffusion. This is clearly visible as depicted in Fig. 4.5. Visual examination between samples A and B as well as C and D show clear differences in the level of diffusion that occurred during the printing process. In both instances, Samples A and C display a higher level of diffusion. The differences in the tensile strength between the respective sample groups with the same raster orientation helps to confirm the effect that the diffusion level has on the parts tensile values.

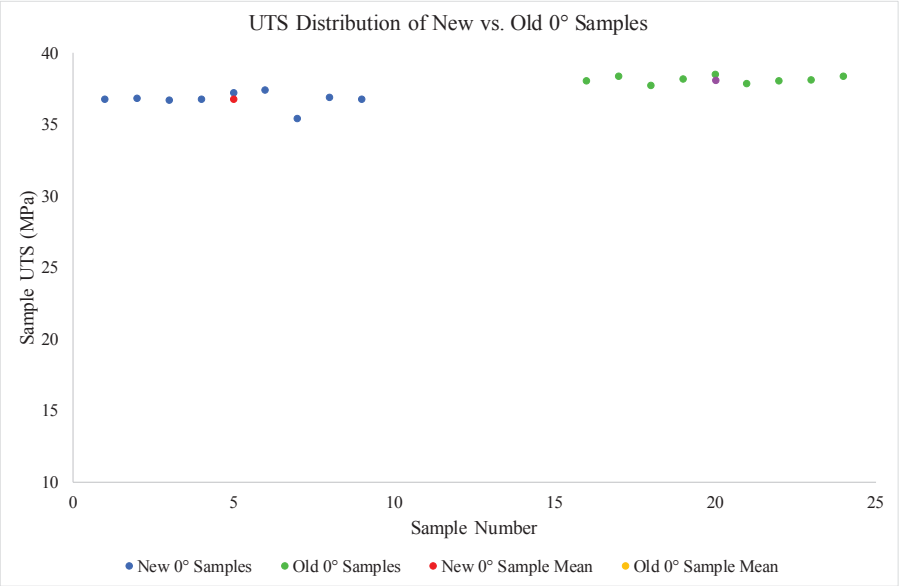

(a)

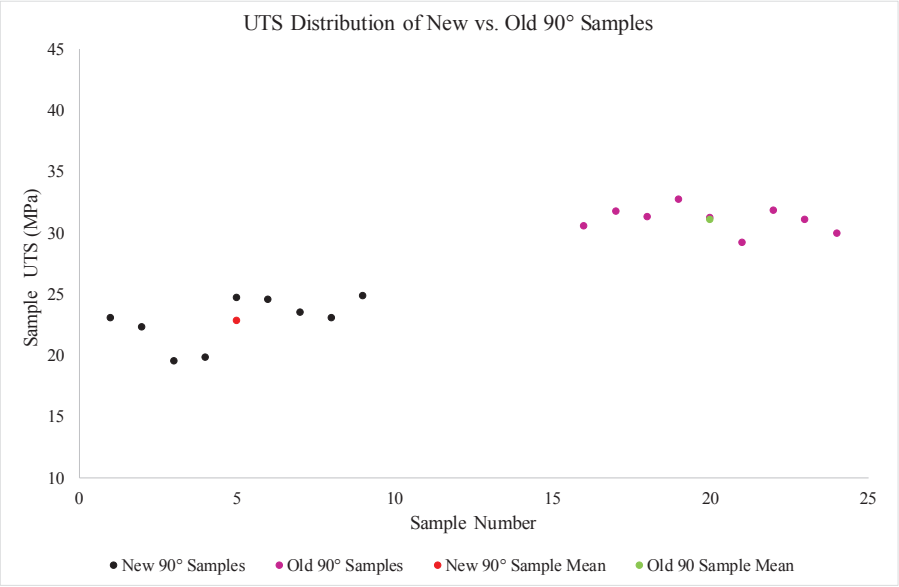

(b)

Figure 4.10 Ultimate Tensile Strength distribution of (a) New and Old 0° samples and (b) New and Old 90° samples

The scatter plots in Fig. 4.10 show the different tensile strengths achieved by the samples in each subgroup. The new 0° sample group had one outlier that exhibited a larger variation from the mean compared to other samples. The observed Standard Deviation (S.D.) of both the 0° sample group was quite low with sample group C showing the lowest variation. Removing the outlier from sample group D changed its S.D. value from 0.557 MPa to 0.26 MPa which is almost identical to the 0.25 MPa of sample group C. Removal of the outlier had a negligible effect on the mean tensile strength value of group D (0.167 MPa). Statistical analysis however showed a significant difference between groups C and D. Fig.4.11 shows a box plot of the sample groups' tensile strength. It is observed that there is no overlap by any of the sample groups even though the difference in tensile strength of groups C and D is reasonably low. This difference in strength is caused by the diffusion level between the axially aligned fibres being higher in sample group C.

A comparison of the S.D. values of sample groups A and B showed a much larger variation. This is likely due to the different levels of diffusion in the parts. As depicted by Fig. 4.10, two samples had tensile strengths below 20MPa with the average value for the group being 22.8 MPa. Mitigating the effects of these two samples, the average strength for group B would be 23.7 MPa with a S.D. more in line with group A of 0.995 MPa. Overall, a larger variation was observed in the 90° sample groups. This is due to the parts reliance on inter-layer and inter-road bonding for strength rather than the fibre roads as in the case of the 0° samples. As these parts are only as strong as the weakest bond between two adjacent layers, larger variations in the achieved tensile strengths are expected. A single layer having insufficient bonding could greatly influence the achieved tensile values. For 0° samples, insufficient bonding won't influence the tensile strength as much because the roads support the majority of the load. The large variation in strength between groups A and B shows a significant difference in the bond quality and level of diffusions of the parts. As it is also known that a larger bonded surface area would greatly increase the strength of a part, it is expected that Scanning Electron Microscopy imaging will show larger bonded areas for group A. A similar result is expected for group C when compared to D.

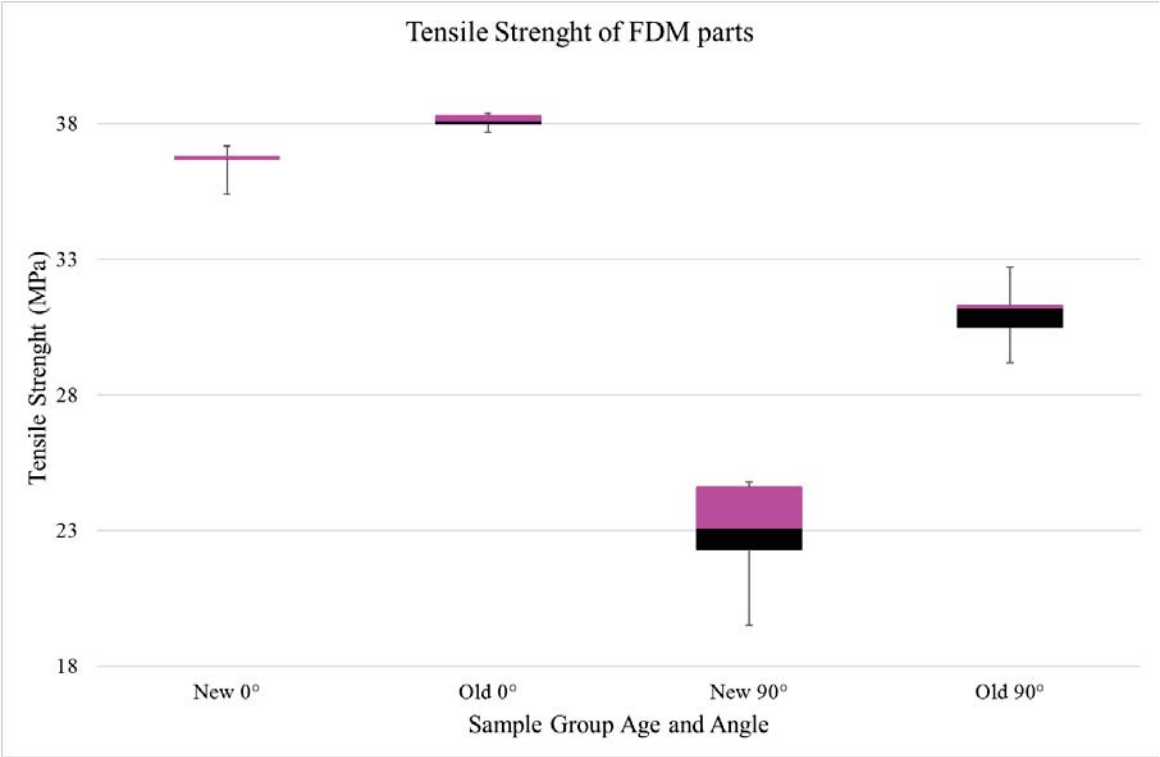

Figure 4.11 Box plot representation of the four sample group's Tensile strength

Examination of the stress strain behaviour of samples that are loaded at a constant rate allows for a comparative analysis of various samples. During the testing phase of the samples, each sample undergoes certain phases. In the initial phase between 0-1 on Fig. 4.11 right, the material behaves as an elastic solid. This means that any deformation is recoverable. The deformation is normally small and occurs due to the stretching or bending of the interatomic bonds between atoms of the polymer molecules. No permanent displacement occurs between adjacent molecules. The second phase between 1 and 2 (Fig.4.12) is associated with a portion of the kinked or coiled molecular chain straightening out. This deformation is ultimately recoverable over time and no change in inter-molecular arrangement occurs. The elastic limit of a material is the greatest extension the part can undergo whilst still being recoverable. Once the elastic limit is reached, extension occurs due to the displacement of molecules with respect to one another with the molecules not exhibiting any tendency to move to its original position [114].

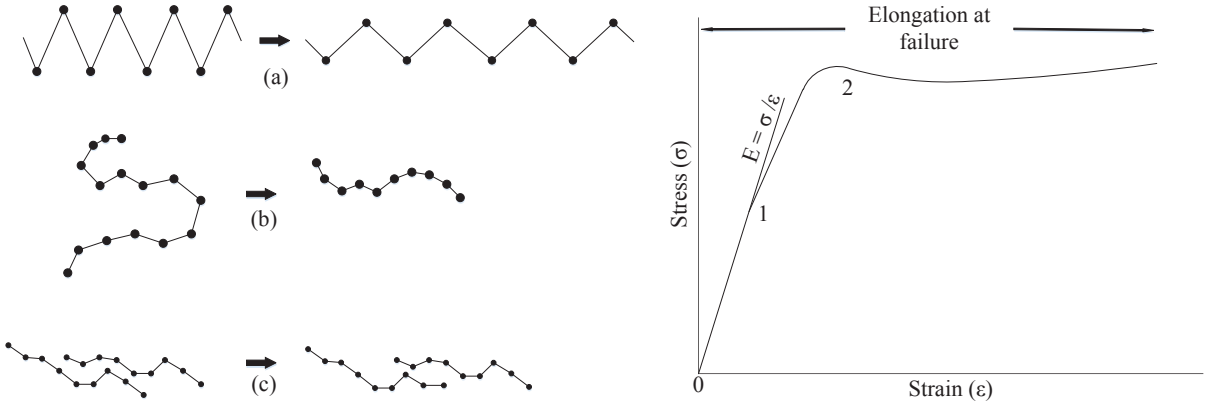

Figure 4.12 Left: Three phases of deformation in plastics. (a) Polymer molecule stretching. (b) Straightening of a molecular chain. (c) Slippage between molecules. Right: Nominal stress-strain diagram. Similar to Chanda et al. [114].

The area under the stress-strain curve gives the resultant strain energy per unit volume of the material and is related to the toughness of the material. The shape of a stress-strain curve also acts as an indicator whether a sample is soft and weak, weak, and brittle, strong and tough or hard and strong. Plastics that are described as soft and weak tend to have low stress values and a lower slope (Young's modulus). Hard materials have a higher elastic modulus (initial slope) with strong material resulting in higher Ultimate strength values. Samples with large strain energy per unit volume and high elongation is described as tough.

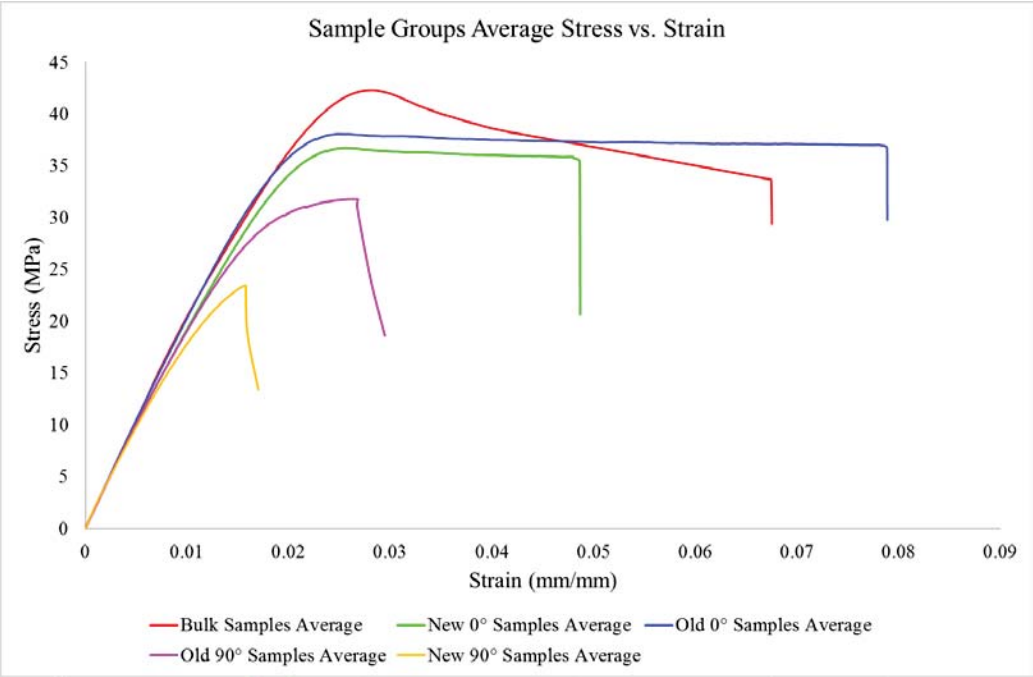

Figure 4.13 Plot of the average stress vs. strain response for all sample groups.

Fig. 4.13 depicts the respective stress-strain responses for the five sample groups. A difference is visible between the various samples groups based on raster orientation. Sample with a 90° raster exhibit sudden brittle fracture and considerably weaker than the other sample groups. The 0° sample groups exhibit much larger strain greater elongation. The responses of the re FDM samples vary between one another but are similar when the raster orientation is identical. The bulk material shows a more typical polymer response. The samples exhibit greater tensile strength and the highest initial slope (Young's Modulus). The bulk material reaches its UTS after which the part starts to fail with a significant decrease in its ability to support the applied force. Comparing this to the 0° samples, it is observed that the 0° samples experience high strain but continue to support the applied load. Even though a statistical difference between the elastic moduli of the two samples depicted in Fig. 4.14 was proven, examination of the graphs show a similar slope in the initial part of the curve.

Comparing the curves of the two 0° samples, the strain energies are approximately the same. Both sample groups had a strong and tough response having high stress values with a relatively large amount of strain before failure. However, samples in the old 0° sample groups displayed higher strain values on average. Samples in group D had two samples exhibit hard and brittle fracture behaviour with the samples failing just before and after the average UTS value for the group was reached. Samples in the old sample group displayed the lowest variance between the sample graph lines with all samples displaying almost identical paths during phases one and two (Phase one: polymer molecule stretching. Phase two: Molecular chain straightening.). A larger variation is observed in group D for the two phases as expected based on the S.D. values of the group. Samples in group C exhibited a higher strain with three samples reaching the maximum set strain value for the tests. As the parts move into the plastic region during testing, the curve does not slowly increase as is typical of polymers. Parts continue to elongate and without an increase in the stress value. During testing, it was noted that once the UTS of the samples were reached, separation occurred between the interior fill of the samples and the border roads surrounding the sample. This immediately decreases the amount of material supporting the load thereby weakening it. Parts failed soon after this delamination occurred.

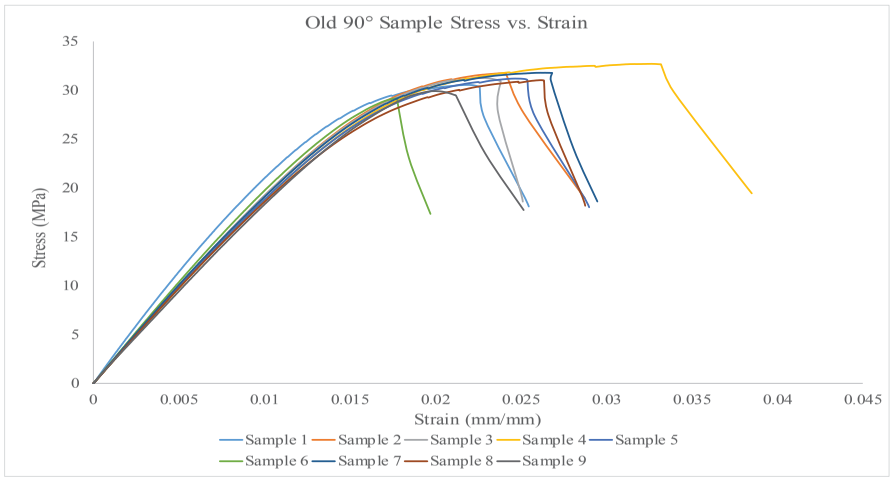

(a)

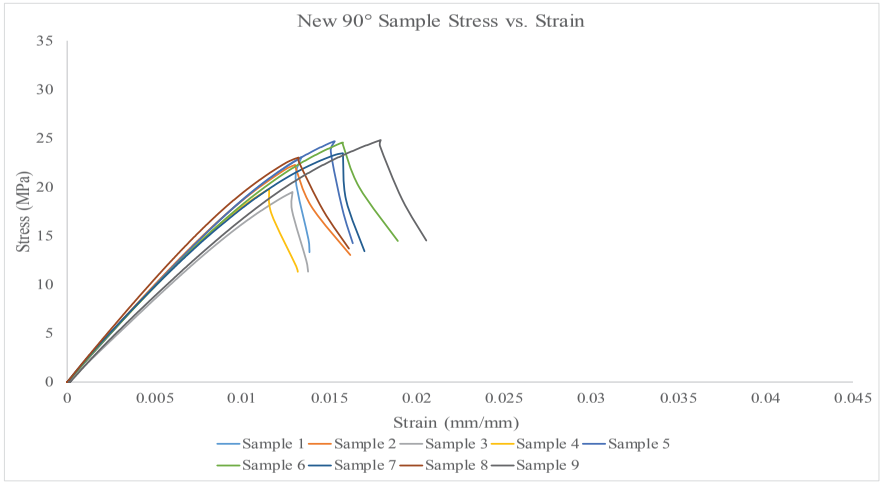

(b)

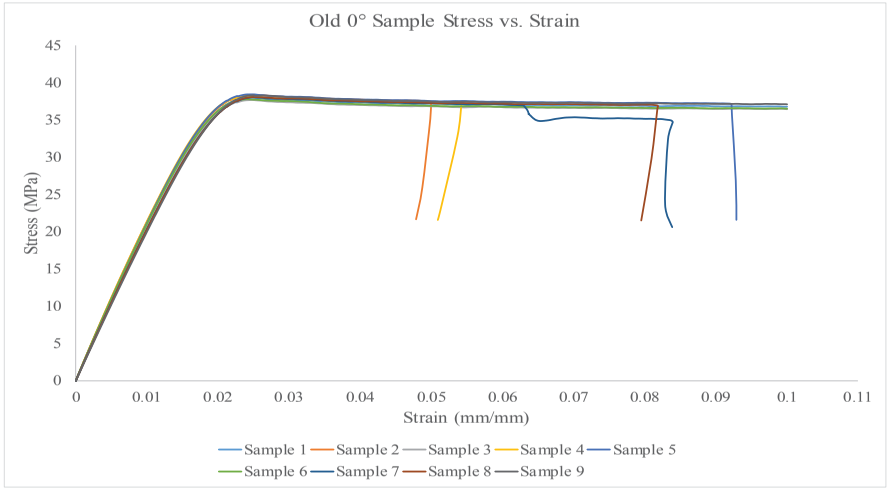

(c)

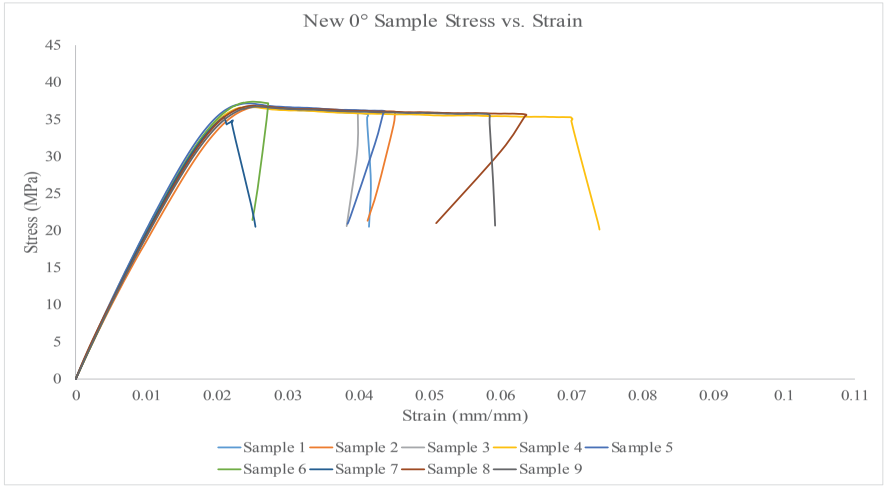

(d)

Figure 4.14 Stress vs. Strain response of sample groups A, B, C and, D by the respective plots.

Sample 7 from group C shows the most dramatic response to this delamination as a sudden drop in the stress is measured. During testing this samples delaminate with the boundary roads being propelled away violently. Other samples experienced similar boundary delamination and consequent fracture however, none as violent as this sample. The consistent higher strain values exhibited by group C with the lower variation in the strain values at failure improves the ability to use this group for any final product use over its counterpart.

Sample groups A and B displayed a more brittle type fracture with samples suddenly failing with rapid crack propagation. Either sample group experiences little elongation. Group A outperformed B with approximately 25% higher experienced strain. The stress-strain diagrams from group A samples were able to approximate those of groups C and D to a larger extent that those of group B. These samples also displayed a higher strain energy than their counterparts making these parts tougher with a greater ability to absorb energy. The achieved tensile strength was also higher. The older samples again had less variation in the resultant test lines of the different samples. This, as in the case of the 0° samples, displays the more consistent and reliable mechanical properties of the older samples.

4.5. Summary

The use of tensile testing in the evaluation and determination of mechanical part properties of FDM parts have been well used. However, to the best of the author's knowledge, a longitudinal study has never been completed comparing parts printed one and a half years apart using identical print conditions and equipment. The tests conducted in this chapter proves that a significant difference exists between the chronological sample groups with samples manufactured on a printer that is younger in age being superior. Upon visual examination, samples in the older groups exhibited a higher level of diffusion. The resultant stress, strain and, Young's modulus values along with the stress-strain curves acts in support of this difference. Results showed the older samples to be superior with samples being tougher. A comparison of the 0° samples with the injection moulded material showed the old 0° samples having the closest properties to those of the bulk material samples. The influence that raster orientation plays became apparent when comparing the 0° and 90° samples. 0° samples experienced greater elongation than their 90° counterparts. They were stronger, tougher and, less brittle. With all sample groups manufactured using identical print settings,

material and machines with the age of the machines and age of the samples being the only difference, it is safe to conclude that age plays a role in sample properties. There is a possibility that the samples age influenced their mechanical properties. However, with a lack of test values from the original group at the original print date, the effect of sample age is hard to prove. The other major factor to consider is the age of the machine. With the original batch manufactured soon after the initial release of the Stratasys Fortus 450mc and the second batch one and a half years after, the printer would have experienced some degradation over time from continuous use. The wear and tear on machine components has the potential to influence accuracy and repeatability. In a part made up of small roads bonded together, the reduced accuracy of the printer can act to magnify the sum of inaccurate road depositions, weakening the part. Even if machine degradation didn't play a role, these findings prove that there is a discrepancy in the consistency of parts manufactured on different printers of the same model. Considering the identical manufacturing conditions, it is necessary to further investigate the differences between samples groups in order to aid the understanding of FDM part properties. Through the use of SEM analysis, these samples were further examined for the diffusion level, print patterns and fracture properties in the subsequent chapter.

5. Topographical and Fracture Surface Analysis with Scanning Electron Microscopy

5.1. Introduction

Understanding of fracture mechanics of FDM parts is vital for design of strong end-user parts. A most commonly used tool for this purpose is scanning electron microscopy (SEM) which provides high magnification/resolution images of the surfaces. Numerous researchers have reported the use of SEM. Ahn et al. [30], Wittbrodt et al. [2] and Fodran et al. [53] used SEM imaging for evaluation of the fracture surfaces of their tensile samples. Similarly, Torrado et al.[76] examined the fracture surfaces of their ABS composite materials. Roberson et al. [28] investigated the fracture surfaces of their notched FDM samples for impact testing while Wu et al. [43] used it to compare the fracture surfaces of PEEK and ABS samples. None of the work completed so far investigated both fracture and topological surfaces of sample. It also hasn't been used to study the printing method based on the print patterns and induced problems such as void size comparison between samples and road consistencies.

This research utilizes SEM to examine both the topographical and fracture surfaces of the sample groups A and B as per Table 4.2. Groups C and D were not examined due to the similarities in tensile strength, Young's moduli and their respective stress-strain responses. If improvements are to be made to the mechanical properties of FDM parts, the easiest way to achieve the greatest improvement is by improving the weakest part. In the case of FDM, the weakest parts are those printed using a 90° raster orientation. Groups A and B showed distinct visual differences between their stress and strain values along with significant differences in their stress-strain curve responses. With both sample groups manufactured using identical print condition, an investigation into the physical properties such as road widths, dimensions, relative diffusion level etc. will help explain why this difference is

present. It will also help to understand why there is such a considerable difference in the UTS of the 90° sample groups. It should be noted that for the purposes of the topographical fracture surfaces, an ASTM D638 type 1 dogbone was used for the old samples whilst a type 5 dogbone was used for the new samples. As the topographical study requires samples that haven't been subjected to tensile load, due to a lack of untouched new type 1 sample, a new type 5 sample was used. The sample was manufactured at the same time as the new type 1 tensile dogbones, on the same machine using the same parameters and print stock. The section of the dogbone used for examination was the upper wider edge to closely resemble the width of the type 1 dogbone neck region. This would ensure that the print patters used for the type 1 dogbone would be similar to the type 5. For the fracture surface analysis, the test samples were used and were identical in every way except the print date.

5.2. Topographical Analysis

Topographical analysis of the samples showed various similarities in the builds. The nature of the printing process is such that for each new layer, the outer boundary is printed first. For the case of the type 1 samples, the boundary layer (shells) consists of two parallel layers as shown in Fig.5.1a. Upon completion of the outer layers, the interior of the part is filled. This fill process occurs from either top or bottom end of the samples longitudinal axis. As the printer moves horizontally relative to the Y axis (as per Fig. 5.1a), a road is completed and the next one started in one continuous path as it turns to deposit the next parallel road. This print path however is not symmetrical path perfectly round corners but rather follows the path as depicted in Fig.5.1b. As the print nozzle moves horizontally across, it has a pre-determined velocity. However, as it approaches the corner, the nozzle slows down in order to ensure accuracy in depositing the material along a non-symmetrical arc. The nozzle moves very slightly in the Y directs as it comes to a halt. As it moves to the next road parallel to the previously deposited one, a more visible arc is followed until the centre distance between the two roads is at the correct value. When the corner is turned, the nozzle again speeds up for its long linear deposition run. The same procedure is followed on the opposite end of the print fill.

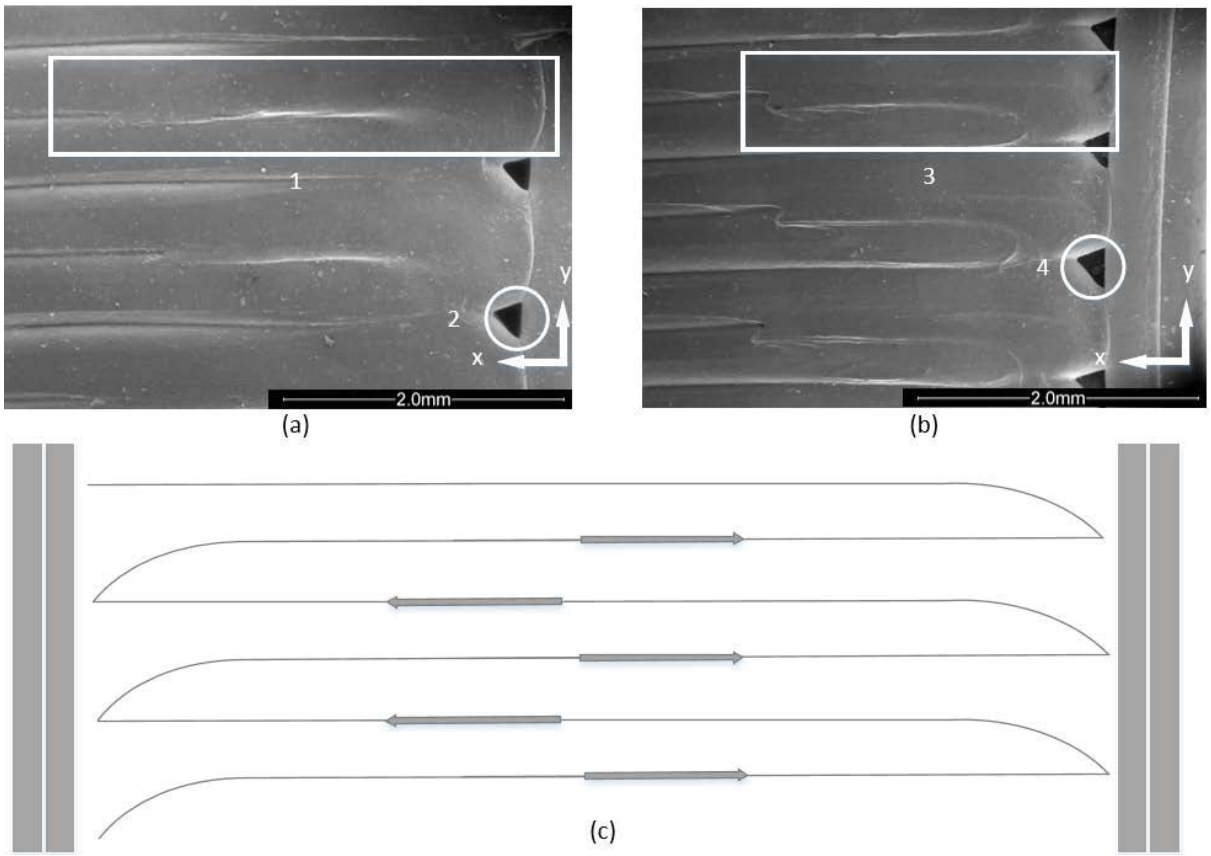

Figure 5.1 Topographical representation of a 90° raster samples with 1 depicting the smearing effect during build and 2 the triangular voids produced due to the print patter for (a) the new samples and (b) the old samples. (c) represents the print pattern followed during the internal fill process of the samples.

Because of this print pattern, two features become visible. The first is the overlapping smear effect observed as the printer accelerated around the corner arc. This pushes some material onto the surface of the previously deposited road. Even though the extrusion rate is slowed as the print head slows down, the smearing is most likely caused by excessive extrusion causing a slight build up on the nozzle. As the print-head speeds up, this material is pushed sideways onto the previously deposited road by a combination of the amount of material built up and the deposition path followed. This smearing effect isn't necessarily bad for the mechanical properties of the part as it results in better diffusion between adjacent roads and a larger contact surface between consecutive roads connected by the same arc. Examination of the topographical surface for both the old and new samples showed that this feature was consistent on either side of the same sample and present in both sample groups A and B. The average measured smearing for the new samples was 2.95mm compared to the average 2.2mm for the old samples. These measurements were consistent on either side of each of the

samples. The measurements were taken from the corner of the arc to where the smearing visibly stops as per 1 and 2 on Fig.5.1. This difference in the smearing that occurred supports the hypothesis that there was a difference in the printing process that both printers followed even though their print parameters were identical.

The second feature is the triangularly shaped voids between corner arcs. The voids produced due to the printing method result in a substantial reduction in the bonding surface area between the part fill and the shells. This reduces the strength of the part as each of these acts as a stress raiser for rapid crack propagation. When the part is subjected to a tensile load, as in the case of a tensile test, each of these voids acts to reduce the contact surface between adjacent roads. The average horizontally measured width for these voids is 240µm ± 20µm. Therefore, the printing process results in a void between each alternate road with an approximate volume of 0.00861 mm^3 based on the measured layer height of 250µm (height measured from fracture surface SEM images). It should also be noted that the void shapes on either side of the print were similar in size and shape for the old samples.

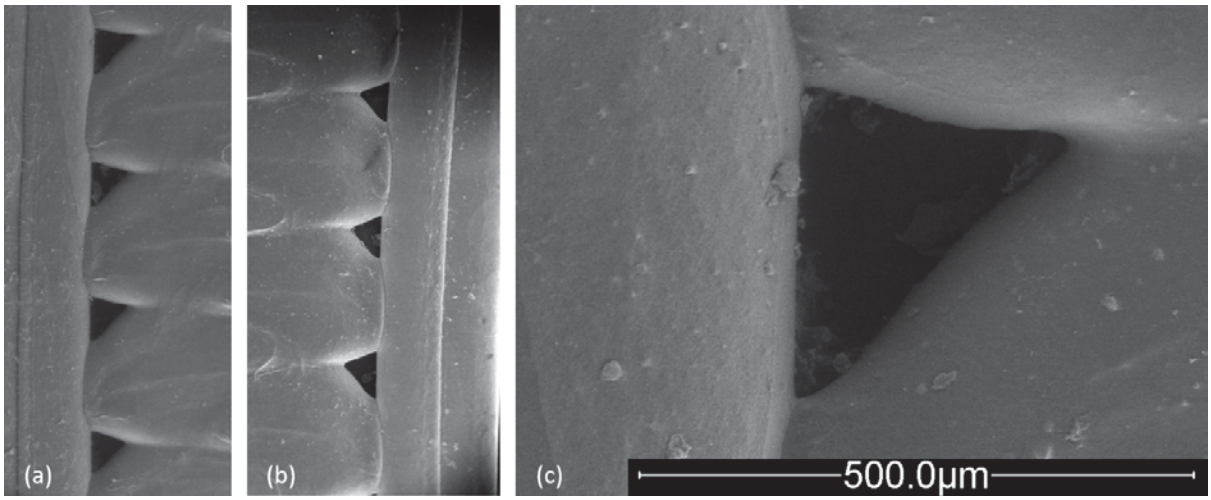

Figure 5.2 SEM topographical images of the old 90° samples (a) Triangular voids on the left of the sample, (b) Triangular voids on the right side of the sample and, (c) 200 x magnification of a triangular void.

A comparison of the voids for the new samples showed differences in the shape and size between the left and right sides of the samples. Voids on the left of the sample depicted by Fig.5.3a and b show rounder edges to the triangular voids. Voids on the right side shown in Fig.5.3c and d had sharper edges. These edges will have a greater effect on the potential for crack propagation compared to the voids on the left as a sharper corner increases the stress

concentration. The approximate volume for each void on the right side was 0.00653mm^3 and 0.00567mm^3 on the left. Considering the lower void volume, a higher level of diffusion is expected between roads and layers as the reduced size in the void indicates the deposition of the material was closer and more compact. The overall surface area of the contacting material around the voids is also higher as a result of the inconsistencies in the printing process. Comparing the void volumes between the old and new samples, results showed that the overall difference in the volume of material absent as a result of the introduction of the voids was 30% higher in the old samples compared to the new.

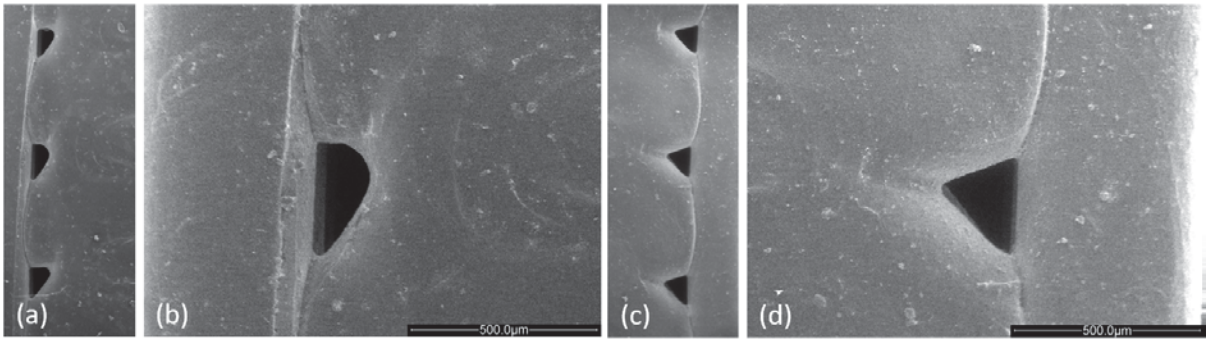

Figure 5.3 Comparison between the new samples left and right resultant print voids with several voids depicted for either side by a and c. B and d depicts a magnified view of a representative voids for either side of the sample.

Further analysis of the topographical surface showed the inconsistency of the deposition process as voids were sometimes introduced between adjacent roads. Fig.5.4d shows one such void present on the new 90° samples. Compared to the old 90° sample the roads have more inconsistent shapes and the old samples do not display any voids. Voids such as these are suspected to be present through the entire sample creating points of higher stress when the sample is subject to a load. These voids also reduce the size of the bonded area in a plane perpendicular to the longitudinal axes. The void depicted in Fig.5.4d measures 776µm long with a width of 116µm. Considering the difference in strength between the old and new samples, relatively large voids such as these will reduce the tensile strength of samples and play a significant role in the reliability and predictability of how a sample would respond when subject to a load. These voids occur as a direct result of the thermal cycles the part is subjected to. As the number of layers in a part increases, the number of heating and cooling cycles it is subjected to also increases. FDM printed parts experience volumetric shrinkage of the polymer layers during the cooling and solidification process resulting in residual stresses

in the part. These stresses may result in distortions in the part as well as distortions in the individual roads leading to inter-layer cracking, and delamination. These stresses affect the areas where the inter-raster bonding is weak and control the fracture paths of FDM specimens [31].

During the SEM analysis, a difference was found between the distances from one void to another. The bonded length between the corner arc and the shells was measured void to void and the new sample had a considerably larger bonded area measuring 780µm compared to the 540µm of the old samples, giving a difference of 31%. With this bonding pattern, consistent along the longitudinal axis of the sample, the sum of the overall bonded surface area between the shell and internal fill will be considerably greater for the new samples based on the topographical analysis. Thus, it would be expected that the newer sample will be less prone to delamination between the fill and the shell. However, this statement is based purely on the examination of the topographical surface. With the knowledge that the old samples are superior in strength, further investigation into the fracture surface will give a more reliable result as the inter-layer diffusion throughout the entire sample can be analysed. These findings aid in proving that the print process does vary based on machine age and manufacturing differences between identical machines.

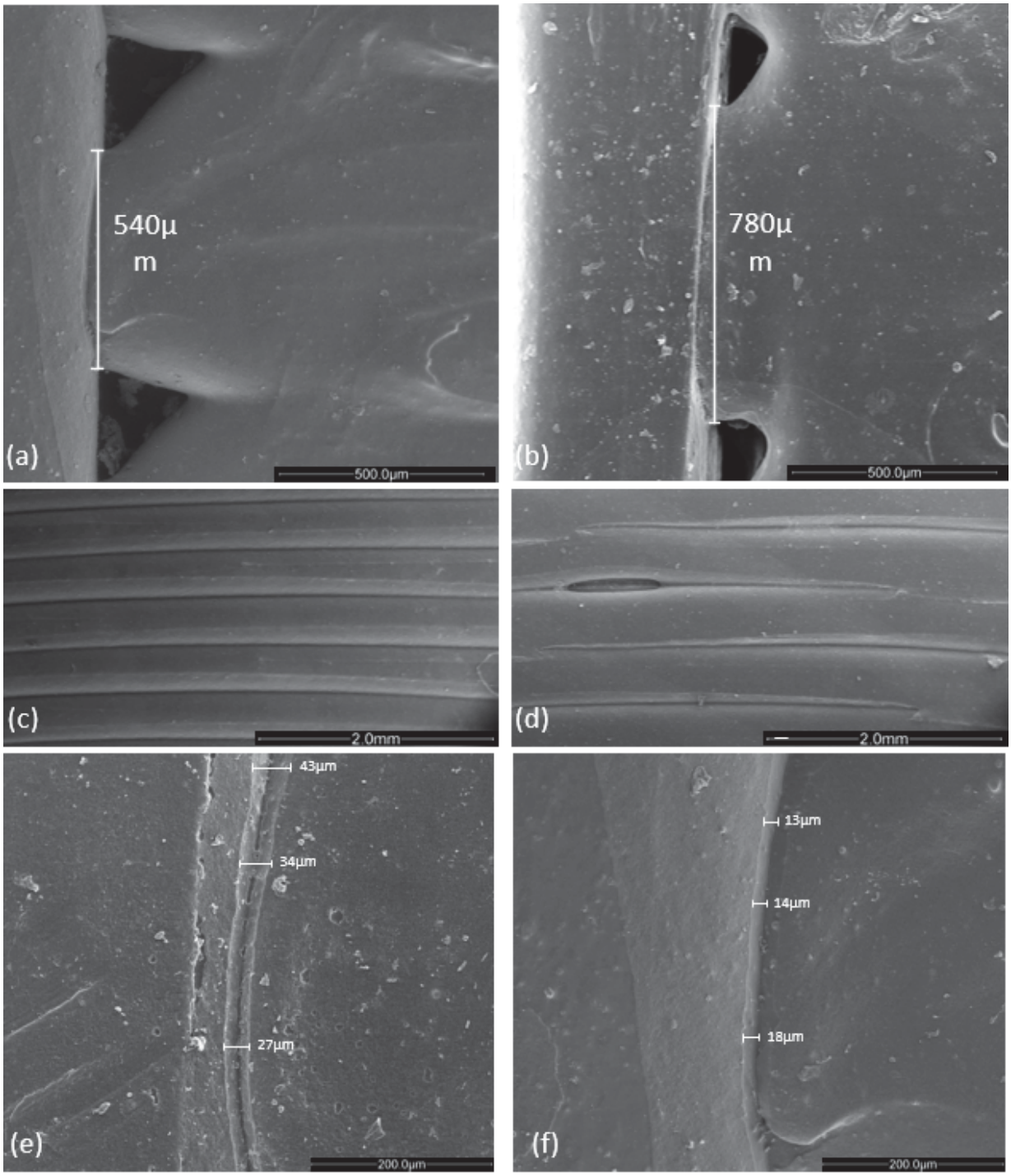

Figure 5.4 Topographical views of: (a) Bonded length measurement between consecutive voids for the (a) Old sample group and (b) new sample group. (c) The old sample roads without the presence of voids. (d) The new sample group depicting a void. SEM images of (e) new and (f) old sample partial delamination due to shrinkage.

In the FDM process, after extrusion and deposition of the roads they start to cool and some shrinkage is experienced. Investigation of the topographical surfaces of the two samples shows the effect that this shrinkage had as per Fig.5.4e and f. The new sample group showed

considerable shrinkage compared to the old samples. In some areas, this shrinkage resulted in visible delaminated areas more than 3 times that of the old samples. The old sample also had a more consistent amount of shrinkage and subsequent delamination throughout the bonded area between the internal fill pattern and boundary layer. This increased shrinkage in the new sample may indicate higher thermal cycles experienced by the sample compared to the old sample. With the observed shrinkage, it is questioned whether consideration is made for the phenomena during the deposition path creation.

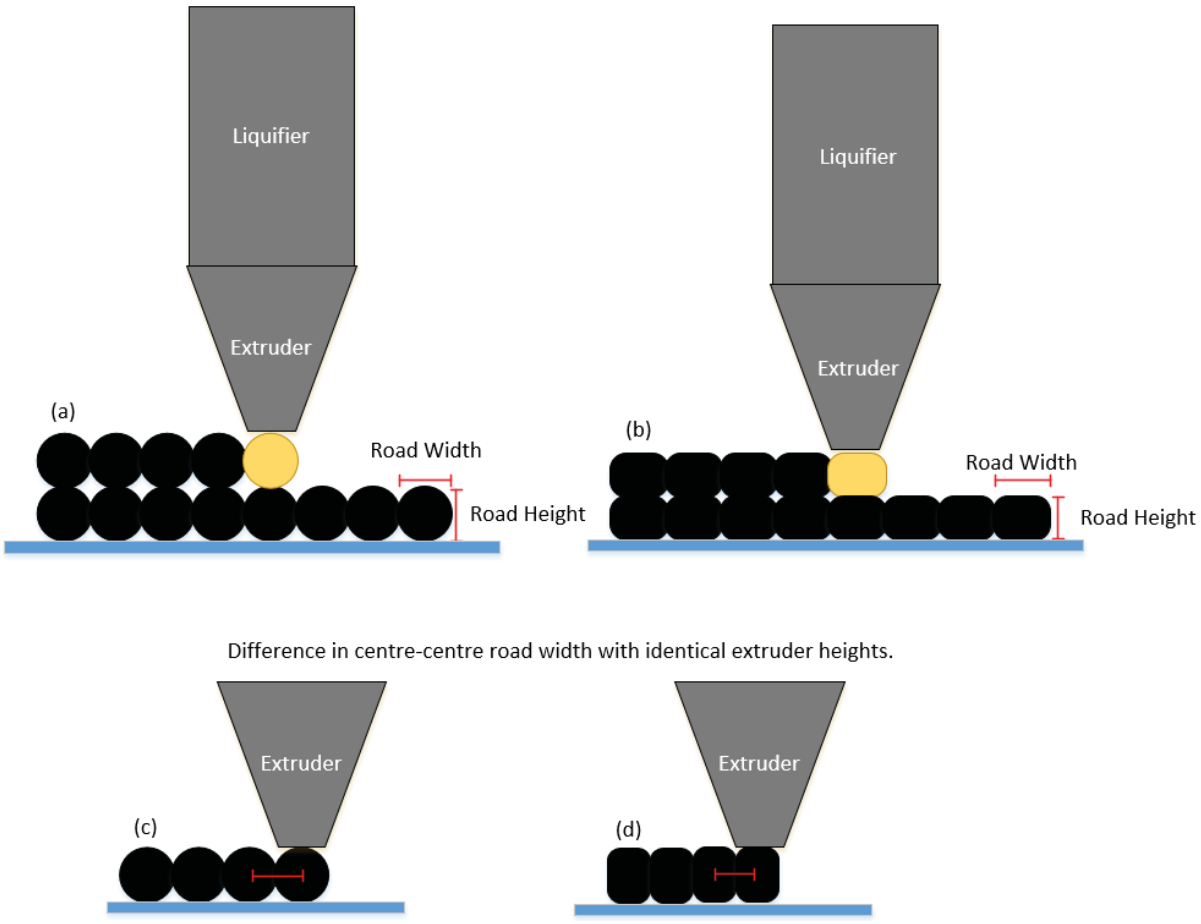

Figure 5.5 Representation of (a) road shapes with a zero-layer height setting, (b) roads with a more oval shape when printed with a negative air gap. Representations of roads printed using identical layer height settings depicted by (c) roads printed with the centre-to-centre road distance equal to the road width and, (d) with a centre-to-centre road distance less that the road width.

With the print path determination based on the slicing algorithm taking several factors into account including the expected diameter of the extruded road, it is important for the algorithm design to know what effect this shrinkage has on the part. Does the algorithm determine the road centre to centre distance based on the hot extruded road diameter or the

cooled diameter? Should the deposition path be based on a warm diameter with the road centre to centre distance slightly large due to print inconsistencies, the cooling of the road would have a greater delaminating effect on the part substantially weakening it. As depicted in Fig.5.5c, the roads are deposited (based on the hot diameter with a distance equal to the centre to centre road distance) and shrinkage start to occur, the delamination would be similar to what is depicted in Fig.5.4e and f. If that distance is increased, the initial amount of material bonding that occurs would be reduced due to the circular shape of the deposited material. Upon shrinking, the already lower bonded area would further delaminate resulting in a lower bonded area when cooled. If the cooled road diameter was used, the road centre to centre distance would be reduced. The adjacent road deposition while hot would force the roads against one another, potentially increasing the bonded surface area in the same way that a negative layer height greatly increases the bonded surface between layers. Fig.5.5d depicts the deposition of a road with a smaller centre to centre road distance and the resultant shape of the roads and relative bonded areas. Comparing these with the more circular shaped roads deposited with larger inter-road distance, smaller bonded surface areas occur between the circular roads. This small delamination effect could also be because of the layer height of the samples which will be examined as part of the fracture surface analysis. However, with the layer height setting defining the thickness of each print layer, this could also influence how large the size of the measured shrinkage effect is. A larger layer height means the height of the nozzle is increased and fewer layers are required to complete a part [116]. Because of this increase, the deposited material will have a difference in shape depending on the relationship between the extruded diameter and the layer height. A lower layer height will deposit the material with less space between the nozzle and the previously deposited layer forcing the material outward and against the adjacent road. This changes the shape of the extruded material to a more rectangular shape with rounded corners instead of the circular extrusion shape. As the layer height is increased, the deformation of the extruded shape changes to a more oval shape and thus, less material is forced sideways away from the nozzle as there is more space for material between the nozzle and the previous layer. This reduction in the horizontal movement of the material reduces the force with which the material is pushed against the adjacent road and results in a smaller bonded surface as depicted in Fig.5.5d.

Further analysis was done on the topographical nature of the two samples by comparing their relative road widths from one side to another. This evaluation brought to light the differences in road widths between the samples. Figure 5.6 shows a scatter plot of the widths as measured from the datum. The datum was chosen as the bond surface between the boundary layers and the internal fill of the sample. An investigation into the road width showed an average width of 0.41mm for the old sample and 0.5mm for the new sample, which is equivalent to a difference of 19%. As the road width is directly impacted by the nozzle height, as previously discussed, assuming the extrusion rates for the two samples were identical, the old samples are expected to have a greater layer thickness. The newer samples having greater road widths are expected to present thinner layers as the material would theoretically be pushed outward. However, if this was the case, the inter-road and layer bonding should be superior to that of the old samples as all samples were manufactured using identical parameters.

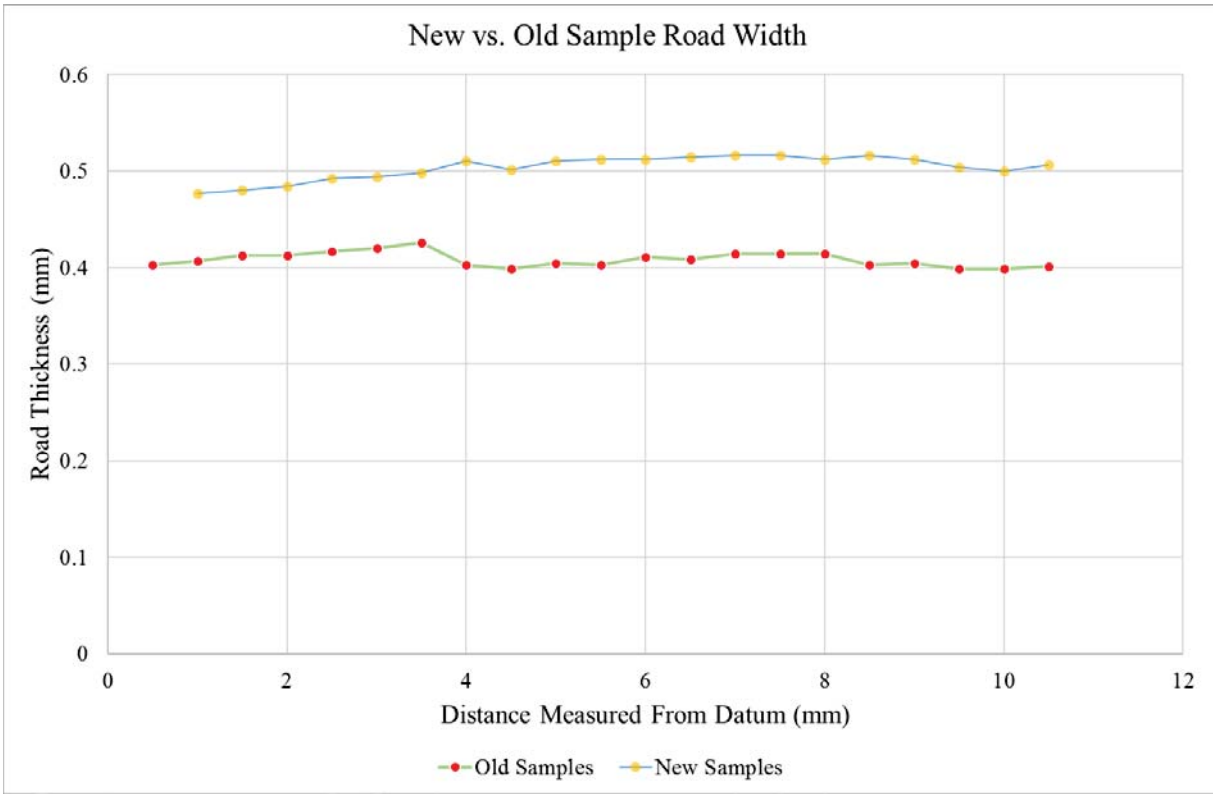

Figure 5.6 Average road width for both the new and old samples measured across the topographical surface.

Measurements across the topographical surface showed inconsistencies in the road width for both samples. The variation in road width was greater for the new samples indicating lower accuracy in the deposition of the printed part. This is consistent with the corresponding age of

the machine and the hypothesis that machine age affects print quality. Observation of the layer thickness for the old samples indicates that the layer width is identical at either end of the sample. In both areas, the print speed would be identical and located just after the extruder turns the corner. After this point, there is an increase in layer thickness. This could possibly be explained by the increase of both the extrusion and deposition rate. As the print-head move linearly and the extrusion rate increases but the increase is not proportional to the acceleration of the print-head, more material is deposited. When the layer height is constant, the width of the road subsequently increases. When the print-head reaches its target speed at the centre of the sample, the deposition rate and extruder speeds align and the road thickness returns to the target width. As the extruder starts its deceleration towards the other end of the sample, at 8mm from the datum, the proportionality between the extruder and deposition rate changes again resulting in the increase in thickness of the roads. Near the approaching corner, these two variables reach the appropriate speeds again and the roads' width returns to the desired values. A similar pattern is visible in the new samples as well based on the road widths. However, there is a consistent difference between the road thicknesses on the both ends of the sample. This could potentially be due to slight warping of the part resulting in the effective distance between the previous layer and the print nozzle to vary across the print surface.

5.3. Fracture Surface Analysis

Fracture surface analysis of the two samples was completed with each sample's fracture surface broken into six equally sized sections. Initial comparisons of both samples' fracture surfaces showed dramatic differences in their fracture surface morphology as depicted in Fig.5.7.

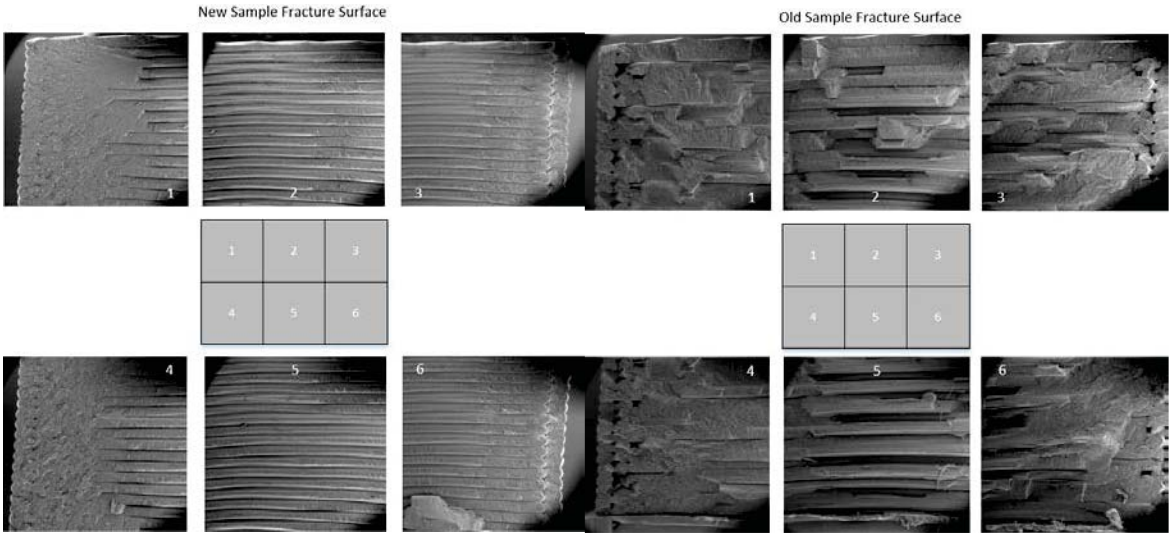

Figure 5.7 Fracture surface images of the new sample surface sectors on the left and the old sample on the right

5.3.1. New Fracture Surface Analysis

Examination of the new fracture surface revealed a part that had different levels of diffusion on either side with an almost fully diffused edge on the left. The diffusion level was so high that it was hard to differentiate between the boundary layer and the internal fill with only the triangular voids marking the boundary as per Fig.5.8a. This diffused section ranged between 1.95mm and 3.2mm in width from top to bottom. A change in the morphology is visible between the top and bottom with the top having a smoother surface becoming more irregular towards the bottom. This however is most likely due to the method of fracture experienced by the samples. A magnified view of the left side shows linear lines all converging at a specific point indicating the direction of crack propagation (Fig 5.7). This point in the sample exhibits a brittle fracture method supported by the stress-strain curve results obtained in chapter 4 and the fracture surface evaluation. The lack of visible layers on the left is likely due to the complete level of diffusion resulting in all the layers bonded together in the same way as a bulk material. Therefore, during the fracture process, the fracture experienced on that side of the sample will not necessarily follow the same plane as the delamination experienced between adjacent roads. Fracture might rapidly occur in a more 3D direction due to stress concentrations and weaknesses in the bonds of the fully diffused area. This means that fracture will continue in the same direction on the x-z plane with a possibility that component be introduced in the y-direction veering off of the pure delamination in the x-z plane.

Comparatively, the right side of the samples did not exhibit similar levels of diffusion. However, there are obvious signs that the level of bonding between adjacent layers are a lot stronger towards the right side when compared to the roads toward the centre of the fracture surface. The boding surfaces of the consecutive layers are all flat with flat bonding surface width varying between 1.4mm and 1.7mm. These sections show that between adjacent roads in the same x-y plane, bonding occurred for almost the entire thickness of the layer with those sections of the roads having a shape like that depicted in Fig.5.5d. The bonding between the internal fill and boundary layer however was not complete compared to the left of the sample with the separation plane between the boundary and fill clearly visible. This confirms the findings from the topographical study stating that there was a visible difference between the left and right side of the samples' diffusion level. The triangular shaped voids present on both sides of the fracture surface are more pronounced on the right. These are the same voids as described in the topographical analysis and this analysis proves that these are present throughout the sample in each layer.

Fig.5.8d shows a material section from the other half of the sample not pulled away during fracture. This could likely be caused by a void in the internal section of the sample creating a stress concentration which allowed the material to not experience delamination but rather fail through the road itself. Another obvious feature in both the fracture and topographical imagery is the distortion in the roads and layers because of the sample's thermal cycles and subsequent stress build up during manufacture. Based on research by Sood et al. [22] it is expected that as the layer thickness increases, the tensile strength will increase. This is due to the weak interlayer bonds that occur due to high temperature gradients towards the bottom of the samples.

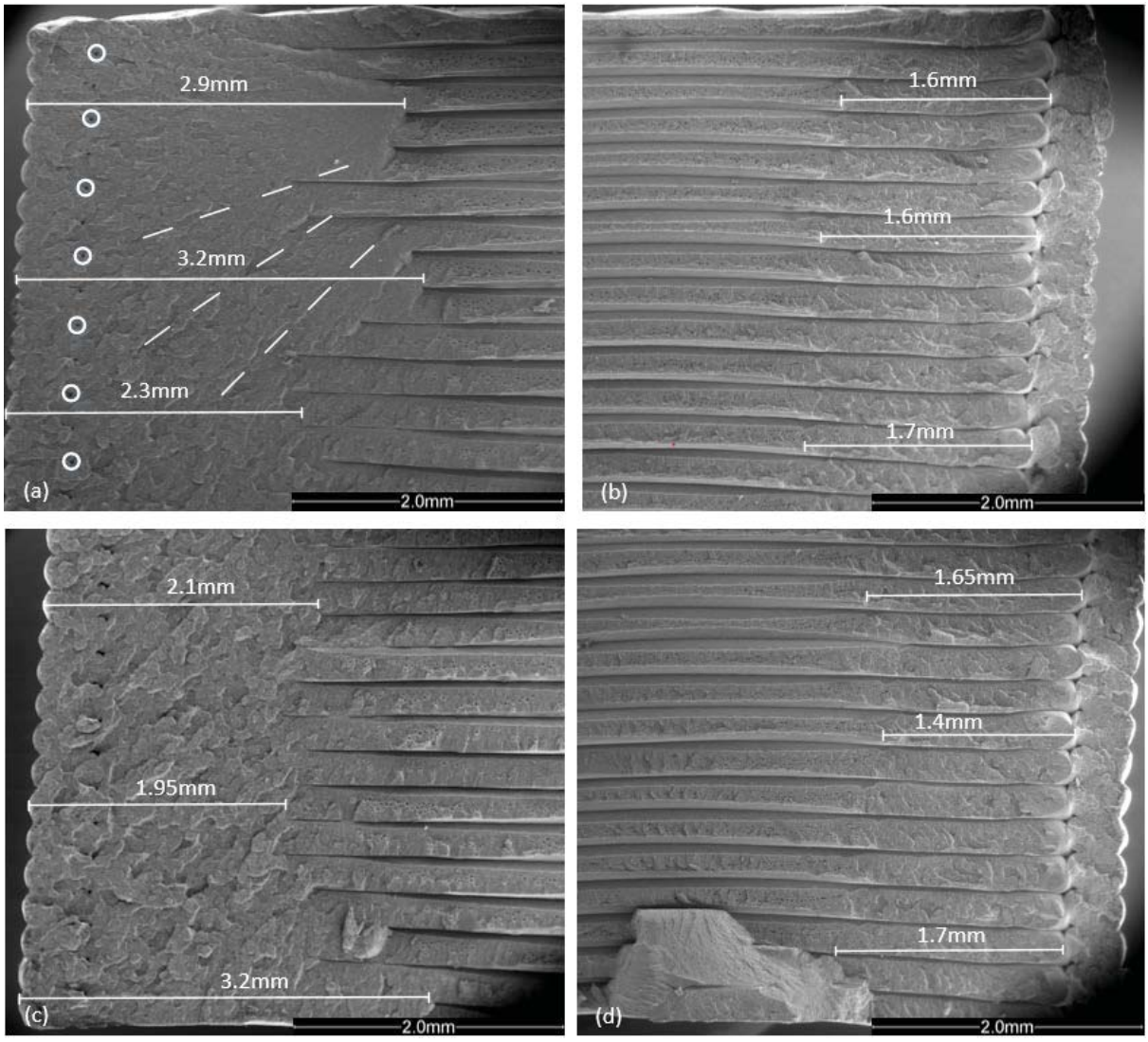

Figure 5.8 53x Magnification SEM images of the new 90° samples fracture surface with measurements of the diffused areas on either side and the striped lines indicating the direction of crack propagation. (a) Corresponds to sector 1, (b) to sector 3, (c) to sector 4 and, (d) to sector 6 as per Fig. 5.7.

As the layer thickness is increased, fewer layers are required to complete the build and the distortion effect is minimised [117]. With these samples comparing the roads leading to the centre of the sample from either side, it is noticed that the bonded area on the left is larger than that on the right. Roads on the left have flatter surfaces in the y-z plane indicating larger bonded surface areas before fracture. Roads on the right moving in towards the centre have a rapid reduction in this surface area after the initial 1.4-1.7mm well bonded area. It should be noted that the datum for measurement from either side was different. The left was measured from the outside boundary layer as the diffusion continued through the entire area whereas

the right samples were only measured from the inside of the boundary layer. This was done as there was a definitive separation between the boundary and the internal fill.

The difference between the outer regions and interior of the parts is a result of the variation in printing and extrusion speed during manufacture. As previously described, when the extruder approaches a corner, both the extrusion speed and the speed at which it travels across the x-y plane show down. This variation in speed and extrusion results in variations in the volume of material deposited per unit area. As the printer approaches the edge of the sample, it slows down meaning there is more time for the material to be accurately deposited and forced into the surrounding areas and against adjacent roads. The proportion of material deposited during this slower speed is most likely higher as the same area on the sides compared to the centre showed larger diffused areas. As the print-head accelerates, the proportion of extruded material and x-y head speed reduces and the material is unable to flow into the adjacent road thoroughly resulting in reduced the surface contact area. Examination of Fig.5.9 however shows that in the centre of the fracture surface, the width of the inter-road bonds widens and then become narrow again. This results in a variation in the inter road bonded widths. The bonded width starts equal to the layer height on the left side of the sample, moving toward the right the bonded width narrows between the left edge and the sample centre, at the centre it increases again and narrows moving further to the right. The full layer height is again bonded between adjacent roads on the right.

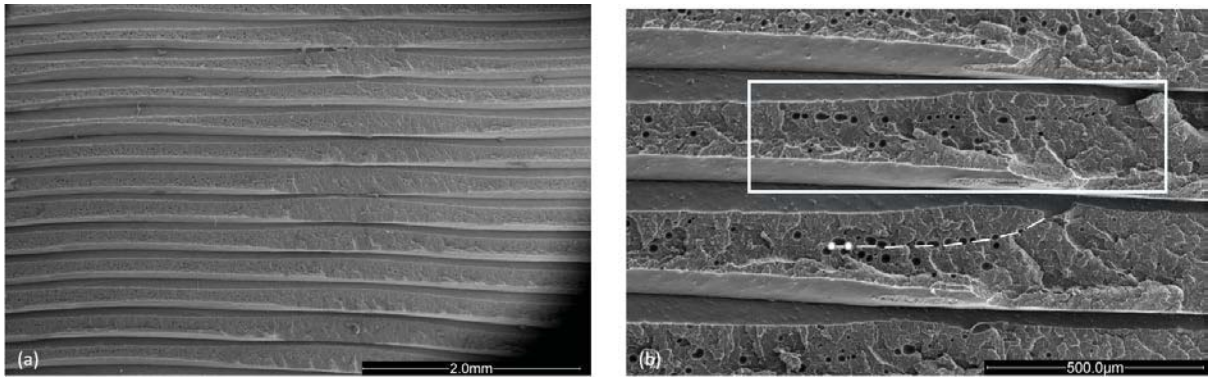

Figure 5.9 SEM images of (a) image of the central layer regions showing the variation in the bonded surface width and (b) the bubbles induced in the right side of the sample with the pattern represented by the white intermittent line.

Fig.5.9b shows bubbles introduced into the roads during the extrusion process. These bubbles appear along the fracture surface and then disappear on the left of the sample where there is

the high diffusion area. The lack of bubbles on the left fully diffused area could possibly mean that they simply aren't visible. Since the delamination along the y-z plane won't necessarily follow through the entire plane once it reaches the completely diffused area, fracture could potentially occur into the material of the roads themselves. Because of this, the bubbles would still be present in the bulk section but hidden in the y-z delamination plane with the fracture not extending through the entire plane but occurring somewhere parallel to the plane through the road material. The print-head likely introduces these bubbles as it starts its acceleration through the central region of the part. There is an absence of bubbles in the right side of the sample's fracture surface where the deposition rate and head speed is considerably lower. As the head accelerates and the inter road fused area subsequently reduces, these bubbles are introduced following a path as displayed in Fig.5.9b. A small notch is also visible at the point where these bubbles are introduced. This notch might be a result of a sudden jerking motion experienced by the head as the speed suddenly increases.

The average layer thickness was measured across the fracture surface of the sample as depicted in Fig.5.10. The average layer thickness for the sample was 0.257mm with a standard deviation of 0.006095mm. There is a downward trend in the layer thickness of the sample towards the right of the face.

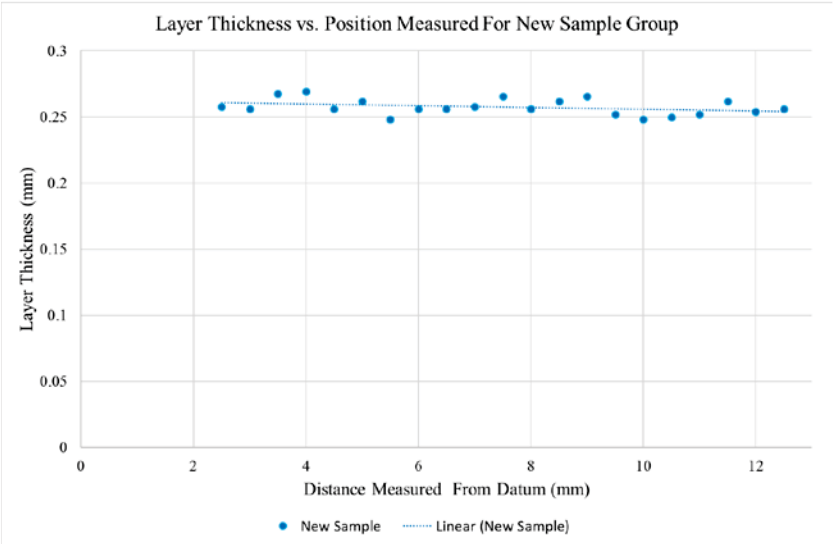

Figure 5.10 Average layer thickness measurement across the new sample fracture surface corresponding to the distance as measured from the datum. The trend line shows a slight decline in layer thickness of the roads moving to the right side of the fracture surface.

5.3.2. Old Fracture Surface:

Examination of the old fracture surface revealed vast differences between the old and new samples as depicted in Fig.5.7.

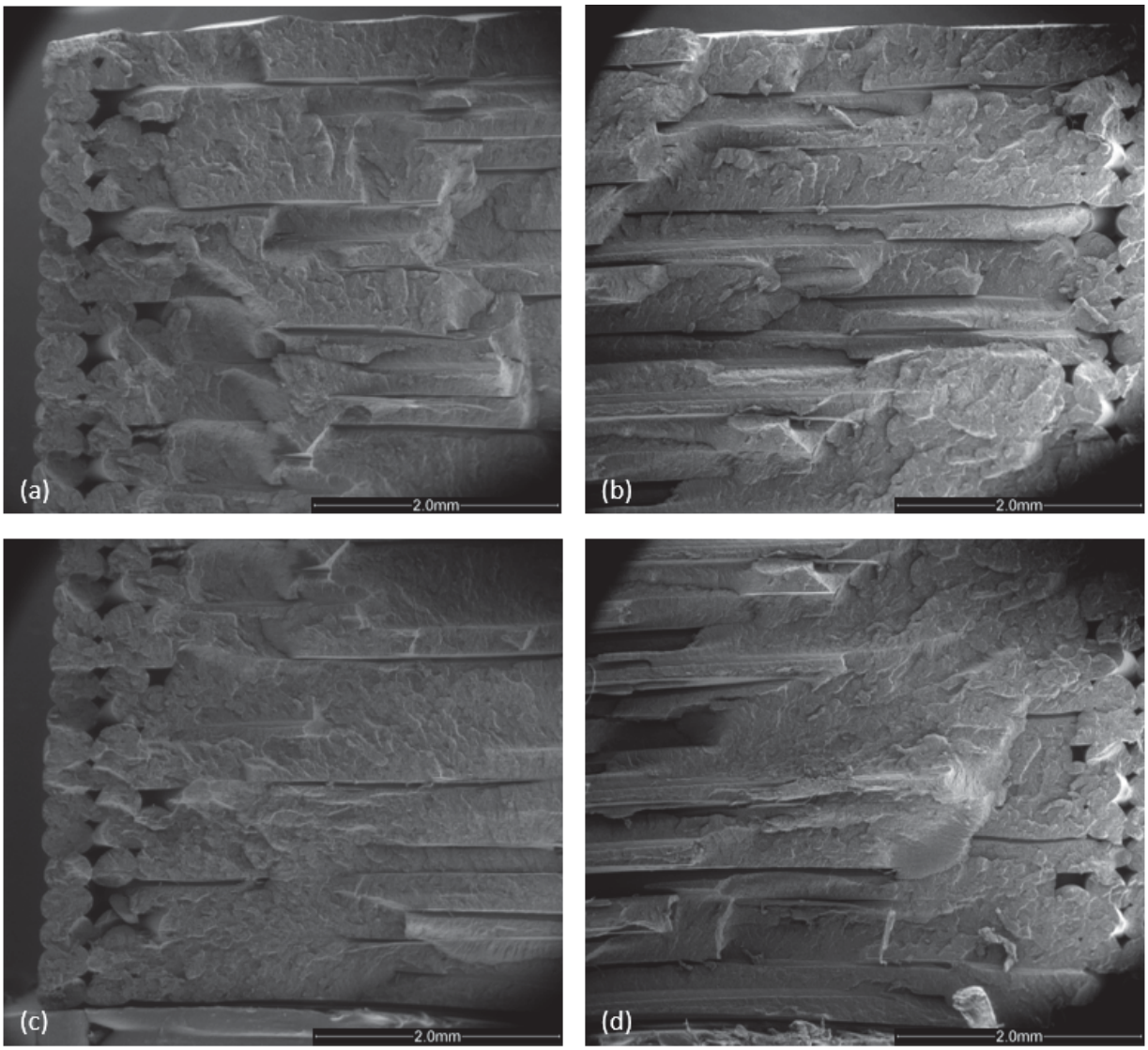

Figure 5.11 SEM imaging of the old samples fracture surface of sectors 1, 3, 4, and,6 for a, b, c and, d respectively.

Fig 5.11 shows the fracture surface for the old samples sectors 1, 3, 4, and, 6 respectively. Comparing these four sectors, no significant difference can be found. All four sectors have very high diffusion. Even though it is still possible to see some horizontal layers, most of the sample layers have fused together. The bonding between the two roads forming the boundary layer isn't as complete as the new samples. There is a definitive vertical line of large voids, a

result of the printing process. Examination of the boundary layers also showed road more ovular in shape compared to the new samples, possibly suggesting a slight variation in the extrusion nozzle height during deposition. The surface suffered from “road pull-out” with adjacent roads having so strong bonds that during fracture they were pulled out together results in an uneven fracture plane. Comparing the fracture plane with the new samples, the level of diffusion is significantly higher. The layers in the new samples along with their diffused contact surfaces were clearly visible with only the left side exhibiting similar diffusion patterns to what is present in the old sample’s entire fracture surface. Based on the knowledge that higher diffusion in parts results in stronger mechanical properties[31], the level of diffusion observed in the old samples correspond well with the results from the tensile testing that the old samples outperforming the new. The voids present in Fig. 5.11 are much larger compared to the new samples. However, the bonded area of the old samples is far greater than that of the new. The tensile results showed that there was only a 17% difference in strength between the old 0° and old 90° samples. This will be due to the 90° sample’s diffusion quality. As the quality of the bonds increases, the material starts to exhibit properties more akin to the 0° samples and that of a homogeneous sample. A raster orientation that is parallel to the loading direction greatly increases strength as the load is supported by the extruded fibre. These individual fibres, although not perfectly bonded, are still homogeneous on their own. In the case of the old 90° samples, the high level of diffusion meant that the material properties became far more homogeneous. As a result, the fracture did not occur along a single y-z plane due to delamination between the adjacent horizontal roads as in the case of the new 90° samples. Fracture was far more irregular with the part failure due to fracture of the material due to crack propagation within the material itself and not delamination between layers. This results in superior tensile strength. Even though there are clear layers along the z-axis, roads would fully diffuse in groups between two to four and then have a noticeable space between the layers. These are due to the shape of the roads. When the roads are extruded, they still retain their ovular shape. The older sample had roads that were altered during the deposition process and became more rectangular. It is observed that some of the roads still retain their curvature resulting in partial bonding between adjacent roads in the same x-y plane. The large gaps left between layers are forms as a result of the road pull-out effect that occurs during the rapid brittle fracture of the part.

Examination of the central region of the old sample showed the road pull-out more clearly. It can be observed that similar to the new samples, the roads in the centre were more ovular in shape due to the print-heads acceleration and higher print speed in the centre of the sample. Roads displayed lower road-to-road diffusion with the diffused surface being smaller than on the sides. Analysis of the difference in diffusion between the sectors of the fracture surface led to the conclusion that during the brittle fracture in these samples, sectors 1, 3, 4, and, 6 experiences rapid fracture in all three axes starting on one side of the sample. As the cracks propagates through the solid region, the irregular fracture through a predominantly homogeneous section results in the observed stair effect. Further, the crack continues to propagate to the central region of the sample where the bonding is lesser and the delamination along the y-z plane starts to occur. This delamination is not along a single y-z plane. It occurs along multiple parallel planes depending on the propagation of the cracks in the highly-diffused regions. When multiple cracks propagate, several cracks move deeper into the sample while others move more outward until a y-z plane is reached in either direction and the weaker diffused roads delaminate. Upon reaching the opposite highly diffused region in the sample, this delamination ceases for the most part and failure continues due to crack propagation through the solid material rather than delamination. This failure through the material rather than delamination is visible in Fig.5.12 in the white box marked '2'. The transition of crack propagation can be observed that occurred through the solid material making its way to the nearest y-z plane where delamination occurred between the two adjacent roads.

Another major difference between the old and new samples is the absence of the bubbles along the delaminated surface as observed in the new samples. These might have not been introduced to the sample due to several reasons. The temperature on the extruder head, though software controlled, might have been slightly different. Thus, the temperature on the older prints could potentially have been more suited for the material thereby not causing bubbling in the material. As these bubbles are only present in the new samples, it could possibly be that the nozzle on the printer used to manufacture the parts was past its design life and as a result suffered from slight deformation.

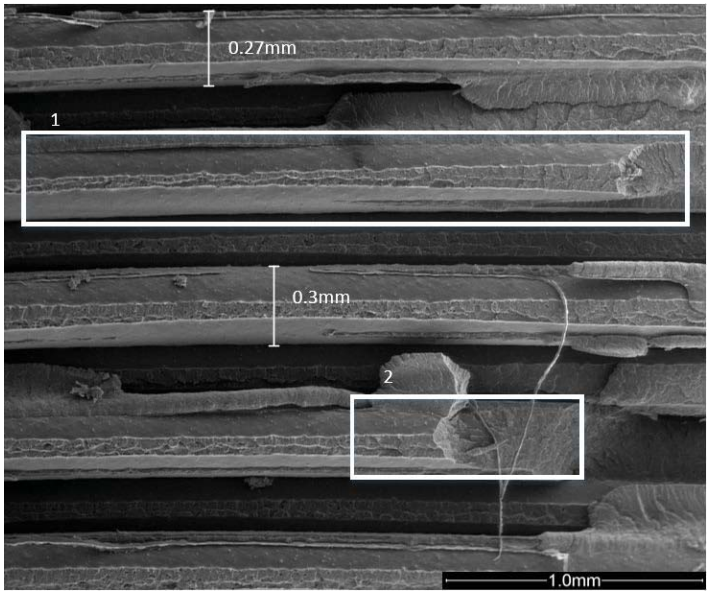

Figure 5.12 100 times magnified SEM image of the central fracture surface region for the old sample.

Another symptom of a machine used to manufacture identical parts is that due to its age and number of hours run time, it suffers from slight inaccuracies due to wear and tear. Alternatively, slight variations in machines might be present. Even though the machine models were the same and acquisition by the manufacturing companies was at the same time, machine to machine variation could likely be present which affected the comparability of parts manufactured on them.

Due to the nature of the diffusion in the old sample, it was not possible to achieve accurate measurements across the width of the surface as previously done. However, random measurements of single layers were completed where possible. The average layer thickness was 0.27mm. In addition to the superior diffusion in the older samples, the increase in layer thickness could also improve the tensile strength in parts as found by Sood et al. [22]. However, it was difficult to achieve an accurate layer thickness measurement from the sample. The print height setting for both samples was identical with an Air Gap setting of -0.01mm. Based on the obtained measurements for the old and new samples, their average road thicknesses of 0.27 and 0.26 respectively is close enough to assume that the z print heights were identical. A summary of the differences between the old and new 90° Topographical and Fracture surface sample analysis is shown in Table 5.1.

Table 5.1 Summary table of the old vs new samples topographical and fracture surface features.

Samples	Old 90°	New 90°
Topographical Surfaces		
Void Volumes	0.00861mm^3 left and right	0.00567mm^3 left and 0.00653mm^3 right
Average Road Widths	0.41mm	0.50mm
Average Observed Shrinkage	34.6µm	15µm
Bonding Size Between Road Corners and Shells	540µ	780µ
Corner Smear Sizes Between Roads	2.2mm	2.95mm
Fracture Surfaces		
Average Diffusion Size of Sample Edges	Not measurable. Most of the sample is diffused	2.61mm left and 1.59mm right
Average Layer Thikness	0.27mm	0.257mm
Bubbles Present	No	Yes
Road Diffusion Level	High, roads not easily visible	Low, roads clearly visible
Fracture Plane	The x-z plane with some fracture through the y plane	Predominantly along the x-z plane

5.4. Summary

The building mechanism of FDM parts is a complex phenomenon. The effect of various factors and their interactions can be observed. However, it is hard to assign exact reasons for the observed interactions. Some of the possible reasons have been outlined in this chapter. Through the use of SEM analysis, both the topographical and fracture surfaces of the samples were examined and compared. Significant differences were discovered between the sample that aid in the understanding and explanation of the superior quality observed in the old samples. A comparison in the topographical structures of both samples showed that the print

pattern is not a symmetrical process. Parts are printed using a process where the print-head speed and extrusion speed is continuously changing along a path which results in triangularly shaped voids to form between the boundary layer and internal fill. This also causes a smearing effect observed in both samples as the head moves around a corner. The size of the triangular voids was 30% larger in the old sample. This resulted in narrower bonding areas between the boundary-fill sections. The continuous change in printer speeds also result in road widths that vary. A significant difference in the road widths between the old and new samples exist. The observed pattern in the road width variation coincides with the points where the print-head appears to accelerate and decelerate.

Evaluation of the fracture surfaces revealed the greatest difference between the samples. New samples were found to have inconsistent diffusion across the fracture surface with the left side having almost complete diffusion between layers whilst the layers were all visible on the right. Variations in the bonded surface area of each layer where bonded to the adjacent road before delamination also exist. Comparisons of the old and new sample layers yielded average layer thickness measurements of 0.27 and 0.26 respectively. A highly-diffused zone was discovered in the new sample on the left of the fracture surface. This zone varied between 1.95mm to 3.2mm in width. Two similar zones exist on either side of the old sample. However, these extend across most the samples fracture surface reaching approximately 4.5mm inward from either side leaving a 4mm area in the centre where the individual layers are visible. Failure mechanism between the two samples differed. The newer sample failed due to delamination between the adjacent roads along the y-z plane ending in fracture as a result of crack propagation through the highly-diffused zone. Since the old samples had a great level of diffusion throughout, the main reason for failure was due to crack propagation through the sample with intermittent delamination between roads resulting in the fibre pull out effect observed.

Results from the SEM examination aid in supporting the finding of the tensile testing. A difference in the printing patterns and properties of the two samples exist. Several factors can contribute to this however, in order to ensure that the only influential factors be uncontrollable ones, thorough communication with the manufacturers would ensure identical print parameters were used. Based on these findings, it is believed that the age of a printer does have the potential to significantly affect the quality of the parts it manufactures. Parts

manufactured on identical FDM printers do have variations in the part properties due to variations in the machines as these machines aren't perfectly identical. It is therefore difficult to accurately predict the strength and properties of parts when all parts are not manufactured on the same printer.

6. Conclusions and Future Recommendations

6.1. Conclusions

The aim of this research was to identify opportunities to improve the knowledge of the mechanical properties of FDM parts. This comes as a result of the drastic shift of FDM part production from rapid prototyping to final end use products. In order to successfully identify the opportunities in the research area, a thorough literature review was completed investigating the various methods used in the determination of FDM part mechanical properties. A review of each of the testing methods such as tensile, flexural and fatigue allowed for the identification of the testing standards used. This review also identified the investigation methods relied on and process parameters examined by researchers. It was found that various standards specifically designed for use on bulk materials are utilised as no standards for orthotropic parts such as those of FDM currently existed. This results in inaccurate comparisons of parts manufactured using identical printers and material. A review on alternative methods used in the examination of FDM part properties such as Fiber Bragg Grating was also completed along with the use of FEA analysis for the prediction and design of FDM parts. This is important as it furthers the understanding of different factors of FDM part properties and the methods that could potentially be used in the future development of the FDM processes.

Through the literature review it was identified that all the research investigating the mechanical properties of FDM parts was done using commercially available locked hardware or on open source hobbyist market machines. No effort had been made to print using more controllable and versatile machines. This identified an area of research that was untouched. Therefore, as part of this research, and due to the availability of legacy machines on the market having superior hardware but mostly old electronics and software, a Stratasys Vantage X printer was retrofitted and optimised. This would allow for parts to be

manufactured using control parameters and feed stock outside the traditional limitations of the machine imposed by the manufacturers. The literature review also identified an untouched research area in the investigation of mechanical properties of FDM parts. With most research focussing on the effect that control variables such as layer height, air gap, and raster width has on the mechanical properties of FDM parts, none have investigated the temporal effect on build quality of these parts nor how printer age influences part quality. Another opportunity was identified in the use of SEM imaging in the investigation of FDM samples. Although SEM has been used in the past to investigate the fracture surfaces of FDM parts, none have used it to thoroughly investigate the intricate details of FDM samples. This includes the investigation of the air gap sizes and their comparisons, layer thicknesses and their variations, the levels of diffusion and the shrinking effects as a result of the FDM process.

As part of this research, the Stratasys Vantage X machine had custom hardware installed with new open-source software for system control, final testing and optimisation of the printer. This included redesign of the power supply system, motherboard, and extruder boards. A modified version of the Makerbot "thing-o-matic" firmware was used. The manufacturer's cartridge system was removed and replaced by an exchangeable spool system. The system was then optimised and parts tested determining the quality of parts manufactured on the new machine. Testing also proved that this new system is capable of printing parts using materials that the machine isn't designed for. This could only be achieved by having full control over all the control variables such as the extrusion temperature etc. normally controlled by the software based on the material the printer is designed for. This retrofitment allows the user to manufacture a sample while having full access to all control variable. This along with the custom feed stock system allowing the use of any extrudable material grants access to a research machine that is not available on the market today and opens up a wide field for potential future research not achievable in the past. Through testing and characterisation, it was proven that the printer could be modified to use materials not originally on the machines capabilities list. Thus, proving the value that such a research machine adds to researchers for the investigation into the effects of various control variables on FDM part mechanical properties.

The identification of the gap in research investigating the temporal effect on build quality of FDM parts along with the effect of machine age, led to the manufacture of identical test samples on the same machines at different times. Completed tensile testing of the samples was used to study the samples stress, strain, and Young's moduli responses and compared these chronologically manufactured samples. Samples manufactured when the printer was newer using identical print conditions were shown to have superior tensile strength. Visual examination of the fracture surface also showed greater levels of diffusion in the initially printed samples for both the 0° and 90° orientations. These samples, particularly the 0°, exhibit similar properties to their injection moulded counterparts. For the newer samples, the 0° orientation also more closely resembled those properties of the bulk material parts.

Similar Young's moduli were found in both 90° sample groups but were different when compared to the bulk material and old 0° samples. Based on the results, it was concluded that the raster orientation effects the Young's modulus values of a part as the failure of the part is subject to the inter-road bonding in the plane perpendicular to the applied load. The raster orientation also plays a significant role in the strain experienced by samples with higher strain values achieved by the 0° samples as the fibres show a greater ability to undergo elongation compared to the inter-road bonds. Results proved that the age of a printer also greatly affects the mechanical properties of parts manufactured on it. The variations in the diffusion between parts are a direct result of the printing process. As the only variation in the manufacturing properties of the parts was the temporal spacing, it is concluded that printer age played a significant role in the parts diffusion quality. A factor that has not been examined before now. Research into the topographical and fracture surfaces of the samples facilitated in proving the increased diffusion in the older parts. In the topographical view, the print patterns for the samples were almost identical. However, the void sizes produced were larger for the older samples. The road widths were also narrower in the old samples with a smaller bonded section between the internal fill and boundary layer. Fracture surface analysis of the 90° samples showed distinct layers in the newer samples with the extruded fibres easily visible. In older samples these layers weren't as distinct due to the high level of diffusion. Newer samples also exhibited a difference between the diffusion zones toward the left and right sides of the fracture surface with one side being more thoroughly diffused than the other. This is a result of variations in the print process. It is therefore concluded that machine age

influences the effective diffusion of parts as well. To the best of our knowledge, a thorough SEM investigation into the topographical and fracture surfaces of FDM samples has never been completed. This adds considerable value to the current knowledge of mechanical properties of the printed parts and the factors that affect them. Design engineers can possibly consider another factor, the printer's age, to take into account when designing parts.

Before having parts manufactured by a bureau, designers should ask the age of the printer used for the manufacture of the parts along with the maintenance history. This will be valuable knowledge that should be taken into account during the design process. This research also identified the potential for a standardised testing or grading standard to be introduced for use in industry. The introduction of such a standard could see bureaus being graded based on the quality of samples they manufacture in according with specified guidelines. These samples can then be tested resulting in a quality grade for the bureau. This would allow designers to know what quality they can expect from the bureau manufacturing their parts.

Alternatively, bureaus could regularly print their own test samples and have their mechanical properties evaluated. This would allow them to report their results to potential clients proving the integrity of their machines are still intact and the same quality can be expected as in the past.

This work is believed to be the first documented study to investigate the effect of temporal spacing on the properties of FDM printed parts.

6.2. Recommended Future Work

Future research will be conducted on the properties of various custom materials and the print parameters required for high quality parts. This will require continuous improvement on the retrofit printer. The replacement of the current Arduino based control system in the printer with a more modern printer control board is recommended. This will update the capability of the printer to for use over a network as well as the internet. The servo motors used in the extruder should also be replaced with stepper motors. The overall strength of the parts manufactured on the 'Vantage X' printer could be significantly increased should the bonded

quality of the fill be improved. Use of the printer for the examination of composite materials is recommended as the printer will allow for the optimization of print parameters for the custom material including variables such as extruder temperature. As the Vantage X grants the user access to more control variable combinations, this should be used for a more thorough examination of the previously locked variables and their effect on part properties.

Following on from the samples and results achieved in this research, nano-indentation on the fracture surfaces is warranted. The use of nano-indentation to examine the bonded regions and specifically the bonded regions between two adjacent roads, will further the understanding of the diffusion that occurs within FDM samples and how this affects the hardness of the diffused zones. Continued research into the mechanical properties of FDM parts and the chronological effects on the printers should be continued. In this research, parts were manufactured using identical control variables apart from the varied raster angle. In order to gain a more thorough understanding on how continued use of a printer affects its accuracy and repeatability in the manufacture of parts, an investigation should be done where multiple control variable is varied. The use of ANOVA analysis will allow for a reduced number of samples and accurate results for the effects of specific control variable combinations. Three sample groups should be manufactured of each control variable combination. By initially manufacturing two identical sets of each sample group, a control group can be tested immediately after manufacture. Based on the desired time determined by the length of the study, the third sample group can be manufactured and mechanical testing conducted along with the second sample group at the predetermined end time of the test.. This will show whether a significant difference exists between two sample groups printed at the same time but tested at different dates. The difference between groups one and three will also indicate the difference between samples as a results of machine age. This will help identify how the samples are affected by time and, due to machine age, which control variable's effect is magnified the most by the ageing of the printer.

In conjunction with this test many sample groups having identical print parameters should be manufactured and periodically tested. By manufacturing five sample groups with identical print parameters, testing can be completed on each of the groups every three months. This will indicate what effect time has on samples as the control sample group (one of the five groups) will act as reference for the following four groups tested quarterly. This will help to

understand the effect, if any, time has on samples along with how quickly the effect is measurable.

As found by this research, the main reason for the difference in tensile strength of parts is the difference in diffusion level between the samples. With the newer sample showing higher levels of diffusion on the sides compared to the centre of the sample, an investigation into the effect that sample dimensions in combination with the achieved diffusion is warranted. By manufacturing two sample types having identical heights but varying the width, it is possible to identify how the highly-diffused edges of the samples vary in relation to the varying widths of the samples. This will help identify how the strength of the sample is affected by the contact area between bonded surfaces and if there is a linear relationship between strength and sample size or non-linear because of the relative relationship between the thoroughly diffused areas and the surface size.

The work conducted in this research aims to improve the understanding of FDM part mechanical properties by investigating specific properties to a higher level than had previously been done. This research in combination with the future work will help understand the role individual printers play on the chronological manufacturing of parts and hopefully help in the development of a comprehensive rule base for the manufacture of parts by means of FDM in the future.

7. References

[1] T. Wohlers and T. Gornet, "History of additive manufacturing," *Wohlers Report: Additive Manufacturing and 3D Printing State of the Industry Annual Worldwide Progress Report,* 2011.

[2] B. Wittbrodt and J. M. Pearce, "The effects of PLA color on material properties of 3-D printed components," *Additive Manufacturing,* vol. 8, pp. 110-116, 10// 2015.

[3] M. Molitch-hou. (2014). *Consumer 3D printing in Serious Growth phase According to Photizo group*. Available: http://3dprintingindustry.com/2014/08/14/consumer-3d-printing-serious-growth-phase-according-photizo-group/

[4] C. Mueller, A. IRANI, and B. Jenett, "Additive Manufacturing of Structural Prototypes for Conceptual Design," in *Proceedings of the International Association for Shell and Spatial Structures (IASS) Symposium*, 2014.

[5] H. Bikas, P. Stavropoulos, and G. Chryssolouris, "Additive manufacturing methods and modelling approaches: a critical review," *The International Journal of Advanced Manufacturing Technology,* pp. 1-17, 2015.

[6] N. Guo and M. C. Leu, "Additive manufacturing: technology, applications and research needs," *Frontiers of Mechanical Engineering,* vol. 8, pp. 215-243, 2013.

[7] B. N. Turner, R. Strong, and S. A. Gold, "A review of melt extrusion additive manufacturing processes: I. Process design and modeling," *Rapid Prototyping Journal,* vol. 20, pp. 192-204, 2014/04/14 2014.

[8] K. M. Rahman, T. Letcher, and R. Reese, "Mechanical Properties of Additively Manufactured PEEK Components Using Fused Filament Fabrication," in *ASME 2015 International Mechanical Engineering Congress and Exposition*, 2015, pp. V02AT02A009-V02AT02A009.

[9] F. Fisher, "Thermoplastics: the strongest choice for 3D printing," *White Paper by Stratasys Inc.(USA),* 2001.

[10] M. M. Schultz. (2012, Constant Improvement: Jeff DeGrange on the state of additive manufacturing for aerospace. 4. Available: http://usglobalimages.stratasys.com/Main/Secure/White%20Papers/Rebranded/SSYS_WP_constant_improvement_jeff_degrange.pdf?v=635011144147354460

[11] D. Drummer, S. Cifuentes-Cuéllar, and D. Rietzel, "Suitability of PLA/TCP for fused deposition modeling," *Rapid Prototyping Journal,* vol. 18, pp. 500-507, 2012.

[12] D. Bourell, B. Stucker, D. Espalin, K. Arcaute, D. Rodriguez, F. Medina, *et al.*, "Fused deposition modeling of patient-specific polymethylmethacrylate implants," *Rapid Prototyping Journal,* vol. 16, pp. 164-173, 2010.

[13] B. J. Brooks, K. M. Arif, S. Dirven, and J. Potgieter, "Robot-assisted 3D printing of biopolymer thin shells," *The International Journal of Advanced Manufacturing Technology,* pp. 1-12, 2016.

[14] T. Serra, J. A. Planell, and M. Navarro, "High-resolution PLA-based composite scaffolds via 3-D printing technology," *Acta biomaterialia,* vol. 9, pp. 5521-5530, 2013.

[15] O. S. Es-Said, J. Foyos, R. Noorani, M. Mendelson, R. Marloth, and B. A. Pregger, "Effect of Layer Orientation on Mechanical Properties of Rapid Prototyped Samples," *Materials and Manufacturing Processes,* vol. 15, pp. 107-122, 2000/01/01 2000.

[16] D. L. Bourell, "Perspectives on Additive Manufacturing," *Annual Review of Materials Research,* 2016.

[17] C. Casavola, A. Cazzato, V. Moramarco, and C. Pappalettere, "Orthotropic mechanical properties of fused deposition modelling parts described by classical laminate theory," *Materials & Design,* vol. 90, pp. 453-458, 1/15/ 2016.

[18] H. Tingting, W. Shanggang, and H. Ketai, "Quality control for fused deposition modeling based additive manufacturing: Current research and future trends," in *Reliability Systems Engineering (ICRSE), 2015 First International Conference on*, 2015, pp. 1-6.

[19] A. Bellini and S. Güçeri, "Mechanical characterization of parts fabricated using fused deposition modeling," *Rapid Prototyping Journal,* vol. 9, pp. 252-264, 2003.

[20] B. N. Turner and S. A. Gold, "A review of melt extrusion additive manufacturing processes: II. Materials, dimensional accuracy, and surface roughness," *Rapid Prototyping Journal,* vol. 21, pp. 250-261, 2015.

[21] A. W. Fatimatuzahraa, B. Farahaina, and W. A. Y. Yusoff, "The effect of employing different raster orientations on the mechanical properties and microstructure of Fused Deposition Modeling parts," in *Business, Engineering and Industrial Applications (ISBEIA), 2011 IEEE Symposium on*, 2011, pp. 22-27.

[22] A. K. Sood, R. K. Ohdar, and S. S. Mahapatra, "Parametric appraisal of mechanical property of fused deposition modelling processed parts," *Materials & Design,* vol. 31, pp. 287-295, 1// 2010.

[23] A. Li, Z. Zhang, D. Wang, and Y. Jinyong, "Optimization method to fabrication orientation of parts in fused deposition modeling rapid prototyping," in *Mechanic Automation and Control Engineering (MACE), 2010 International Conference on*, 2010, pp. 416-419.

[24] R. Anitha, S. Arunachalam, and P. Radhakrishnan, "Critical parameters influencing the quality of prototypes in fused deposition modelling," *Journal of Materials Processing Technology,* vol. 118, pp. 385-388, 2001.

[25] D. Croccolo, M. De Agostinis, and G. Olmi, "Experimental characterization and analytical modelling of the mechanical behaviour of fused deposition processed parts made of ABS-M30," *Computational Materials Science,* vol. 79, pp. 506-518, 11// 2013.

[26] K.-M. M. TAM, J. R. COLEMAN, N. W. FINE, and C. T. MUELLER, "Stress line additive manufacturing (SLAM) for 2.5-D shells."

[27] B. Vasudevarao, D. P. Natarajan, M. Henderson, and A. Razdan, "Sensitivity of RP surface finish to process parameter variation," in *Solid Freeform Fabrication Proceedings*, 2000, pp. 251-258.

[28] D. A. Roberson, A. R. Torrado Perez, C. M. Shemelya, A. Rivera, E. MacDonald, and R. B. Wicker, "Comparison of stress concentrator fabrication for 3D printed polymeric izod impact test specimens," *Additive Manufacturing,* vol. 7, pp. 1-11, 7// 2015.

[29] C. S. Lee, S. G. Kim, H. J. Kim, and S. H. Ahn, "Measurement of anisotropic compressive strength of rapid prototyping parts," *Journal of Materials Processing Technology,* vol. 187–188, pp. 627-630, 6/12/ 2007.

[30] S.-H. Ahn, M. Montero, D. Odell, S. Roundy, and P. K. Wright, "Anisotropic material properties of fused deposition modeling ABS," *Rapid Prototyping Journal,* vol. 8, pp. 248-257, 2002.

[31] Q. Sun, G. Rizvi, C. Bellehumeur, and P. Gu, "Effect of processing conditions on the bonding quality of FDM polymer filaments," *Rapid Prototyping Journal,* vol. 14, pp. 72-80, 2008.

[32] R. Singh, R. Singh, S. Singh, S. Singh, K. Mankotia, and K. Mankotia, "Development of ABS based wire as feedstock filament of FDM for industrial applications," *Rapid Prototyping Journal,* vol. 22, pp. 300-310, 2016.

[33] A. R. Torrado and D. A. Roberson, "Failure analysis and anisotropy evaluation of 3D-printed tensile test specimens of different geometries and print raster patterns," *Journal of Failure Analysis and Prevention,* vol. 16, pp. 154-164, 2016.

[34] V. Francis and P. K. Jain, "Experimental investigations on fused deposition modelling of polymer-layered silicate nanocomposite," *Virtual and Physical Prototyping,* pp. 1-13, 2016.

[35] F. Górski, W. Kuczko, R. Wichniarek, and A. Hamrol, "Computation of Mechanical Properties of Parts Manufactured by Fused Deposition Modeling Using Finite Element Method," in *10th International Conference on Soft Computing Models in Industrial and Environmental Applications*, 2015, pp. 403-413.

[36] R. Rezaei, M. K. Ravari, M. Badrossamay, and M. Kadkhodaei, "Mechanical characterization and finite element modeling of polylactic acid BCC-Z cellular lattice structures fabricated by fused deposition modeling," *Proceedings of the Institution of Mechanical Engineers, Part C: Journal of Mechanical Engineering Science,* p. 0954406215626941, 2016.

[37] S. Ogden and S. Kessler, "Anisotropic finite element modeling of the fused deposition modeling process," *Characterization of Minerals, Metals, and Materials 2014,* pp. 235-243, 2014.

[38] Z. Weng, J. Wang, T. Senthil, and L. Wu, "Mechanical and thermal properties of ABS/montmorillonite nanocomposites for fused deposition modeling 3D printing," *Materials & Design,* vol. 102, pp. 276-283, 7/15/ 2016.

[39] K. Szykiedans and W. Credo, "Mechanical Properties of FDM and SLA Low-cost 3-D Prints," *Procedia Engineering,* vol. 136, pp. 257-262, // 2016.

[40] F. Górski, R. Wichniarek, W. Kuczko, and J. Andrzejewski, "Experimental Determination of Critical Orientation of ABS Parts Manufactured Using Fused Deposition Modelling Technology," *Journal of Machine Engineering,* vol. 15, pp. 121--132, 2015.

[41] M. Dawoud, I. Taha, and S. J. Ebeid, "Mechanical behaviour of ABS: An experimental study using FDM and injection moulding techniques," *Journal of Manufacturing Processes,* vol. 21, pp. 39-45, 1// 2016.

[42] M. Bertoldi, M. Yardimci, C. Pistor, S. Guceri, and G. Sala, "Mechanical characterization of parts processed via fused deposition," in *Proceedings of the 1998 solid freeform fabrication symposium*, 1998, pp. 557-565.

[43] W. Wu, P. Geng, G. Li, D. Zhao, H. Zhang, and J. Zhao, "Influence of Layer Thickness and Raster Angle on the Mechanical Properties of 3D-Printed PEEK and a Comparative Mechanical Study between PEEK and ABS," *Materials,* vol. 8, pp. 5834-5846, 2015.

[44] F. Rayegani and G. C. Onwubolu, "Fused deposition modelling (FDM) process parameter prediction and optimization using group method for data handling (GMDH) and differential evolution (DE)," *The International Journal of Advanced Manufacturing Technology,* vol. 73, pp. 509-519, 2014.

[45] F. Ning, W. Cong, J. Qiu, J. Wei, and S. Wang, "Additive manufacturing of carbon fiber reinforced thermoplastic composites using fused deposition modeling," *Composites Part B: Engineering,* vol. 80, pp. 369-378, 10// 2015.

[46] C. Ziemian, M. Sharma, and S. Ziemian, *Anisotropic mechanical properties of ABS parts fabricated by fused deposition modelling*: INTECH Open Access Publisher, 2012.

[47] P. Pandey, N. V. Reddy, and S. Dhande, "Part deposition orientation studies in layered manufacturing," *Journal of materials processing technology,* vol. 185, pp. 125-131, 2007.

[48] J. Torres, J. Torres, M. Cole, M. Cole, A. Owji, A. Owji*, et al.*, "An approach for mechanical property optimization of fused deposition modeling with polylactic acid via design of experiments," *Rapid Prototyping Journal,* vol. 22, pp. 387-404, 2016.

[49] F. Górski, R. Wichniarek, W. Kuczko, P. Zawadzki, and P. Buń, "Strength of ABS parts produced by Fused Deposition Modelling technology–a critical orientation problem," *Adv. Sci. Technol. Res. J,* vol. 9, pp. 12-19, 2015.

[50] O. A. Mohamed, S. H. Masood, J. L. Bhowmik, M. Nikzad, and J. Azadmanjiri, "Effect of Process Parameters on Dynamic Mechanical Performance of FDM PC/ABS Printed Parts Through Design of Experiment," *Journal of Materials Engineering and Performance,* pp. 1-14.

[51] B. M. Tymrak, M. Kreiger, and J. M. Pearce, "Mechanical properties of components fabricated with open-source 3-D printers under realistic environmental conditions," *Materials & Design,* vol. 58, pp. 242-246, 6// 2014.

[52] M. F. Afrose, S. Masood, M. Nikzad, and P. Iovenitti, "Effects of build orientations on tensile properties of PLA material processed by FDM," in *Advanced Materials Research*, 2014, pp. 31-34.

[53] E. Fodran, M. Koch, and U. Menon, "Mechanical and dimensional characteristics of fused deposition modeling build styles," in *Solid Freeform Fabrication Proc*, 1996, pp. 419-442.

[54] ASTM, "ASTM D638-10, Standard Test Method for Tensile Properties of Plastics," in ed. www.astm.org: ASTM International, 2010.

[55] ASTM, "ASTM D695-96, Test Method for Compressive Properties of Rigid Plastics.," ed: ASTM, 1996.

[56] B. N. Panda, M. V. A. R. Bahubalendruni, and B. B. Biswal, "A general regression neural network approach for the evaluation of compressive strength of FDM prototypes," *Neural Computing and Applications,* vol. 26, pp. 1129-1136, 2014.

[57] G. Percoco, F. Lavecchia, and L. M. Galantucci, "Compressive properties of FDM rapid prototypes treated with a low cost chemical finishing," *Research Journal of Applied Sciences, Engineering and Technology,* vol. 4, pp. 3838-3842, 2012.

[58] A. K. Sood, R. K. Ohdar, and S. S. Mahapatra, "Experimental investigation and empirical modelling of FDM process for compressive strength improvement," *Journal of Advanced Research,* vol. 3, pp. 81-90, 2012.

[59] B. H. Lee, J. Abdullah, and Z. A. Khan, "Optimization of rapid prototyping parameters for production of flexible ABS object," *Journal of Materials Processing Technology,* vol. 169, pp. 54-61, 10/30/ 2005.

[60] A. Tsouknidas, M. Pantazopoulos, I. Katsoulis, D. Fasnakis, S. Maropoulos, and N. Michailidis, "Impact absorption capacity of 3D-printed components fabricated by fused deposition modelling," *Materials & Design,* vol. 102, pp. 41-44, 2016.

[61] S. K. Panda, S. Padhee, S. Anoop Kumar, and S. Mahapatra, "Optimization of fused deposition modelling (FDM) process parameters using bacterial foraging technique," *Intelligent information management,* vol. 1, p. 89, 2009.

[62] J. T. Belter and A. M. Dollar, "Strengthening of 3D printed fused deposition manufactured parts using the fill compositing technique," *PloS one,* vol. 10, p. e0122915, 2015.

[63] S. Singamneni, A. Roychoudhury, O. Diegel, and B. Huang, "Modeling and evaluation of curved layer fused deposition," *Journal of Materials Processing Technology,* vol. 212, pp. 27-35, 1// 2012.

[64] L. M. Galantucci, F. Lavecchia, and G. Percoco, "Quantitative analysis of a chemical treatment to reduce roughness of parts fabricated using fused deposition modeling," *CIRP Annals - Manufacturing Technology,* vol. 59, pp. 247-250, // 2010.

[65] ASTM, "ASTM D790-15e2, Standard Test Methods for Flexural Properties of Unreinforced and Reinforced Plastics and Electrical Insulating Materials," ed. ASTM International, West Conshohocken, PA, 2015.

[66] ISO, "ISO 178: Plastics -- Determination of flexural properties," ed. www.iso.org: ISO.org, 2012, p. 19.

[67] M. Domingo-Espin, J. M. Puigoriol-Forcada, A.-A. Garcia-Granada, J. Llumà, S. Borros, and G. Reyes, "Mechanical property characterization and simulation of fused deposition modeling Polycarbonate parts," *Materials & Design,* vol. 83, pp. 670-677, 10/15/ 2015.

[68] M. F. Afrose, S. H. Masood, P. Iovenitti, M. Nikzad, and I. Sbarski, "Effects of part build orientations on fatigue behaviour of FDM-processed PLA material," *Progress in Additive Manufacturing,* pp. 1-8, 2015.

[69] ISO, "ISO 13003:2003 Fibre-reinforced plastics -- Determination of fatigue properties under cyclic loading conditions," ed: ISO, 2006, p. 17.

[70] M. Zoroufi. (2013). *Significance of fatigue testing parameters in plastics versus metals.* Available: http://softlaunch.element.quba.co.uk/.

[71] J. Lee and A. Huang, "Fatigue analysis of FDM materials," *Rapid Prototyping Journal,* vol. 19, pp. 291-299, 2013.

[72] S. Swapp. (2016, 24/04). *Scanning Electron Microscopy (SEM)*. Available: http://serc.carleton.edu/research_education/geochemsheets/techniques/SEM.html

[73] D. Karalekas, "On the use of FBG sensors for measurement of curing strains in photocurable resins," *Rapid Prototyping Journal,* vol. 14, pp. 81-86, 2008.

[74] J. Goldstein, D. E. Newbury, P. Echlin, D. C. Joy, A. D. Romig Jr, C. E. Lyman, *et al.*, *Scanning electron microscopy and X-ray microanalysis: a text for biologists, materials scientists, and geologists*: Springer Science & Business Media, 2012.

[75] ACMAL. (2015, 24-04-2016). *Philips XL 40 ESEM*. Available: http://mcff.mtu.edu/acmal/electron-microscopy/philips-xl-40-esem/

[76] A. R. Torrado, C. M. Shemelya, J. D. English, Y. Lin, R. B. Wicker, and D. A. Roberson, "Characterizing the effect of additives to ABS on the mechanical property anisotropy of specimens fabricated by material extrusion 3D printing," *Additive Manufacturing,* vol. 6, pp. 16-29, 4// 2015.

[77] S. Dul, L. Fambri, and A. Pegoretti, "Fused deposition modelling with ABS–graphene nanocomposites," *Composites Part A: Applied Science and Manufacturing,* vol. 85, pp. 181-191, 2016.

[78] FBGS. (2016). *FBG - FIBER BRAGG GRATING PRINCIPLE*. Available: http://www.fbgs.com/technology/fbg-principle/

[79] A. Kantaros, J. Giannatsis, and D. Karalekas, "A novel strategy for the incorporation of optical sensors in Fused Deposition Modeling parts," *Advanced Manufacturing Engineering and Technologies NEWTECH 2013 Stockholm, Sweden 27-30 October 2013,* p. 163, 2013.

[80] X. Li and F. Prinz, "Embedded fiber Bragg grating sensors in polymer structures fabricated by layered manufacturing," *Journal of Manufacturing Processes,* vol. 5, pp. 78-86, 2003.

[81] R. Maier, W. MacPherson, J. Barton, M. Carne, M. Swan, J. Sharma, *et al.*, "Fibre optic strain and configuration sensing in engineering components produced by additive layer rapid manufacturing," in *Sensors, 2011 IEEE*, 2011, pp. 1353-1357.

[82] R. R. Maier, W. N. MacPherson, J. S. Barton, M. Carne, M. Swan, J. N. Sharma, *et al.*, "Embedded fiber optic sensors within additive layer manufactured components," *Sensors Journal, IEEE,* vol. 13, pp. 969-979, 2013.

[83] A. Kantaros and D. Karalekas, "Fiber Bragg grating based investigation of residual strains in ABS parts fabricated by fused deposition modeling process," *Materials & Design,* vol. 50, pp. 44-50, 9// 2013.

[84] F. Colpo, L. Humbert, and J. Botsis, "Characterisation of residual stresses in a single fibre composite with FBG sensor," *Composites Science and Technology,* vol. 67, pp. 1830-1841, 2007.

[85] S. N. Economidou and D. Karalekas, "Optical sensor-based measurements of thermal expansion coefficient in additive manufacturing," *Polymer Testing,* vol. 51, pp. 117-121, 5// 2016.

[86] Stratasys. (2011, 26/04). *ABS-P400*. Available: https://www.padtinc.com/downloads/Stamp%20Dimension-ABS-Model-Material.pdf

[87] C. Kousiatza and D. Karalekas, "In-situ monitoring of strain and temperature distributions during fused deposition modeling process," *Materials & Design,* vol. 97, pp. 400-406, 5/5/ 2016.

[88] Y. Zhang and K. Chou, "A parametric study of part distortions in fused deposition modelling using three-dimensional finite element analysis," *Proceedings of the Institution of Mechanical Engineers, Part B: Journal of Engineering Manufacture,* vol. 222, pp. 959-968, 2008.

[89] Y. Zhang and Y. Chou, "Three-dimensional finite element analysis simulations of the fused deposition modelling process," *Proceedings of the Institution of Mechanical Engineers, Part B: Journal of Engineering Manufacture,* vol. 220, pp. 1663-1671, 2006.

[90] H. Li, G. Taylor, V. Bheemreddy, O. Iyibilgin, M. Leu, and K. Chandrashekhara, "Modeling and characterization of fused deposition modeling tooling for vacuum assisted resin transfer molding process," *Additive Manufacturing,* vol. 7, pp. 64-72, 2015.

[91] P.A.Kelly, *Solid Mechanics Part I: An Introduction to Solid Mechanics*: Auckland University, 2015.

[92] R. Richards Jr, *Principles of solid mechanics*: CRC Press, 2000.

[93] D. P. Mark Michalovic, Patricia DePra Springsteen. (2005). *The Glass Transition*. Available: http://pslc.ws/macrog/level3.htm

[94] J. F. Rodríguez, J. P. Thomas, and J. E. Renaud, "Mechanical behavior of acrylonitrile butadiene styrene (ABS) fused deposition materials. Experimental investigation," *Rapid Prototyping Journal,* vol. 7, pp. 148-158, 2001.

[95] K. P. Karunakaran, S. Suryakumar, V. Pushpa, and S. Akula, "Low cost integration of additive and subtractive processes for hybrid layered manufacturing," *Robotics and Computer-Integrated Manufacturing,* vol. 26, pp. 490-499, 10// 2010.

[96] K. P. Karunakaran, S. Suryakumar, V. Pushpa, and S. Akula, "Retrofitment of a CNC machine for hybrid layered manufacturing," *The International Journal of Advanced Manufacturing Technology,* vol. 45, pp. 690-703, 2009.

[97] S. Shaikh, N. Kumar, P. K. Jain, and P. Tandon, "Hilbert Curve Based Toolpath for FDM Process," in *CAD/CAM, Robotics and Factories of the Future: Proceedings of the 28th International Conference on CARs & FoF 2016*, D. K. Mandal and C. S. Syan, Eds., ed New Delhi: Springer India, 2016, pp. 751-759.

[98] S. Suryakumar, K. Karunakaran, U. Chandrasekhar, and M. Somashekara, "A study of the mechanical properties of objects built through weld-deposition," *Proceedings of the Institution of Mechanical Engineers, Part B: Journal of Engineering Manufacture,* vol. 227, pp. 1138-1147, 2013.

[99] S. Simhambhatla and K. P. Karunakaran, "Build strategies for rapid manufacturing of components of varying complexity," *Rapid Prototyping Journal,* vol. 21, pp. 340-350, 2015.

[100] Y.-A. Song and S. Park, "Experimental investigations into rapid prototyping of composites by novel hybrid deposition process," *Journal of Materials Processing Technology,* vol. 171, pp. 35-40, 1/10/ 2006.

[101] X. Xiong, H. Zhang, and G. Wang, "Metal direct prototyping by using hybrid plasma deposition and milling," *Journal of Materials Processing Technology,* vol. 209, pp. 124-130, 1/1/ 2009.

[102] R. Vaidyanathan, J. Walish, J. Lombardi, P. Calvert, and K. Cooper, "The extrusion freeforming of functional ceramic prototypes," *JOM,* vol. 52, pp. 34-37, 2000.

[103] M. Industries, "An open-source gcode interpreter for driving REpRaps, Makerbots, and other similar CNC beasties. ," ed, 2013.

[104] J. M. Pearce, "Building research equipment with free, open-source hardware," *Science,* vol. 337, pp. 1303-1304, 2012.

[105] W. M. Johnson, M. Rowell, B. Deason, and M. Eubanks, "Comparative evaluation of an open-source FDM system," *Rapid Prototyping Journal,* vol. 20, pp. 205-214, 2014.

[106] A. Ranellucci. (2016). *Slic3r G-code generator for 3D printers*. Available: https://github.com/alexrj/Slic3r

[107] B. Beauregard. (2012, December 2). *br3ttb / Arduino-PIDLibrary*. Available: https://github.com/br3ttb/Arduino-PID-Library/

[108] C. Bellehumeur, L. Li, Q. Sun, and P. Gu, "Modeling of bond formation between polymer filaments in the fused deposition modeling process," *Journal of Manufacturing Processes,* vol. 6, pp. 170-178, 2004.

[109] M. Faes, E. Ferraris, and D. Moens, "Influence of inter-layer cooling time on the quasi-static properties of ABS components produced via Fused Deposition Modelling," *Procedia CIRP,* vol. 42, pp. 748-753, 2016.

[110] Stratasys. (2015, 09/11). *ASA vs. ABS*. Available: http://usglobalimages.stratasys.com/Main/Files/Material_Spec_Sheets/MSS_FDM_ABSvsASA.pdf?v=635785163874834436

[111] Stratasys, "ASA," in *A UV-Stable, production-grade thermoplastic for Fortus 3D produtcion systems*, ed. Stratasys webpage: Stratasys, 2015.

[112] P. Echlin, *Handbook of sample preparation for scanning electron microscopy and X-ray microanalysis*: Springer Science & Business Media, 2011.

[113] R. B. Bird, R. C. Armstrong, and O. Hassager, "Dynamics of polymeric liquids. Volume 1: fluid mechanics," *A Wiley-Interscience Publication, John Wiley & Sons,* 1987.

[114] M. Chanda and S. K. Roy, *Plastics Fundamentals, Properties, and Testing* vol. 75: CRC press, 2008.

[115] S. Ziemian, M. Okwara, and C. W. Ziemian, "Tensile and fatigue behavior of layered acrylonitrile butadiene styrene," *Rapid Prototyping Journal,* vol. 21, pp. 270-278, 2015.

[116] C. A. Griffiths, J. Howarth, G. De Almeida-Rowbotham, A. Rees, and R. Kerton, "A design of experiments approach for the optimisation of energy and waste during the production of parts manufactured by 3D printing," *Journal of Cleaner Production,* vol. 139, pp. 74-85, 12/15/ 2016.

[117] S. Pengfei, L. Kai, and W. Yangwei, "A Model Research for Prototype Warp Deformation in the FDM Process," *Machine Design & Research,* vol. 3, p. 039, 2015.

8. Appendices

8.1. Appendix A

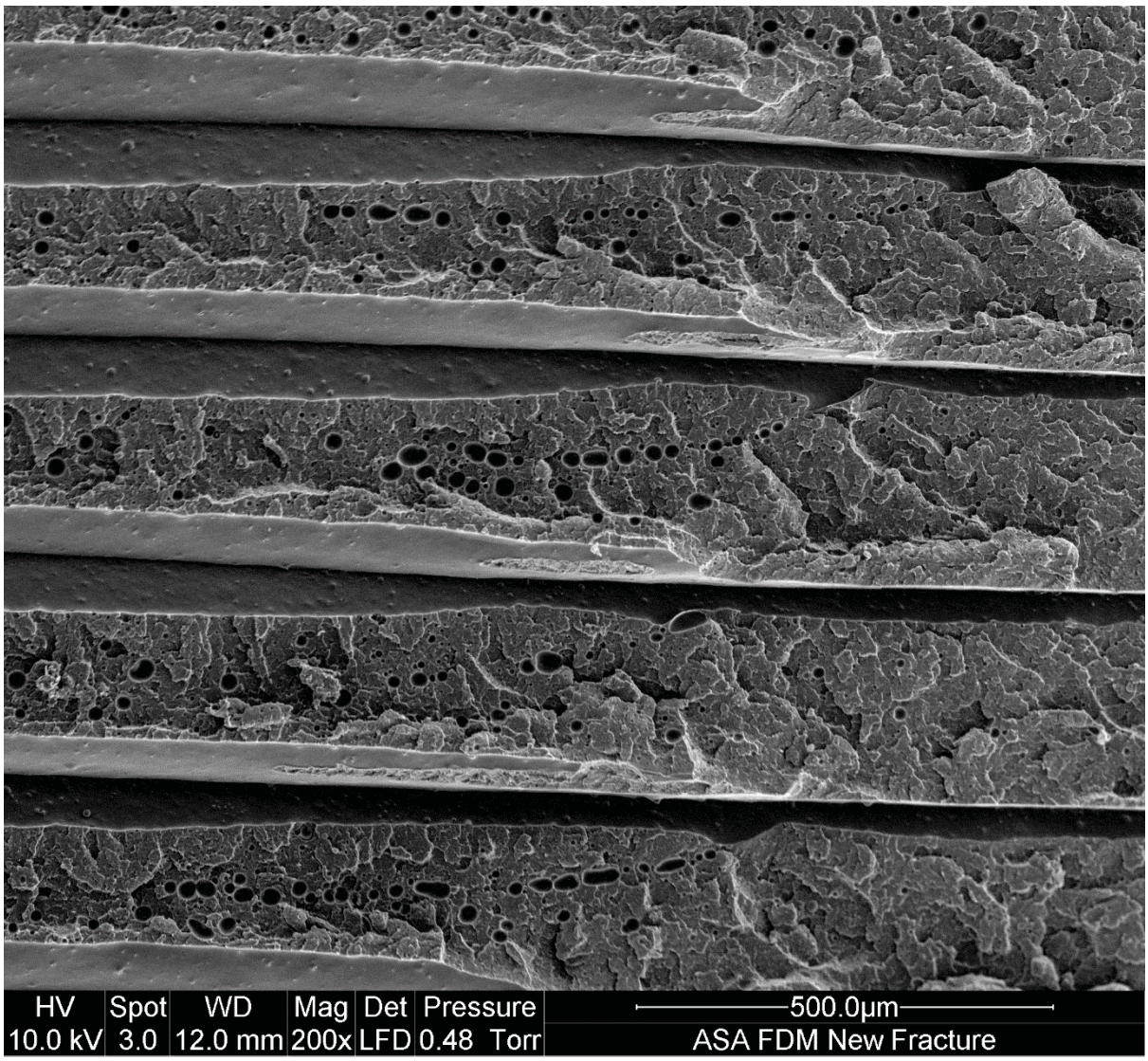

Figure 8.1 SEM image of the new sample fracture surface depicting the recurring bubbles that are introduced during the printing process.

8.2. Appendix B

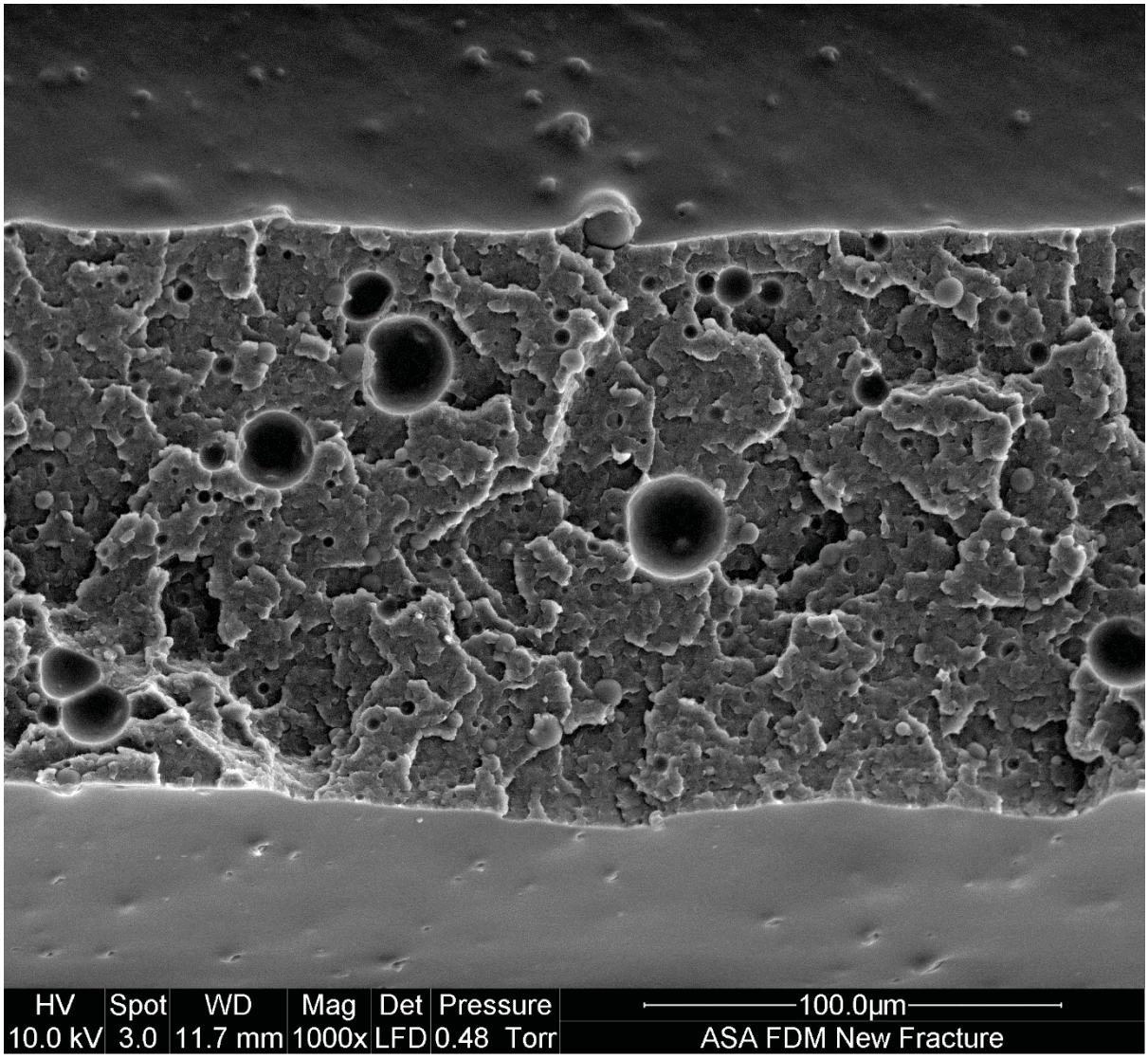

Figure 8.2 Magnified image of the inclusions observed throughout the fracture surface of the sample.

8.3. Appendix C

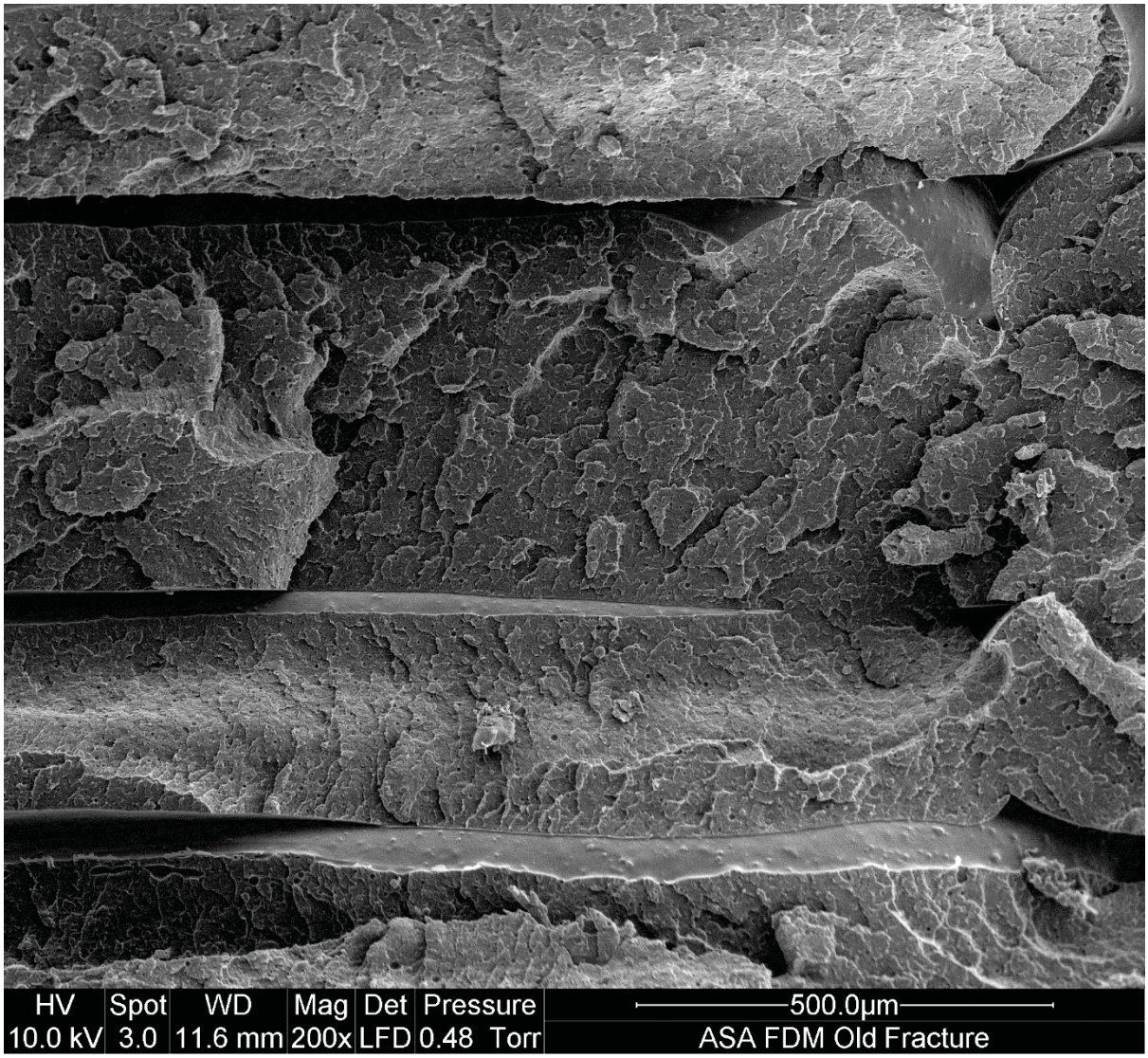

Figure 8.3 Magnified image of the old sample fracture surface depicting consecutively bonded print layers fracturing along different planes. The bubbles induced during the printing process and observed in the new sample group is absent in the old samples.